An Experimental Study of Wave Dispersion and Stability in Crossing Seas and on Sheared Currents

James Nicholas Steer
School of Engineering
University of Edinburgh

A thesis submitted for the degree of
Doctor of Philosophy
2019

To Rolf Kopp, who has made me laugh and cry more than anyone else.

Abstract

This thesis considers the effects of crossing seas and linearly sheared current on the dispersion and stability of surface gravity waves. Experimental data are compared against predictions by three different nonlinear Schrödinger equations (NLSE): the constant-vorticity (vor-NLSE), used to simulate wave evolution on a linearly sheared current; the coupled (CNLSE), which predicts the interaction between two crossing wave systems; and the two-dimensional (2D+1 NLSE), which allows an angle between the carrier wave and the packet of a single wave system.

In chapter 2, the linearly sheared currents examined are one-dimensional, in accordance with wave propagation and consist of a velocity profile varying linearly with depth. Such currents have constant-vorticity and, although rotational, admit potential flow solutions. Both the linear evolution and the weakly nonlinear behaviour of waves on five constant vorticity sheared currents in the shear rate, Ω range, $0\ \mathrm{s}^{-1} \leq \Omega \leq -0.87\ \mathrm{s}^{-1}$ are measured and compared to predictions by the vor-NLSE and vor-dispersion relation. It is found that the constant-vorticity equations agree extremely well with the experimental measurements in all cases. Significant differences between the vor-equations and uniform velocity equations are found at the strongest shear cases for both stability and linear dispersion experiments ($-0.48\ \mathrm{s}^{-1} \leq \Omega \leq -0.87\ \mathrm{s}^{-1}$).

In chapter 3, the coupled nonlinear Schrödinger equation (CNLSE) is used to quantify the effect of a crossing angle between two weakly nonlinear coupled wave systems. Individually (when unidirectional) both systems show modulational instability. This is augmented by the addition of a crossing angle between the two wave systems. Linear stability analysis of the CNLSE indicates that wavetrains become increasingly stable as the crossing angle is increased, reaching stability at a critical angle of 35.26°. The experiments presented in this thesis measured the stability of crossing angles up to 88° for a coupled system showing clear instability when the wavetrains are unidirectional. Initially strong instabilities for the interacting unidirectional case are quickly stabilised as the crossing angle is increased. The system becomes entirely stabilised when the crossing angle is increased beyond the critical angle.

In chapter 4, the two-dimensional nonlinear Schrödinger equation is used to impose a crossing angle between the carrier wave and continuous sidebands of a narrow-banded wave group. Measurements of a low-steepness wave group envelope showed normal dispersive behaviour when unidirectional. However, as the two-dimensional nonlinear Schrödinger equation predicts, at the critical angle of 35.26° it was found that the Gaussian wave group propagated with entirely unchanging form, displaying nondispersive behaviour. Similarly, when a medium-steepness Gaussian group was propagated at the critical angle, not only was the group nondispersive, the focusing present in its unidirectional propagation (due to nonlinear focusing) became negligible. Nonlinear effects were seen as the development of a double peaked wave envelope as larger waves travelled to the front of the group. These results show that wave groups are capable of travelling for extended periods of time with extreme waves at their centre. Two nondispersive crossed groups with crossing angles of ±35.26° were superimposed to create the first observations of a hydrodynamic X-wave. Such waves have previously been observed in optics, Bose-Einstein condensates, and plasmas. The X-wave has a large central amplitude where the two groups cross.

Acknowledgements

Firstly, I would like to thank both of my supervisors, Dr. Ton van den Bremer, and Prof. Alistair Borthwick for their total commitment to not only me but all their students. Particularly, I would like to thank Ton for only accepting my best and then making me improve it, and for always aiming my sights higher and guiding me to them. I would like to thank Alistair for reading and correcting the smallest through to the greatest pieces of my work, and for allowing me weekly access to his vast knowledge, regardless of the hemisphere he was in.

Thank you to Simen Ellingsen of the Norwegian University of Science and Technology and David Forehand of The University of Edinburgh (UoE) for their thorough examination of this thesis.

The experiments conducted during this PhD were made possible by collaborations with several co-authors to whom I owe enormous thanks. Dimitris Stagonas and Eugeny Buldakov of University College London twice allowed me access to the coastal flume there and enthusiastically provided their time and experience. Many thanks to Mark McAllister who, through innumerable informal discussions, endowed me with his insightful and non-judgmental answers to my silly questions. Thank you to Amin Chabchoub and Miguel Onorato whose expertise provided the theoretical basis for the work presented in chapter 4. I would also like to extend my thanks to the staff at the FloWave facility who put up with me and my whims on multiple occasions. Special thanks go to Sam Draycott at The University of Manchester for fun and interesting discussions while he worked at FloWave.

This project would not have been possible without the financial support of the Strathclyde and Edinburgh based Wind and Marine Energy Systems Centre for Doctoral Training (CDT), funded largely by the UK Engineering and Physical Sciences Research Council. The staff and students of the CDT gave the best possible start to my PhD and continued that support with a network full of students in all stages of their own studies. I would particularly like to mention the members of my own cohort who, along with their significant others, I regard as some of my closest friends.

From my arrival to my departure, The UoE School of Engineering and the CDT have provided me with hill-walking companions, motorcycling partners and above all, friendly faces too numerous to mention individually. However, I would like to thank my office mates, Alfred Cotten, Ben McGilton, Owain Roberts, and Anna Garcia-Teruel, who provided celebratory cakes throughout our time together and who were forced to endure my own efforts at baking. Thanks also to Donald Noble and Paul Bonar for always having time to forget about waves on a Friday evening.

Finally, I would like to thank my parents, Esther and Alan; my sister, Emma; and all my extended family, without whom I would never have been in a position to start this PhD, let alone complete it successfully.

Declaration of Originality

I declare that I have composed this thesis myself and, except where otherwise noted, the work contained within it is entirely my own. Parts of this thesis have already been published, as noted in the text, but no part has been submitted previously for any other degree or professional qualification.

James N. Steer

Contents

List of Figures

List of Tables

Chapter 1

Introduction

1.1 Background

1.1.1 Research context

At a liquid's free surface, vertical perturbations are restored by gravity and buoyancy forces causing periodic oscillations which form surface gravity waves. Surface gravity waves can be comprised of one frequency (regular waves) or can be the result of a number of frequencies and amplitudes being superimposed. Waves in the ocean appear irregular: overlapping, breaking, crossing, and interacting seemingly without much rhyme or reason. However, on a much larger scale, irregular waves often form part of a wave group, having been generated by a single storm event and travelling large distances. Wave groups such as these are generated with some directionality and may meet and interact with other groups, formed by other events, at different times, or may go on to interact with strong currents (formed by tides or generated by the wind). This thesis will investigate the effect of crossing waves and currents on wave behaviour, and seeks to determine the applicability of their leading-order governing equations, the constant vorticity nonlinear Schrödinger equation, the coupled nonlinear Schrödinger equation, and the 2D nonlinear Schrödinger equation. The three nonlinear Schrödinger equations are all capable of describing the formation of very large, possibly rogue, waves. Anecdotally, rogue waves have long been known as a danger to offshore structures and shipping. However, their existence and behaviour was not formally investigated until the second half of the 20th century. With the rising worldwide demand for renewable energy, offshore structures are becoming increasingly utilized in the extraction of offshore wind energy (including floating), wave energy, and tidal energy.

The specialised topics of wave crossing and wave interactions with currents are examined in this thesis because of their applicability to offshore technologies for marine renewable energy extraction. Interaction with currents is inherent to the operation of tidal-stream turbines, whereas the power output of wave energy devices is dependent on their placement in wave energy-dense environments. Traditional wind turbines are increasingly operated in far-shore, deep-water conditions putting the support structures at risk of experiencing crossing seas. Due to the relative immaturity of these offshore renewable energy structures, understanding their environment for design, operation and maintenance is a major concern. Immaturity also means that reports of rogue waves and extreme sea states from shipping and oil platforms are far more numerous [101, 16, 98].

Currents travelling against the direction of wave propagation (adverse currents) are known to increase their amplitude and decrease their wavelength, steepening waves [102]. Although well-studied theoretically, experimental studies on the effect of velocity variations (shear) within currents on wave behaviour are less prevalent. This thesis assumes a linearly sheared current and measures the propagation of weakly nonlinear waves on these currents. Crossing seas often occur when wave systems in the ocean meet after being radiated from different sources, such as wind and swell. The interaction between systems is thought to provide a mechanism for the formation of extreme events and to increase the elevation of already very large crests. Although the field of hydrodynamics is the primary focus of this thesis, because the equations governing surface waves are applicable to all dispersive media, there are analogies in other dispersive media, such as optics, Bose-Einstein condensates, and plasma [26, 94, 72, 47].

Of the media in which rogue waves are predicted or have already been observed, hydrodynamics is by far the most widely studied, optics being a close second. Rogue waves in optical fibres were first observed as large high-frequency tails in optical intensity spectra [114], a well-established measure of the likelihood of rogue waves [91]. Since the pioneering work of Solli et al., (2007) rogue waves have been studied extensively in many fields within optics [7]. As in hydrodynamics, the sudden emergence of optical rogue waves can have unexpected consequences in the multitude of electrical systems in which they exist giving rise to attempts at their control [113]. For further context on the formation of rogue waves in the field of optics, [41, 7] provide excellent reviews. The fields of optics and hydrodynamics are then bridged together in the review by Dudley et al., 2019 [43].

1.1.2 Surface gravity waves - an overview

In this background section, an overview is given of the equations governing surface gravity waves along with their underlying assumptions and applicability. For details of the derivation of the classical wave equations, the reader is directed to the excellent, in-depth review by Craik, 2004 [33].

In deriving the water-wave equations governing surface gravity waves, the water is first assumed to be incompressible and, with the exception of Chapter 2, irrotational. The governing equation is the Laplace equation, $\nabla^2\phi = 0$, which should be satisfied for the entire domain. The flow domain of the water has a solid, uniform bed at its lower boundary and a free surface at its upper boundary. The following boundary conditions apply. Firstly, the lower boundary condition ensures no water passes vertically through the solid bed,

$$\phi_z = 0, \text{ at } z = -d, \tag{1.1}$$

where ϕ is the velocity potential, z the vertical coordinate, d the depth, and subscripts denote partial derivatives. The dynamic free surface boundary condition balances pressures at the surface,

$$\Phi_t + \frac{1}{2}\Phi_x^2 + \frac{1}{2}\Phi_y^2 + \frac{1}{2}\Phi_z^2 + g\eta = 0, \text{ for, } z = \eta(x,y,t), \tag{1.2}$$

where Φ is the potential at the surface (η), g is the gravitational constant and x, y and t are the horizontal, vertical, and time coordinates. The kinematic free surface boundary condition defines the free surface,

$$\eta_t + \Phi_x\eta_x + \Phi_y\eta_y - \Phi_z = 0, \text{ on } z = \eta(x,y,t). \tag{1.3}$$

Incompressibility, irrotationality, and inviscidity make these governing equations appropriate for potential theory.

1.1.2.1 Linear wave theory

For unidirectional waves, a linear potential solution and free surface elevation applicable to low amplitude waves is readily obtained from the governing equations. As a function of depth, z, horizontal distance, x, and time, t these are,

$$\phi(x,z,t) = \frac{\omega}{k}\frac{\cosh[k(z+d)]}{\sinh kd}\left[-\frac{1}{2}\left[iae^{i(kx-\omega t)} + c.c.\right]\right] \tag{1.4}$$

$$\eta(x,t) = \frac{1}{2}\left\{a\ \exp[i(kx-\omega t)] + c.c.\right\}, \tag{1.5}$$

where a is the complex wave amplitude (having magnitude and angle), ω its frequency, k its wavenumber, and *c.c.* denotes the complex conjugate. In order to satisfy the linearized dynamic free surface boundary condition, the linear dispersion relation for arbitrary depth must be satisfied,

$$\omega^2 = gk\tanh kd. \tag{1.6}$$

By definition, the phase velocity of a wave is the ratio between frequency and wavenumber and so linear wave evolution is defined by this dispersion relation. If the wavelength, $\lambda = 2\pi/k$, is much smaller than the depth, the water can be assumed deep ($kd >> 1$) and the linear dispersion relation becomes $\omega^2 = gk$.

Having linear properties, solutions can be superimposed to create a wave system comprised of multiple components each with their own frequency, amplitude, and phase. Directionality can be added to the system with wavenumbers along both an x-axis, (k_x) and y-axis, (k_x). These component wavenumbers must satisfy the dispersion relation,

$$\omega^2 = g\kappa\tanh \kappa d,\ \text{where},\ \kappa = \sqrt{k_x^2 + k_y^2}, \tag{1.7}$$

to give the three-dimensional free surface elevation,

$$\eta(x,y,t) = \frac{1}{2}\left\{a\ \exp[i(k_x x + k_y y - \omega t)] + c.c.\right\}. \tag{1.8}$$

Throughout this thesis, the linear dispersion relation will be modified to make it applicable to the cases of crossing waves and waves on sheared current. By definition, the linear case that has been described does not allow temporal changes in the frequency spectrum and consequently wave stability may not be investigated.

1.1.2.2 Nonlinear wave theory: the nonlinear Schrödinger equation

In order for spectral changes to occur, nonlinear interactions between components must be considered. Nonlinear solutions to the governing equations can, for example, be obtained using the combination of a Stokes expansion and a multiple-scales analysis in which a series of individual solutions at increasing orders of a small parameter, ϵ are sought [38]. For surface gravity waves, the wave steepness, $\epsilon = ka$ is the most suitable small parameter. The form of these equations is,

$$\phi = \sum_{j=0}^{+\infty}\epsilon^j\phi_j \text{ and } \eta = \sum_{j=0}^{+\infty}\epsilon^j\eta_j, \tag{1.9}$$

where the functions, ϕ_j and η_j depend on a hierarchy of scales,

$$\vec{x}_0 = \vec{x},\ \vec{x}_1 = \epsilon\vec{x},\ \vec{x}_2 = \epsilon^2\vec{x} \tag{1.10}$$

$$\vec{x}_j = \epsilon^j\vec{x} \tag{1.11}$$

$$t_0 = t,\ t_1 = \epsilon t,\ t_2 = \epsilon^2 t \tag{1.12}$$

$$t_j = \epsilon^j t \tag{1.13}$$

At each order, new information and further accuracy in the wave evolution equations are obtained. However, this is offset by increasing difficulty in finding solutions. At $\mathcal{O}(\epsilon^1)$ the linear dispersion relation is revealed, while at $\mathcal{O}(\epsilon^3)$ the nonlinear Schrödinger equation arises. The 1D+1 NLSE often takes different forms depending on its useage as discussed in [22] (the "+1" terminology herein refers to the always present temporal dimension). The most common form of the NLSE (the space-NLSE) derived by Zakharov in 1968 for water waves (see [137]) gives the evolution of the wave envelope, A_s,

$$i\left(\frac{\partial A_s}{\partial t} + c_g\frac{\partial A_s}{\partial x}\right) + L\frac{\partial^2 A_s}{\partial x^2} + N|A_s|^2 A_s = 0, \tag{1.14}$$

where the group velocity, c_g, linear coefficient, L, and nonlinear coefficient, N, are functions of the dispersion relation evaluated at the carrier frequency (carrier properties denoted by a zero subscript),

$$c_g = \frac{\partial\omega}{\partial k}\bigg|_{k_0},\ L = \frac{1}{2}\frac{\partial^2\omega}{\partial k^2}\bigg|_{k_0} \text{ and } N = -\frac{\omega_0 k_0^2}{2}. \tag{1.15}$$

However, for the purposes of comparing numerical solutions to experimental measurements in which the wavemaker plays the role of a boundary condition at a fixed location, it is most convenient to use the time-NLSE,

$$i\left(\frac{\partial A_t}{\partial x} + \frac{1}{c_g}\frac{\partial A_t}{\partial t}\right) + \frac{L}{c_g^3}\frac{\partial^2 A_t}{\partial t^2} + \frac{N}{c_g}|A_t|^2 A_t = 0, \tag{1.16}$$

where the transformation between the space and time NLSEs is given in [22] and assumes $A_{s,0}(x) \sim A_{t,0}(-x/c_g)$ and $A_{t,0}(t) \sim A_{s,0}(-c_g t)$, where subscripts s and t denote solutions to the space and time NLSEs respectively. The linear free surface elevation is reconstructed from the wave envelope by reintroducing the carrier component,

$$\eta = \frac{1}{2}\left\{A_t e^{i(k_0 x - \omega_0 t)} + c.c\right\}. \tag{1.17}$$

In Chapter 2, the coefficients of the constant vorticity NLSE will additionally be a function of current shear. In Chapter 3 two NLSEs will be solved simultaneously to model coupled, crossing wave systems (CNLSE) and in Chapter 4 a 2D+1 version of the NLSE will be used.

The 1D+1 NLSE has well-known analytic solutions [103] including the family of breather solutions, known to increase in envelope amplitude, creating waves of 3 and 5 times their initial height [24]. These solutions are specific examples of modulational instability described by the NLSE and first discovered and described by Benjamin and Feir, in 1967 [14]. Modulational instability had since been observed by experimentalists who found that steep regular wavetrains tended to disintegrate and become irregular [136]. Benjamin and Feir investigated instability of the Stokes plane wave solution, adding infinitesimal amplitude and phase perturbations at the “perturbation wavenumber”, a small wavenumber increment from the carrier wave wavenumber. Modulational instability has been linked to increases in kurtosis, the fourth spectral moment [42]. Large values of kurtosis are known to increase the likelihood of rogue waves and this measure has been used by a number of authors investigating rogue waves in irregular seas [128, 91, 97].

1.2 Aim and objectives

This thesis aims to study experimentally the effects of crossing seas and linearly sheared currents on the dispersion and stability of surface gravity waves. In this experimental study, three different forms of the NLSE are used to design, give insight into and compare against experimental results through numerical solutions.

1.3 Synopsis

In Chapter 2, the dispersion and stability of wavetrains travelling on a vertical, linearly sheared current is investigated experimentally and compared to predictions by the constant vorticity dispersion (vor-dispersion) relation and NLSE (vor-NLSE). This is the first time results of weakly nonlinear (and nominally unstable) modulated wavetrains propagating on a linearly sheared current have been presented. In Chapters 3 and 4, the effect of directionality on dispersion and stability is investigated in two ways. In Chapter 3, the stability of two coupled, weakly nonlinear, wave systems crossing with some angle is investigated experimentally and the results compared to predictions by the coupled NLSE (CNLSE). This is the first time that experiments using the classical, modulated wave approach to stability have been performed on coupled wave systems beyond the 35.26° stability limit. In Chapter 4, wave groups with an angle between the carrier and sidebands are generated in order to observe the effect of their crossing angle on group dispersion. At 35.26° the group ceases to disperse and propagates with unchanging form as predicted by the two-dimensional NLSE (2D+1 NLSE).

In each of the three main chapters, linear stability analysis of the appropriate wavetrain (available in the literature but rederived and included for completeness) for the different NLSEs is used to determine the stability regions in the input parameter space specific to each facility being used. In addition to linear stability analysis, which gives a simplified, nonconservative estimation of spectral changes, a numerical solver specific to each NLSE was created. Prior to experimentation, the numerical solver was used to simulate results (free surface elevation and spectral data) for each test and determine whether shear and crossing were likely to have a measurable effect on stability. Following experimentation, free surface elevation data obtained from the first measurement position were used as initial conditions to the numerical solvers. The numerical solution was then obtained for the same evolution distance as experiments allowing for direct comparisons between the two. Linear stability predictions were also compared alongside experimental and numerical results. Each chapter concludes with a discussion on whether the expected stability characteristics were observed experimentally. Emphasis is given to the comparison with numerical predictions and the applicability of the relevant NLSE to the predictions of stability and extreme wave events.

Chapter 2: Modulational Stability on Linearly Sheared Currents

This chapter examines experimentally the dispersion and stability of weakly nonlinear waves on opposing current profiles that are linearly vertically sheared and thus have constant vorticity. Measurements are compared against predictions from the 1D+1 nonlinear Schrödinger equation for waves propagating on a linearly vertically sheared current (the vor-NLSE) derived by Thomas, Kharif & Manna (Physics of Fluids, **24**, 127102 (2012)). The shear rate is negative in opposing currents when the magnitude of the current in the laboratory reference frame is negative (i.e. opposing the direction of wave propagation) and reduces with depth, as is most commonly encountered in nature. Compared to a uniform current with the same surface velocity, negative shear has the effect of increasing wavelength and enhancing stability. In experiments with a single low-steepness monochromatic wave unseeded by sidebands, the dispersion relationship between wavelength and frequency is examined on five opposing current profiles with shear rates from 0 s^{-1} to -0.87 s^{-1}. For all current profiles, the linear constant vorticity dispersion relation predicts the wavenumber to within the 95% confidence bounds associated with estimates of shear rate and surface current velocity. The effect of shear on modulational stability was determined by measuring the spectral evolution of a carrier wave seeded with spectral sidebands on opposing current profiles with shear rates between 0 s^{-1} and -0.48 s^{-1}. numerical solutions of the vor-NLSE are consistently found to predict sideband growth to within two standard deviations across repeated experiments for all current profiles and all sideband frequencies examined. The vor-NLSE predicted experimental observations better than its uniform-current NLSE counterpart. Similarly, the amplification of experimental wave envelopes along their evolution distance is predicted well by numerical solutions of the vor-NLSE, and consistently significantly over-predicted by the uniform-current NLSE.

Chapter 3: Modulational Stability in Crossing Seas

The coupled nonlinear Schrödinger equation (CNLSE) is a wave envelope evolution equation applicable to two crossing, narrow-banded wave systems. Modulational instability, a feature of the nonlinear Schrödinger wave equation, is characterized (to first order) by an exponential growth of sideband components and the formation of distinct wave pulses, often containing extreme waves. Linear stability analysis of the CNLSE shows the effect of crossing angle, θ, on MI, and reveals instabilities between $0^\circ < \theta < 35^\circ$, $46^\circ < \theta < 143^\circ$, and $145^\circ < \theta < 180^\circ$. Herein, the modulational stability of crossing wavetrains seeded with symmetrical sidebands is determined experimentally from tests in a circular wave basin. Experiments were carried out at 12 crossing angles between $0^\circ \leq \theta \leq 88^\circ$, and strong unidirectional sideband growth was observed. This growth reduced significantly at angles beyond $\theta \approx 20^\circ$, reaching complete stability at $\theta =$ 30–40°. We find satisfactory agreement between numerical predictions (using a time-marching CNLSE solver) and experimental measurements for all crossing angles.

Chapter 4: Nondispersive Crossing Waves

Stationary wave groups exist in a wide range of nonlinear dispersive media, most notably in optics, Bose-Einstein condensates, plasma, and hydrodynamics. They are often referred to as solitons because the steady shape of the waves is maintained as a result of a balance between dispersion and nonlinearity. Hydrodynamic solitons have been widely investigated, particularly when assuming unidirectionality of the wave field. In two-dimensional propagation, the observation of stationary wave groups becomes more difficult because of the presence of dispersion and diffraction. This chapter reports experimental observations of nonlinear gravity-driven X-waves, i.e., X-shaped wave envelopes that propagate with constant form on the water surface in deep water. These can be constructed and described within the framework of higher-dimensional nonlinear Schrödinger equations (NLSEs) in a regime of vanishing dispersion. In fact, the 2D+1 NLSE predicts a balance between dispersion and diffraction when the envelope consisting of the arms of the X travel at an angle of $\pm\text{atan}(1/\sqrt{2}) \approx \pm 35.26^\circ$ to the direction of travel of the carrier wave. Moreover, this chapter analyses in detail the single crossed-wave component and finds that the frequency dispersion decreases to a minimum at the nondispersive crossing angle of approximately ±35.26°. Our results may motivate similar investigations in other physical media, governed by weakly nonlinear evolution equations and improve understanding of the lifetime of extreme events in directional seas.

Chapter 5: Conclusions

In the final chapter, results from each experimental campaign are put into context with a focus on offshore renewable energy. Recommendations for future work are made.

Publications arising from this thesis

- Steer, J. N., McAllister, M. L., Borthwick, A. G. L., & van den Bremer, T. S., (2019) Experimental Observation of Modulational Instability in Crossing Surface Gravity Wavetrains *MDPI Fluids,* 4(2):105
- Steer, J. N., Borthwick, A. G. L., Stagonas, D., Buldakov, E., & van den Bremer, T. S. (under review), Experimental Study of Dispersion and Modulational Instability of Surface Gravity Waves on Constant Vorticity Currents *Journal of Fluid Mechanics.*
- Steer, J. N., Borthwick, A. G. L., Chabchoub, A., Onorato, M., & van den Bremer, T. S. (forthcoming), Hydrodynamic X-Waves *Physical Review Letters.*

Other relevant publications

- Chabchoub, A., Mozumi, K., Hoffmann, N., Babanin, A. V., Toffoli, A., Steer, J. N., van den Bremer, T. S., Akhmediev, N., Onorato, M., & Waseda, T., Directional Soliton and Breather Beams, *Proceedings of the National Academy of Sciences of the United States of America,* (2019)

Chapter 2

Modulational Stability on Linearly Sheared Currents*

2.1 Introduction

Interactions between opposing waves and currents have long been known as potentially hazardous to shipping. In 2015 the Cemfjord cement carrier was found capsised in the Pentland Firth of Scotland; the concluding report stated that "Cemfjord capsised suddenly and rapidly at 13.16 on 2nd January 2015 when it encountered extraordinarily violent, breaking seas (...) created by gale force winds opposing a strong ebb tidal stream" [86]. While these effects of opposing waves and currents on shipping have been understood qualitatively by seafarers for centuries, only in the latter half of the 20th century, did these interactions become the subject of research (as reviewed in the seminal papers, [102] and [104]). Waves meeting an opposing current are known to increase in amplitude, a, and wavenumber, k, a combination which causes an overall increase in steepness, $\epsilon \propto ka$. The relationship between wavenumber and frequency (dispersion relation) is fundamental to the evolution of dispersive waves through all media, and thus wave-current interactions are important, as they affect the dispersion relationship. Additionally, the increase in steepness not only makes waves more prone to violent breaking but can also bring otherwise linear waves into a parameter space subject to amplitude-dependent nonlinear effects such as modulational instability.

Modulational instability affects medium- and high- steepness, narrow-banded waves propagating on water deeper than $k_0d = 1.36$ (with k_0 being the carrier wavenumber and d the water depth). At first-order, wavetrains subject to modulational instability experience exponential amplitude growth of their sideband components, seen as a pulsing or modulation in the time domain with extreme wave crests often forming in the centre of the formed groups [14, 60]. The nonlinear Schrödinger equation (NLSE) provides the simplest framework for investigating this phenomenon and admits a number of solutions exhibiting modulational instability. One such family of analytic solutions is the 'breather wave' family named for the manner in which their envelope amplitudes (periodically) increase to 3 or 5 times that of their initial amplitude [25, 24]. Whereas breather waves require precise initial conditions to complete their prescribed evolution, unstable Stokes plane waves provide a more general context for investigating modulational instability. Stokes

---

[*] An abridged version of this chapter is under review for publication in a paper entitled—"Experimental Study of Dispersion and Modulational Instability of Surface Gravity Waves on Constant Vorticity Currents", co-authored by A. G. L. Borthwick, D. Stagonas, E. Buldakov, and T. S. van den Bremer, (Journal of Fluid Mechanics)

plane waves exhibit modulational instability when sideband frequency perturbations are introduced to a carrier wave within a range of unstable perturbation wavenumbers (found through linear stability analysis) [136]. Many experiments have been carried out on the break-down of unstable wavetrains following the pioneering studies of [14, 136, 90]; and [78].

In their simplest form, sub-surface currents exist as one-dimensional and uniform with depth. Waves initially propagating on still water that begin to interact with such a uniform current, experience alterations in amplitude and wavelength in accordance with the conservation of wave action, first derived for low-steepness linear waves in [18] and [133] then subsequently extended to nonlinear waves [8]. In essence, opposing currents tend to increase amplitude and shorten wavelength, whereas for following currents the reverse is true, as captured by the uniform-current linear dispersion relationship and the conservation of wave action. In real flows that often experience bed friction and surface winds, variations in inline current velocity with depth introduce vertical shear to the flow.

The most complex forms of sheared current exist as arbitrary variations in all 3-component velocities, (U, V, W) within a fluid. Nonlinear numerical models for two-dimensional waves and arbitrary distributions of vorticity in [122] and [36] have been shown to agree very well with laboratory experiments [119]. However, their complexity generates a need for analytic approximations to the dispersion relationship. These have been derived for moderate shear [112, 75], weak shear [120] and high depth-averaged shear rates [49]. In addition to direct changes to the free surface, shear affects sea bed pressure measurements and the transfer functions used to determine free surface elevation from bottom pressure [30]. While the effect of arbitrary vorticity on determining surface elevation from pressure measurements is known [63], only recently have the pressure transfer functions and amplification factors been derived for the most general case [64]. Often, investigations into the effects of sheared current on wave behaviour constrain current velocity variation to one dimension.

Horizontally sheared currents can take the form of inline velocities that vary either along the axis of wave propagation or perpendicular to it. Propagation of waves across an inline horizontally sheared current ($\mathrm{d}U/\mathrm{d}x \neq 0$) and onto an opposing current has the effect of steepening waves by the conservation of wave action. Experiments have shown this process to trigger rogue waves in random unidirectional Gaussian wave spectra [129] as well as to destabilise regular wavetrains [97]. Jet-type horizontally sheared currents ($\mathrm{d}U/\mathrm{d}y \neq 0$) are known to exist in the Agulhas current around the South African east coast [85]. These jet currents are of interest as a possible mechanism of rogue wave formation through wave trapping [111].

Assuming a steady, one-dimensional, linearly-varying current velocity with depth (constant vorticity) allows the addition of irrotational perturbations (in the form of waves) and therefore the assumption of a potential fluid and the simplified governing equations this implies [48]. For a rotational flow of constant vorticity, the dispersion equation for linear waves was first derived independently by both [124] and [15]. The evolution of steep waves on constant shear has been investigated numerically (using the Euler equations) [35, 130, 34], and its effect on modulational stability found to be destabilised by positive shear and vice versa [28]. It should be noted that linear waves initially on still water approaching an opposing constant vorticity current are steepened in a similar manner to the uniform-current case, by wave action conservation altered for constant vorticity [106].

The same effects of constant vorticity on wave stability found through numerical analysis have been found through constant vorticity NLSEs (so-called vor-NLSEs) as derived analytically for infinite depth and studied numerically for arbitrary depth in [13]. Thomas, Kharif, and Manna in [123] (henceforth TKM12) derived a constant vorticity NLSE with coefficients expressed as explicit functions of the carrier wave properties, vorticity, and depth, which is the starting point of the present chapter. Linear stability analysis of the vor-NLSE has also shown that when the ratio of shear, Ω, to carrier wave frequency, $\tilde{\omega}_0$ (in the surface current reference frame, denoted with tilde) is less than $-2/3$ rad^{-1} (i.e. $\Omega/\tilde{\omega}_0 < -2/3$ rad^{-1}) wavetrains become entirely stabilised regardless of perturbation wavenumber or depth.

Further to the aforementioned Doppler shift of waves propagating on a current, a two-way exchange of energy and momentum between waves and currents may create a velocity field more complex than the simple superposition of individual periodic and mean flow solutions (see [70, 32] for the literature discussing such interaction). Coupled nonlinear interaction equations for plane waves on uniform currents have been derived by [10, 9] and predict reductions in current velocity during adverse wave-current interaction and vice versa. The change in shear rate of constant vorticity currents and colinear waves has been measured in experiments by [76] using laser Doppler velocimetry. [58] compare these experiments to numerical solutions of the equation they derive based on the generalised Lagrangian mean, finding good agreement and showing an increase in vertical shear near the surface in adverse currents and vice versa. In this study, we do not consider the effect of the waves on the current's magnitude and shear rate and acknowledge that full velocity field measurements in the presence of waves could improve the robustness of our conclusions.

This chapter investigates experimentally the propagation of medium-steepness weakly nonlinear waves on a current profile that is steady, one-dimensional, has constant vorticity and opposes the wave direction. The steepening behaviour that takes place as the waves come into contact with the current is not examined. Instead, the focus is placed on the evolution of the waves once they are on the current. In doing so, the effect of a vertical shear is investigated and not the magnitude of the current itself. In particular, the effects of vertical shear on the (linear) dispersion relationship and on the occurrence of modulational instability are investigated experimentally in parts I and II of this chapter respectively. It is found that in all experiments, the constant vorticity equations predicted linear wave evolution and stability very well, out-performing the zero vorticity equations.

This chapter is laid out as follows. Section 2.2 reviews the derivation of the constant vorticity nonlinear Schrödinger equation (vor-NLSE) and the constant vorticity dispersion (vor-dispersion) relationship. Section 2.3 discusses the method used to create a linearly sheared currrent profile, collect wavelength and frequency measurements from low-steepness regular waves, and measure the stability of weakly nonlinear modulated waves. Section 2.4 discusses the linear and weakly nonlinear wave evolution measurements and how both compare to predictions by constant vorticity and zero vorticity equations. Finally, conclusions are drawn in Section 2.5.

2.2 Theoretical model

2.2.1 Coordinate system and reference frames

Figure 2.1 presents the coordinate system used in both the laboratory and the surface current reference frames. The system is assumed two-dimensional, such that it is invariant along the transverse y-axis. The location of the still water level is at $z = 0$, the free surface elevation at $z = \eta(x, t)$, and the bed at $z = -d$. The constant vorticity wave equations (vor- equations) are typically derived in the surface current reference frame. In the laboratory reference frame, the steady, inline current profile, $U(z)$ with constant shear, $\Omega = \mathrm{d}U/\mathrm{d}z$, is prescribed in the x-direction. This constant surface current velocity, U_0 and shear rate, Ω define the current field as,

$$U = U_0 + \Omega z. \tag{2.1}$$

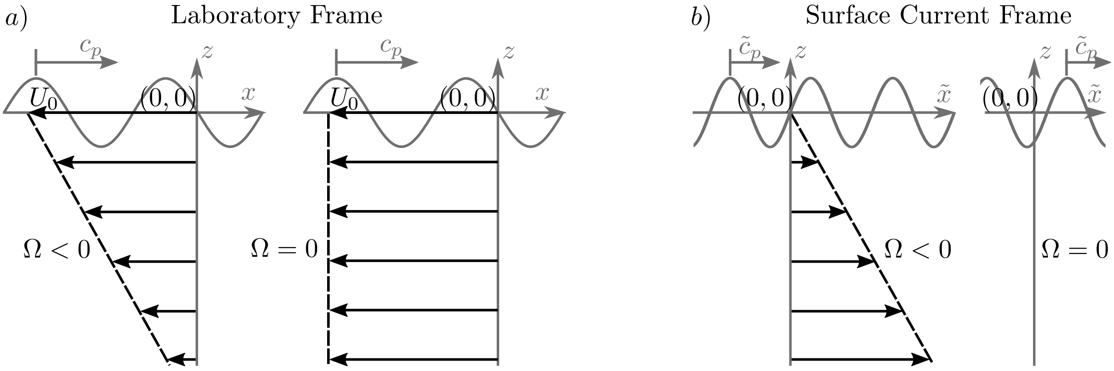

Figure 2.1: Schematic of laboratory (panel a) and surface current (panel b) reference frames used herein. Both reference frames show a negatively sheared current on the left ($U_0 < 0$, $\Omega < 0$) and negative uniform current on the right ($U_0 < 0$, $\Omega = 0$) with respect to the x-direction, the direction of the wave phase velocity, c_p. The tilde denotes properties measured within the surface current reference frame.

All experiments presented herein consider waves propagating in the positive x-direction, while current profiles are opposing, and associated velocities are therefore negative. Wave frequencies measured in the laboratory reference frame, ω can be related to wave frequencies in the surface current reference frame, $\tilde{\omega}$ using a simple Doppler shift,

$$\omega = \tilde{\omega} + U_0 k, \tag{2.2}$$

where k is wavenumber, and the tilde denotes properties measured in the surface current reference frame.

2.2.2 Governing equations and boundary conditions

In general, potential flow theory cannot be used in the presence of vorticity. The one exception is a strictly two-dimensional flow with waves travelling either exactly opposing or inline with the current and with the current's vorticity being constant in time and space, as considered here. The total velocity field $\boldsymbol{u}$ can be written as the sum of a rotational current and irrotational water waves: $\boldsymbol{u} = U(z)\hat{\boldsymbol{\imath}} + \boldsymbol{\nabla}\phi$, where $\hat{\boldsymbol{\imath}}$ is the unit vector in the x-direction and ϕ is the potential of the waves. The potential, ϕ of the system must satisfy the Laplace equation, $\nabla^2\phi = 0$ in the range $-d < z < \eta(x,t)$ and is related to the streamfunction of the waves, ψ through the Cauchy-Riemann equations. Kelvin's circulation theorem shows that an irrotational streamfunction can be assumed when vorticity within the flow is constant in space and time [34]. The standard bottom boundary condition, $\phi_z = 0$ at $z = -d$ prevents flow through the bed. At the surface, the kinematic and dynamic boundary conditions are respectively,

$$\eta_t + (\Phi_x + \Omega\eta)\eta_x - \Phi_z = 0 \quad \text{and} \quad \Phi_t + \frac{1}{2}\Phi_x^2 + \frac{1}{2}\Phi_z^2 + \Omega\eta\Phi_x + g\eta - \Omega\Psi = 0 \quad \text{for} \quad z = \eta(x,t), \tag{2.3a,b}$$

where $\Psi \equiv \psi(z = \eta(x,t))$ and $\Phi \equiv \phi(z = \eta(x,t))$ denote their respective lower case variables evaluated at the free surface, and g is the gravitational constant.

2.2.3 Solutions using perturbation methods

2.2.3.1 Linear solutions: frequency dispersion

Assuming a carrier wave with amplitude a_0, wavenumber k_0, and frequency $\tilde{\omega}_0$, a Stokes expansion in steepness, $\epsilon = a_0 k_0$ gives at first-order the linear, constant vorticity, arbitrary-depth vor-dispersion relation (first derived by [15] and [124]),

$$\tilde{\omega}_0^2 + (\tilde{\omega}_0 \Omega - g k_0) \tanh k_0 d = 0. \tag{2.4}$$

By relating wave frequency to wavenumber, the implicit vor-dispersion relation describes the evolution of linear waves ($\epsilon \ll 1$), where nonlinear changes to the dispersion relationship and instability do not play a role. Throughout the present work, frequencies and wavenumbers are computed from (2.2) and (2.4).

2.2.3.2 The vor-NLSE

Performing a combined Stokes and multiple-scales expansion, [13] (for deep water) and subsequently TKM12 (for arbitrary depth) derived a NLSE with coefficients reflecting the presence of vorticity: the vor-NLSE. In their derivations, a carrier wave varying on the fast scales x, and t is modulated by a wavepacket evolving on the slow spatial and temporal scales,

$$\xi = \epsilon(\tilde{x} - \tilde{c}_g t) \quad \text{and} \quad \tau = \epsilon^2 t, \tag{2.5a,b}$$

where the group velocity, $\tilde{c}_g$, and the slow scales are defined in the reference frame of the surface current, as denoted by the tilde. At third-order in the small parameter ϵ, the nonlinear evolution of a narrow-banded wavepacket of amplitude, A is described by the constant vorticity NLSE (vor-NLSE) with linear coefficient, L, and nonlinear coefficient, M, (TKM12),

$$iA_\tau + L A_{\xi\xi} - M|A|^2 A = 0. \tag{2.6}$$

For brevity, only coefficients for deep water are presented here,

$$L = -\frac{\tilde{\omega}_0 (1+\bar{\Omega})^2}{k_0^2 (2+\bar{\Omega})^3} \quad \text{and} \quad M = \frac{\tilde{\omega}_0 k_0^2}{8(1+\bar{\Omega})} \left(4 + 10\bar{\Omega} + 8\bar{\Omega}^2 + 3\bar{\Omega}^3\right), \tag{2.7a,b}$$

where $\bar{\Omega} = \Omega/\tilde{\omega}_0$. The arbitrary-depth coefficients (used for all calculations herein) can be found in TKM12 (their (48)-(58)) and Appendix A of this thesis. The first-order free surface is reconstructed using,

$$\eta^{(1)} = \mathrm{Re}\left[\epsilon A(\xi, \tau) e^{i(k_0 \tilde{x} - \tilde{\omega}_0 t)}\right]. \tag{2.8}$$

2.2.3.3 Linear stability analysis of the vor-NLSE

To investigate the effect of shear on the stability of the vor-NLSE, a linear stability analysis of the Stokes wave solution, $A = a_0 \exp\left(-iMa_0^2\tau\right)$, is performed by perturbing the wavetrain by a sideband wave of infinitesimal amplitude and phase shift,

$$A = [a_0 + \delta(\tau, \xi)] e^{-iMa_0^2\tau}. \tag{2.9}$$

The perturbation solution, δ, is assumed to take the periodic form, $\exp\left(i(K\xi - \tilde{\gamma}\tau)\right)$, and from this, the relationship between perturbation wavenumber, K and perturbation frequency, $\tilde{\gamma}$ is found (first presented in TKM12),

$$\tilde{\gamma} = \pm\sqrt{K^2L(K^2L + 2Ma_0^2)}. \tag{2.10}$$

When $\tilde{\gamma}$ is imaginary and negative, sideband amplitudes grow exponentially in time, τ. At depth parameter, k_0d, the sideband growth rates in the (K, Ω) domain can be defined. Figure 2.2 presents both the growth rates for $k_0d = 3$ (the depth parameter used herein) and experimental parameters used in part II experiments. For each shear rate, the maximum instability, $\gamma_{\max} = Ma_0$, is achieved at the perturbation wavenumber, $K = a_0\sqrt{-M/L}$. In deep water and with zero shear, this reduces to the well-known result of $\gamma_{\max} = \omega_0 k_0^2 a_0^2/2$ at $K = 2k_0^2 a_0$ [136]. Figure 2.2 shows the generally destabilizing effect of positive shear whereby the growth rate of previously unstable regions increases and the region of instability expands to include previously stable perturbation wavenumbers; on negatively sheared current the reverse is true. Additionally, complete stability is reached at a vorticity of $\Omega/\tilde{\omega}_0 = -2/3$ rad^{-1}, and this stability boundary is insensitive to the perturbation wavenumber.

Although a useful tool in determining first-order stability characteristics, linear stability analysis is non-conservative and does not provide information on the long-term behaviour of the system. A long-term recurrence phenomenon known as Fermi-Pasta-Ulam (FPU) recurrence [52] is revealed by a nonlinear stability analysis on the NLSE [69]. In FPU recurrence, energy is periodically transferred from sideband waves back to the carrier wave over the evolution of many wavelengths [53]. For the limited evolution distances in all experiments presented herein, we do not expect to observe FPU recurrence. Numerical time-marching solutions to the NLSE also show the emergence of secondary sidebands at multiples of the primary sideband frequency, if run for a longer duration than considered herein. Spectral asymmetry in sideband evolution has also been observed experimentally in the absence of shear [79, 90], however cannot be modelled by the NLSEs due to their narrow-banded spectrum assumptions. The Dysthe equation (or modified NLSE) derived by [45] lifts these restrictions and asymmetric sideband growth has been observed numerically using the Dysthe equation [81]. Such asymmetric sideband growth has been observed in this study but was not significant and the absence of a constant vorticity Dysthe equation meant that it could not be comprehensively studied (see Appendix D for measurements of sideband asymmetry).

2.3 Experimental methodology

The experiments aim to determine the effect of vertical, linearly sheared current on the frequency dispersion of low-steepness linear waves and the stability of weakly nonlinear wavetrains. To achieve this, three stages are defined: current creation, in which a suitable current profile is sought; linear dispersion (part I), in which the dispersive behaviour of linear (low-steepness) waves is measured; and, ultimately, modulational stability (part II), in which the behaviour of weakly nonlinear waves is examined.

2.3.1 Wave-current facility

The wave-current flume in the Department of Mechanical Engineering at University College London (UCL) is used for all experiments considered in this chapter. The flume consists of a recirculating current system and two force-feedback wavemakers capable of both generation and absorption as laid out in the facility schematic (figure 2.3). Current is recirculated underneath the flume by three parallel 0.3 m diameter pipes and three impeller pumps, before passing

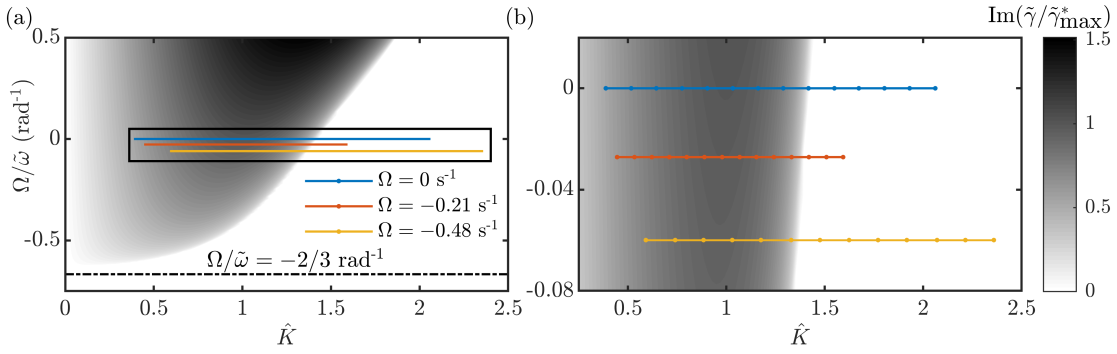

Figure 2.2: Sideband growth rate, $\tilde{\gamma}$ normalised by the maximum growth rate at zero shear, $\tilde{\gamma}^*_{\mathrm{max}} = M^* a_0^2$, as a function of normalised perturbation wavenumber, $\hat{K} = K/\left(a_0\sqrt{-M^*/L^*}\right)$ and shear rate, $\Omega/\tilde{\omega}_0$, where M^* and L^* are the linear and nonlinear vor-NLSE coefficients evaluated at depth, $k_0 d = 3$ and $\Omega = 0$ s^{-1}. The normalised maximum growth rate for zero shear is 1 at $\hat{K} = 1$ and $\Omega/\tilde{\omega}_0 = 0$. Panel (a) provides an overview of the experimental parameter range used in part II, as indicated by the coloured horizontal lines corresponding to the three current profiles used (defined in table 2.1). The solid dots in panel (b), which zooms in on the rectangular box in panel (a), indicate individual experiments (see §2.4.2).

through turning vanes and upwelling into the bottom of current conditioning units. The flume has width, $w = 1.2$ m, a working depth, $d = 0.5$ m, and wavemaker-to-wavemaker length of 16 m. It should be noted that the current conditioning units limit the working length of the flume to approximately 9 m. The first wave gauge defines the x-axis origin, and all horizontal distance measurements along the flume are given with reference to this point. Steel rails allow wave gauges to be fixed 0.3 m from the flume side.

Having a width of 1.2 m, wave energy dissipation in the facility arising from side-wall friction (the dominant source of dissipation [66]) was considered. Linear waves are known to undergo exponential amplitude attenuation due to side-wall friction; high-frequency waves being attenuated more than low-frequency waves [66]. Additionally, [59] suggest that modulational instability may be entirely stabilised by any form of dissipation. [74] show theoretically and experimentally that a perturbation from precise initial conditions causes a phase shift to FPU recurrence and, in the case of the spatially localised Akhmediev breather, induces FPU-type recurrence, where it would otherwise not occur. However, the evolution distance of our experiments did not allow for long-term recurrence effects to be observed. Using the equations presented in [66], we estimate frictional attenuation to be no more than 3% along the working length of the flume. Additionally, the propagation of regular waves at $k = 6.0$ rad m^{-1} (the carrier wavenumber in all experiments in part II) was recorded on each current profile, and attenuation was found to be smaller than the variation between the four repeated experiments and thus undetectable.

2.3.2 Current

2.3.2.1 Current conditioning

Figure 2.4 shows a current conditioner positioned above the outlet turning vanes. The system of current conditioning described herein has been employed in previous experiments at the facility and is described in detail by [115] and [109]. Each conditioning unit spans the width of the flume

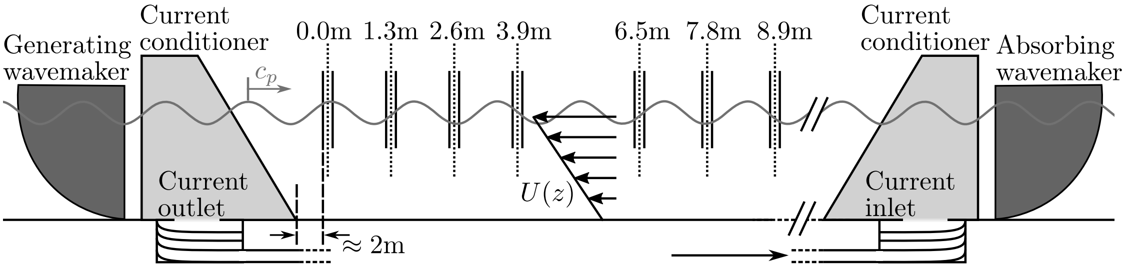

Figure 2.3: Schematic diagram illustrating the wave-current flume at UCL configured for a typical case of currents (with inline velocity, $U(z)$) opposing wave phase velocity, c_p. Individual wave gauges are denoted by solid vertical lines. Gauges are arranged in pairs separated by 0.15 m to allow estimates of the incident and reflected free surface elevation at the mid-point of each gauge pair (denoted by the dotted vertical lines).

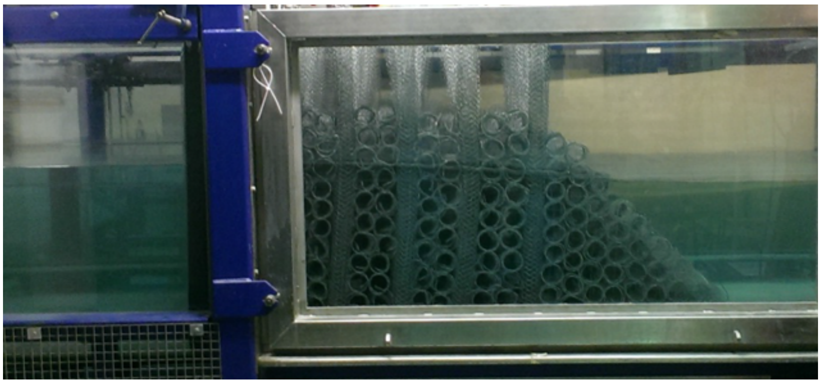

Figure 2.4: Current conditioning unit located above the outlet of the wave-current flume at the UCL Mechanical Engineering Department. Porous mesh cylinders make up the bulk conditioner (left) and triangular current shaping portion (right). The locations of the units are shown in the facility schematic of figure 2.3.

and consists of a rectangular bulk conditioner whose primary purpose is to reduce turbulence and distribute current evenly as it enters the flume. The rectangular unit abuts onto a triangular current-shaping unit. The bulk conditioner is constructed from porous wire mesh cylinders of diameter ≈ 0.1 m. During construction, pairs of horizontal cylinders are laid transversely across the flume and additional cylinders stacked on top, the stack reaching an elevation well above the still water level. Along the flume, the stacks are separated by 0.1 m gaps in which vertical porous mesh cylinders are placed. The current shaping unit consists of porous mesh cylinders placed horizontally across the flume and stacked to form a right-angled triangle. The current conditioners were optimised to generate current profiles which do not change considerably along the flume and have a significant linear portion.

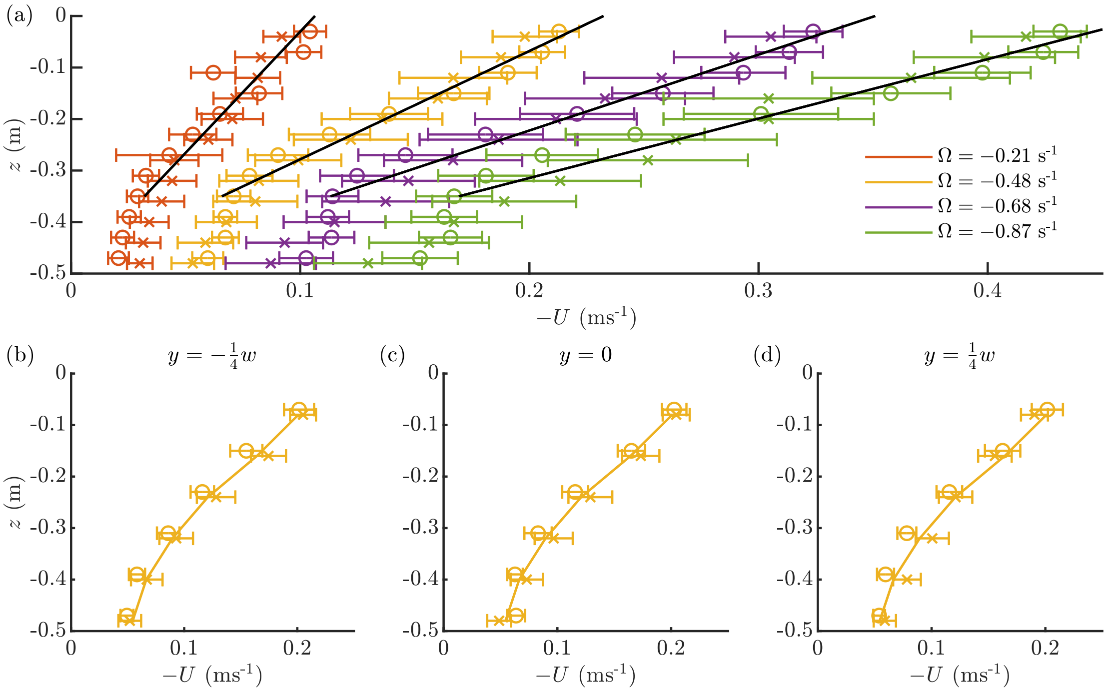

Figure 2.5: Measured current velocity profiles used in experiments presented herein. Open circles represent mean measurements taken at $x = 0$ m and crosses at $x = 9$ m. Error bars span one standard deviation calculated across the 60 s velocity record. **(a):** All non-zero velocity profiles. Solid black lines represent the linear regression used to estimate the shear rate. All measurements were taken midway across the flume (at $y = 0$ m). **(b-d):** The $\Omega = -0.48$ s^{-1} current profile measured at one quarter, midway and three-quarters across the width of the flume, w, namely at $y/w = -1/4$, 0 and 1/4. The (identical) solid lines correspond to the mean current profile measurement across all 6 locations.

2.3.3 Current profile approximation

Experiments were conducted with opposing currents (with negative surface current velocity), because the effective length of evolution in the following-current case was considered too short to observe any nonlinear effects. Five current profiles were created and will be referred to herein by their shear rates, Ω: 0 (zero current), -0.21, -0.48, -0.68, and -0.87 s^{-1}. These values can be found, along with their associated surface current velocities, in table 2.1 where the 95% confidence bounds of both parameters are also given.

Acoustic Doppler velocimetry (ADV) was used to measure the depth-varying, three-component velocity profiles at two positions defined by the coordinates, (x, y, z) along the flume centreline: at $(0, 0, z)$ m and at $(9, 0, z)$ m (with $y = 0$ corresponding to midway across the flume). As the fastest current profile used in the stability experiments, the -0.48 s^{-1} shear current profile was also measured at three positions across the flume to assess three-dimensional effects. Velocity measurements through the flume depth were taken from the bed in consecutive 0.04 m vertical increments to the free surface. At each position, all three velocity components, (U, V, W), were measured at 200 Hz for one minute. Prior to each current profile change, the flume was allowed

Ω ($\mathrm{s^{-1}}$)	U_0 ($\mathrm{m\,s^{-1}}$)
0	0
-0.21 ± 0.01	-0.11 ± 0.01
-0.48 ± 0.01	-0.22 ± 0.01
-0.68 ± 0.02	-0.33 ± 0.01
-0.87 ± 0.04	-0.44 ± 0.01

Table 2.1: Mean and associated 95% confidence bound values of surface current velocity, U_0 and linear shear rate, Ω for the 5 current profiles used in experiments.

to settle for one hour to reach a steady state, at which time seeding material was added.

Figure 2.5 presents the mean and standard deviation values of the inline velocity, U, as calculated from the full time-series data. The shear rate, Ω, and surface current, U_0, fully define the linearly varying approximation of each current profile and are presented in table 2.1 along with their 95% upper and lower confidence bounds. The shear rate was estimated using a linear regression fit through the current's upper, linear portion. The deeper in the fluid, the smaller the effect of the current's velocity and shear rate on wave phase velocity [117]. Excluding current data below $z = -0.35$ m from the linear regression fit allows an accurate estimation of shear rate (see Appendix B for a detailed estimation of the small resulting error based on the Rayleigh equation [112]). Surface current was estimated using a smoothing spline fitted through the entirety of the depth-varying current data.

2.3.4 Part I. Linear dispersion relation

By observing the relationship between frequency and wavenumber for low-steepness regular waves, experimental estimates of the vor-dispersion relation (2.4) are obtained. For all five current profiles, regular waves with input frequencies between the wavemaker's low-frequency mechanical limit and the high-frequency wave-blocking limit ($3.6 < \omega < 9.4$ $\mathrm{rad\,s^{-1}}$) were selected. Wave blocking occurs when opposing current velocities exceed the wave group velocity and wave energy is not capable of propagating forward. Free surface elevation data were both recorded and displayed in real-time at two gauges spaced at the estimated wavelength of the generated wave. The wave gauge pair spacing was then adjusted to bring both free surface measurements into phase, and this distance (now at precisely one wavelength) was recorded. Waves at each frequency were generated at a sufficiently low amplitude ($ka \ll 0.1$) to keep behaviour primarily linear. The precise frequency in the laboratory frame was extracted from the measured free surface elevation data. To remove the effect of surface current and determine the effect of shear, this measured frequency, ω was converted to the surface current frame through (2.2). Measured dispersion relation data were compared against vor-dispersion predictions and the zero-shear dispersion relation (see §2.4.1 for discussion and figure 2.6 for results).

2.3.5 Part II. Modulational instability

In order to examine modulational instability, a 3-component wave was created consisting of a carrier wave seeded with two sideband components, akin to the classical experiments on modulational instability without shear undertaken by [136]. In particular, a medium-steepness carrier wave seeded with two symmetric sidebands was selected. The target free surface elevation given as input to the generating wavemaker was,

$$\eta(0,t) = \mathrm{Re}\left[a_0 e^{-i\omega_0 t} + a_\delta \left(e^{-i(\omega_0+\omega_\delta)t} + e^{-i(\omega_0-\omega_\delta)t}\right)\right], \tag{2.11}$$

where a_δ and ω_δ are the real sideband amplitude and sideband frequencies respectively. To maintain a periodic signal over the repeat period, R, all frequencies were defined in terms of an integer multiple N such that $f_\delta = N/R$ Hz and $\omega_\delta = 2\pi f_\delta$ $\mathrm{rad\,s^{-1}}$. For each current profile, the sideband frequency was altered across experiments to explore a range of stability regimes. Sideband frequencies are given in table 2.3 as values of N and are also shown, along with estimations of growth rate in figure 2.2. Although breather-type solutions to the NLSE would produce the most extreme amplitude growth and have been used successfully to study properties of the NLSE in the absence of shear, they require precise control of the full input signal. Such control is impeded in the present case because the waves created by the wavemaker first have to propagate onto the current (and travel through the current conditioning unit), which has a different effect on the phase and amplitude of components of different frequencies. Experimental measurements of sideband amplitude were compared with numerical solutions of the vor-NLSE and NLSE through a numerical, space-marching scheme and with predictions by linear stability analysis. The error associated with removing shear from predictions could then be quantified experimentally.

2.3.5.1 Data collection

To capture the evolution of the 3-component system, the free surface elevation was recorded across a total length of 8.9 m by 14 wave gauges arranged in 7 pairs. Wave gauges collected data for a total of 160 s at 250 Hz. A repeat period of 128 s was used to ensure high frequency resolution and thus allow a high number of sideband frequencies to be tested. To facilitate the application of simple reflection analysis (based on [56]) of the free surface elevation time series, each pair of wave gauges had a spacing of 0.15 m, and produced one incident and one reflected spectrum at a virtual gauge located at each pair's centre. Figure 2.3 presents the flume configuration for stability experiments where individual wave gauges are represented by solid, free surface penetrating lines and dotted lines represent virtual gauges.

2.3.5.2 Experimental procedure

Throughout the stability investigation, the same experimental procedure was followed across multiple days. Firstly, current was generated for one hour to homogenise the flume contents (for zero-current experiments, the flume was allowed to settle for a further hour thereafter). All wave gauges were wiped with a damp cloth to remove contaminants. To calibrate the wave gauges, the voltage of each wave gauge was recorded for 30 s at five known free surface positions.

At each current profile, 15 to 17 sideband frequencies spanning nominally stable and unstable regimes were propagated with a carrier wave. Each sideband frequency experiment was carried out 4 times on different days. Confidence bands calculated from these 4 repeats are thus indicative only. The data processing technique described below was performed on each repeat individually before a mean and standard deviation result was calculated. Between each experiment, the flume was allowed to settle for 5 min while reflections and low frequency error waves attenuated; current conditioners helped with this process.

Ω (s^{-1})	ω ($\mathrm{rad\,s}^{-1}$)	ka_0
0	7.62	0.15
-0.21	7.17	0.12
-0.48	6.63	0.10

Table 2.2: Carrier wave parameters for stability experiments (part II). All experiments were carried out at $k_0 = 6.0$ $\mathrm{rad\,m}^{-1}$ and $k_0 d = 3.0$. The average measured steepness at each shear profile is also presented.

		f_δ, (N/128 Hz)																									
Ω (s^{-1})	a_δ/a_0	0	1	2	3	4	5	6	7	8	9	10	11	12	13	14	15	16	17	18	20	22	24	26	28	30	32
0	0.1	🟦		🟦		🟦		🟦		🟦		🟦		🟦		🟦		🟦		🟦	🟦	🟦	🟦	🟦	🟦	🟦	🟦
-0.21	0.1	🟧				🟧	🟧	🟧	🟧	🟧	🟧	🟧	🟧	🟧	🟧	🟧	🟧	🟧	🟧	🟧							
-0.48	0.1	🟨	🟨	🟨	🟨	🟨	🟨	🟨	🟨	🟨	🟨	🟨	🟨	🟨	🟨	🟨	🟨	🟨									

Table 2.3: Sideband frequency parameters of stability experiments (part II), with completed experiments indicated by coloured cells. Frequencies are expressed as the integer multiple, N, of the inverse of the repeat period, R, giving $f_\delta = N/R$ Hz and $\omega_\delta = 2\pi f_\delta$ $\mathrm{rad\,s}^{-1}$ (corresponding values of the perturbation wavenumber, $\hat{K}$, are shown in Figure 2.2b). Repeat period, R, was fixed at 128 s across all experiments.

2.3.5.3 Experimental parameters

Table 2.2 details the carrier wave input parameters while table 2.3 details the sideband parameters. The primary objective when selecting the input spectra and current profiles for the stability experiments was to produce high-quality waves of medium steepness. Due to the frequency range of the wavemakers, following currents could not be considered because of the reduction in wave steepness through their interaction with waves and their small effective length of evolution, limiting experiments to negative (stabilizing) shear rates. Additionally, the wave blocking criterion, $\partial\tilde{\omega}/\partial k + U_0 \geq 0$ excluded the highest frequencies and current strengths. Unpredictable attenuation of waves through the current conditioning units and wave steepening by opposing currents meant that input amplitude selection was based on preliminary measurements of a range of input amplitudes.

Results from linear stability analysis of the vor-NLSE were used to inform stability experiment parameters and target the stable and unstable regions of the sideband frequency domain. To allow experimental parameters to be plotted on a single surface of linear stability (cf. figure 2.2), the depth parameter was kept constant at $k_0 d = 3$ across all current profiles. Constant flume depth was maintained, and input carrier frequency altered across the three current profiles to maintain $k_0 = 6.0 \pm 0.1$ $\mathrm{rad\,m}^{-1}$. The generated wavelength was checked using the method detailed in §2.3.4, and the input carrier frequency adjusted if required.

2.3.5.4 Reflection analysis

Following the collection and calibration of wave gauge time series, the 160 s free surface elevation series was cut to the final 128 s to give a periodic signal of frequency resolution 1/128 Hz containing both incident and reflected waves. Amplitude spectra were estimated from each gauge and a (linear) reflection analysis based on [56] applied to each gauge pair. The reflection analysis assumes that, at two closely spaced gauges ($\Delta x \ll \lambda$), complex amplitude spectra, A_1

and A_2, are comprised of incident, A_I, and reflected, A_R, components,

$$A_1 = A_I e^{-ik_I \Delta x/2} + A_R e^{ik_R \Delta x/2} \quad \text{and} \quad A_2 = A_I e^{ik_I \Delta x/2} + A_R e^{-ik_R \Delta x/2}, \qquad (2.12\text{a,b})$$

where the incident and reflected wavenumbers, k_I and k_R, are calculated using the relevant dispersion equation (i.e. including current and shear). The method assumes linear evolution between gauges within a pair, and linear stability analysis estimations of sideband growth across the short, 0.15m distance confirmed this assumption to be satisfactory. The use of this technique deviates from the classical method described by [56] only in that the vor-dispersion equation is used (validated in §2.4.1) to compute incident and reflected wavenumbers. Reflections were found to be largest in the zero current experiments where they comprised $5 - 10\%$ of the measured energy. This value reduced for adverse current experiments but reflection analysis was applied to all experiments regardless. All results presented include only incident waves. Following the reflection analysis, upper and lower sidebands were identified in the incident wave spectrum at the first gauge and their amplitude tracked across all seven gauge pairs.

2.4 Results

2.4.1 Part I. Linear dispersion relation

Figure 2.6 presents the measured results from part I in the form of measured wavenumbers as a function of frequency in the surface current reference frame. The measured wavenumbers are compared to the predictions by both the vor-dispersion equation and the classical uniform-current dispersion equation (using the measured surface current throughout the water column). Mean wavenumber values are represented by solid dots and error bars indicate the effect of using upper and lower surface current confidence bounds when calculating $\tilde{\omega}$ from (2.2). The vor-dispersion prediction is delineated by solid lines surrounded by shaded areas which define the error associated with use of the upper and lower shear rate confidence bounds when calculating wavenumber from (2.4). The dot-dashed lines denote the wavenumber prediction by the uniform-current dispersion relation. Normalisation by the wavenumber for zero current is performed on all wavenumbers. This normalisation allows the fractional error associated with discounting both surface current and shear rate to be clearly appreciated.

The dispersion measurements in the absence of currents exhibit almost zero deviation from the prediction of the standard arbitrary-depth dispersion relation. The greatest error in this data set is 2.6% above the predicted wavenumber. At the -0.21 s^{-1} shear rate, the zero-shear prediction begins to deviate from the vor-dispersion prediction. In general, the experimental measurements follow the trend of the vor-dispersion relation. Experimental error bars at larger frequency values ($\tilde{\omega} > 8.0$ rad s^{-1}) show that measurements lie within the error associated with the measurement of shear. The -0.48 s^{-1} shear current profile presents a much larger deviation in the zero-shear prediction with respect to experimental measurements that fall almost entirely within the shaded region associated with the vor-dispersion relation. This good agreement between experimental measurements and the vor-dispersion predictions also occurs for the -0.68 s^{-1} and -0.87 s^{-1} shear rate current profiles.

2.4.2 Part II. Modulational instability

Figures 2.7 to 2.11 present the measured and predicted evolution of the weakly nonlinear wave-trains investigated in part II. Subplots within figures are titled according to the normalised perturbation wavenumber, $\hat{K} = K/K(\tilde{\gamma}^*_{\max})$, where $\gamma^*_{\max}$ is the maximum growth rate evaluated

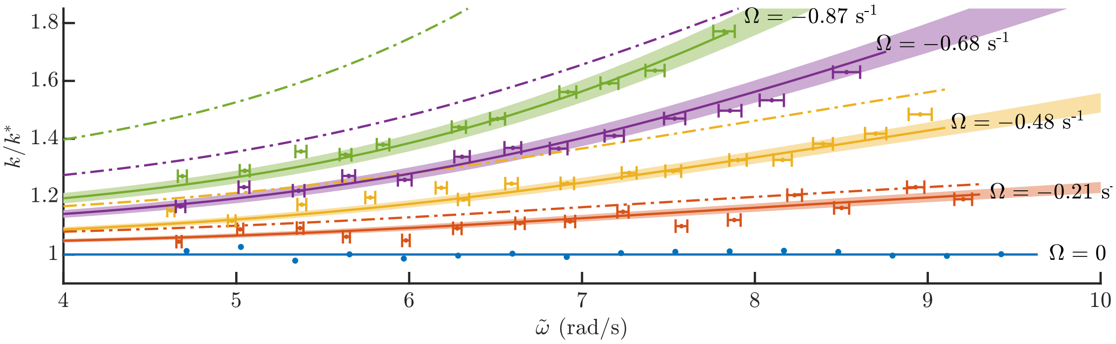

Figure 2.6: Comparison of the measured dispersion relationship (solid dots with error bars) with wavenumber predictions from the calculated vor-dispersion relationship (solid lines) and uniform-current dispersion relationship (dashed-dot lines). The wavenumbers on the y-axis have been normalised by k^*, the wavenumber predicted at zero current. The horizontal error bars represent the error associated with the surface current velocity estimation (95% confidence bounds). Similarly, the shaded areas represent the error associated with the shear rate estimation (95% confidence bound).

at $k_0 d = 3$ and zero shear (i.e. $\hat{K} = 1$ at the zero shear maximum growth rate). Normalised perturbation wavenumbers allow results to be directly related to the growth rate surface in figure 2.2. Following reflection analysis, spectral information was extracted from incident wave spectra and is compared with the predictions of a linear stability analysis of the vor-NLSE (overview in §2.2.3.3) and a space-marching numerical split-step (or pseudospectral) scheme (details in Appendix C) that solves the same equation. Both theoretical methods allow the removal of shear from their predictions in order to quantify the error associated with ignoring vertical shear. The complex amplitudes and frequencies of sidebands and carrier waves were extracted from the incident amplitude spectrum at $x = 0.0$ m; these were then used as initial conditions for both theoretical methods. The numerical scheme was executed for all experiment repetitions, and the average and standard deviation of sideband amplitude calculated across these.

Figures 2.7 to 2.9 present the evolution of seeded sideband amplitudes in both the absence of currents and in the presence of opposing currents. Averages of the upper and lower sidebands are given normalised by the initial carrier amplitude. Due to the spectral symmetry of NLSEs, individual upper and lower sidebands are predicted less well than their averages by the vor-NLSE, but are included for completeness in Appendix D. Numerical solutions of the vor-NLSE and NLSE are presented alongside experimental results. Mean amplitudes across four repeats are represented by dots (experimental) and lines (theoretical), while error bars and shaded areas represent two standard deviations from the mean for experimental and theoretical results respectively. Shaded areas are not always visible due to strong repeatability.

Figure 2.10 presents a sample of the evolution of incident envelopes (linearised by filtering bound waves and averaged over repeats) as measured experimentally and predicted through the NLSE and vor-NLSE numerical solutions by showing these envelopes at the first and final gauge. The ratio between maximum envelope amplitude at the final and first gauge gives an amplification factor associated with the perturbation wavenumber and shear rate; this amplification factor is presented for all experiments in figure 2.11. In both figures 2.10 and 2.11 the effect of shear on the formation of extreme wave crests becomes clear. Incident free surface elevation time

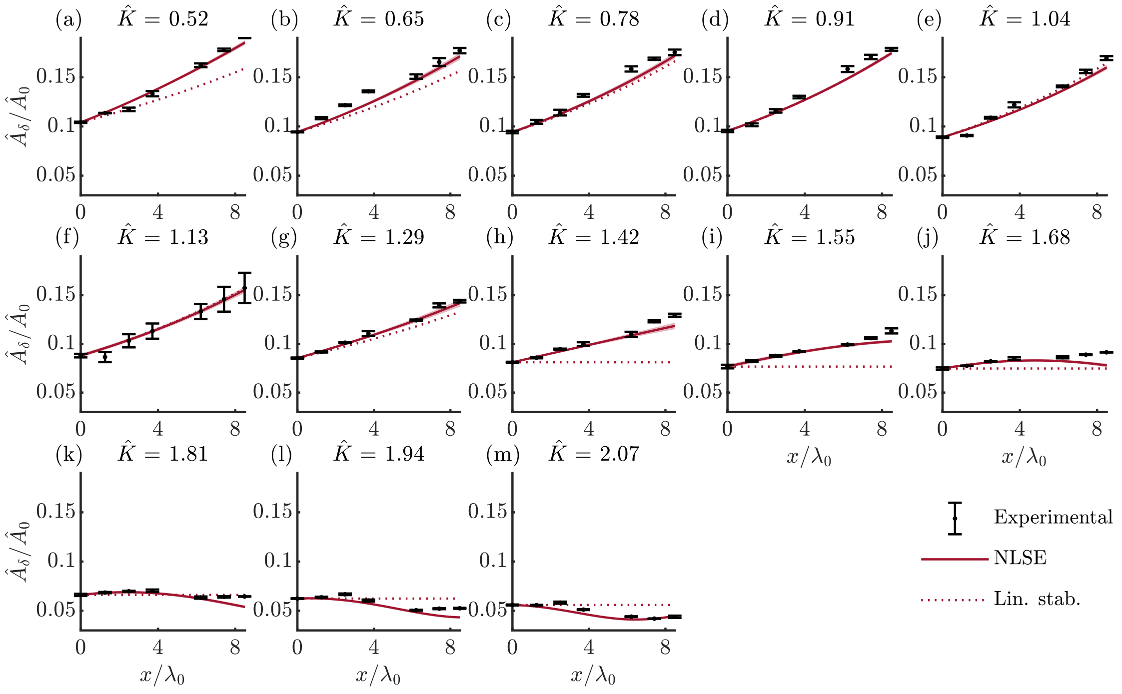

Figure 2.7: $\mathbf{\Omega = 0}$ s^{-1} : Averaged upper and lower primary sideband Fourier amplitudes, $\hat{A}_\delta$ normalised by the carrier Fourier amplitude, $\hat{A}_0$. Error bars denote two standard deviations from the mean as averaged across four repeats (part II). All sideband wavenumbers are represented as the normalised sideband wavenumber parameter $\hat{K} = K/\left(a_0\sqrt{-M^*/L^*}\right)$. Solid lines denote numerical predictions, while dotted line predictions are based on growth rates obtained from linear stability analysis.

series and associated amplitude spectra are presented in figures 2.12 and 2.13, respectively.

2.4.2.1 Zero current

Figure 2.7 presents sideband evolution in the absence of current (and shear). Growth is clearly visible through the $0.52 \leq \hat{K} \leq 1.29$ sideband wavenumber range, as predicted by linear stability analysis. Here, sideband amplitudes all increase by more than 60% with a maximum amplification by 87% occurring at $\hat{K} = 0.90$. Breaking was not observed in any experiments, and significant decay in sideband amplitude was never recorded, thus indicating the lack of (the beginnings of) FPU recurrence in the short flume. Between $1.29 \leq \hat{K} \leq 1.67$, sideband amplification reduces significantly, having crossed the theoretical stability boundary at $\hat{K} = 1.42$ (beyond which sideband amplitude behaviour is expected to become oscillatory). Such oscillations are observed in both experimental measurements and the numerical solution throughout the stable region. Across all still water experiments, small error band intervals indicate that experiments were very repeatable. Numerical solutions of the NLSE exhibit very satisfactory agreement with experimental measurements over the range of still water experiments, with predictions usually falling within two standard deviations of experimental measurements.

Figure 2.11 shows the ratio of the maximum values of the final and first gauge envelopes

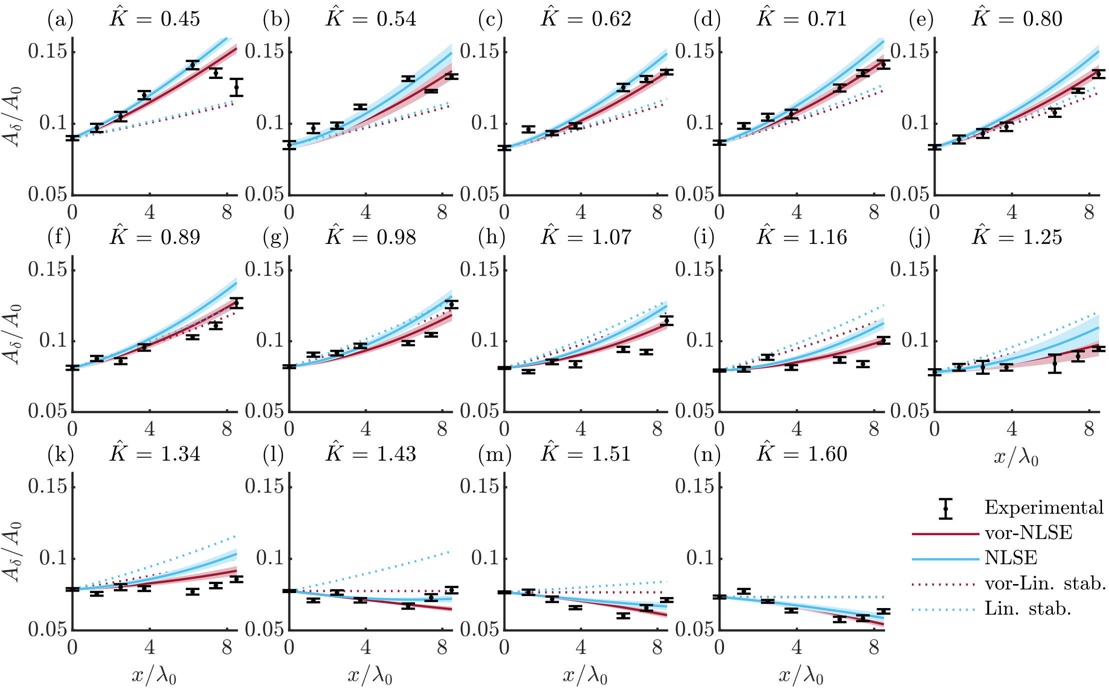

Figure 2.8: $\mathbf{\Omega = -0.21}$ s^{-1} : Averaged upper and lower primary sideband Fourier amplitudes, $\hat{A}_\delta$, normalised by the carrier Fourier amplitude, $\hat{A}_0$. Error bars denote two standard deviations from the mean as averaged across four repeats (part II). All sideband wavenumbers are represented as the normalised sideband wavenumber parameter $\hat{K} = K/\left(a_0\sqrt{-M^*/L^*}\right)$. Solid lines denote numerical predictions, while dotted line predictions are based on growth rates obtained from linear stability analysis.

presented in figure 2.10. In figure 2.11a, the experimental amplification factors show a clear downward trend following a maximal amplification factor of approximately 1.9 at $\hat{K} = 1$, the perturbation wavenumber predicted by linear stability analysis to have maximum growth at zero shear. The numerical solution to the vor-NLSE follows this trend very closely, remaining within two standard deviations throughout the unstable region ($\hat{K} < 1.4$). Similarly, the envelopes presented in figure 2.10a-d show increases in amplitude for both unstable perturbation wavenumbers (a-b); there is good agreement between experimental and numerical results. In the stable perturbation wavenumber region (figure 2.10c-d), agreement between numerical and experimental envelopes is also observed.

2.4.2.2 Opposing currents

In figure 2.8, which illustrates the sideband evolution in -0.21 s^{-1} shear rate experiments, the experimental measurements show obvious growth for perturbation wavenumbers within the range $0.45 \leq \hat{K} \leq 0.98$. Similarly, in the -0.48 s^{-1} shear rate experiments of figure 2.9, clear sideband growth is observed within the perturbation wavenumber range $0.59 \leq \hat{K} \leq 1.03$. Maximum amplifications by 21% were observed at $\hat{K} = 0.71$ and $\hat{K} = 0.59$ for the -0.21 s^{-1} and -0.48 s^{-1} shear rates respectively. Growths observed in the -0.48 s^{-1} shear experiments are predominantly

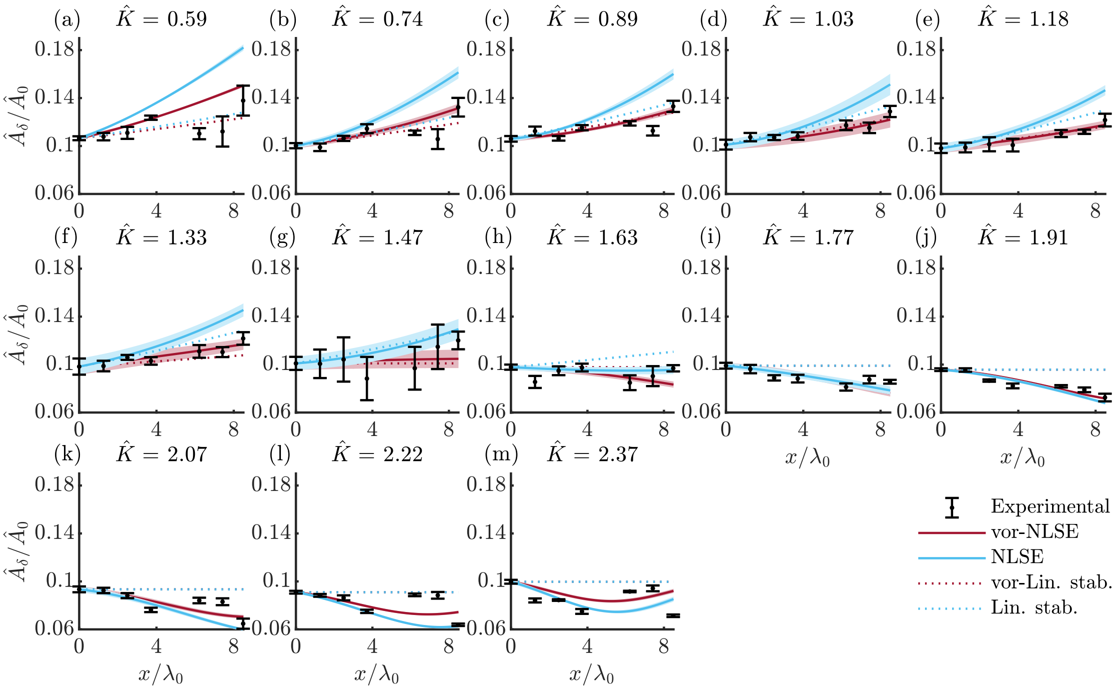

Figure 2.9: $\mathbf{\Omega = -0.48}$ s^{-1} : Averaged upper and lower primary sideband Fourier amplitudes, $\hat{A}_\delta$ normalised by the carrier Fourier amplitude, $\hat{A}_0$. Error bars denote two standard deviations from the mean as averaged across four repeats (part II). All sideband wavenumbers are represented as the normalised sideband wavenumber parameter $\hat{K} = K/\left(a_0\sqrt{-M^*/L^*}\right)$. Solid lines denote numerical predictions, while dotted line predictions are based on growth rates obtained from linear stability analysis.

lower than in the -0.21 s^{-1} shear case due to the carrier wave having lower steepness. As the perturbation wavenumber is increased beyond the theoretical stability threshold, both current profiles exhibit stabilisation of sideband amplitudes, with zero or negative amplification beyond $\hat{K} \approx 1.4$.

The numerical solutions of the vor-NLSE closely match the experimental data for both current profiles. In the -0.21 s^{-1} shear case, although removing shear from theoretical predictions leads to over-prediction of sideband growth for all unstable cases, this does not become significant until the edge of the stability region ($\hat{K} = 1.42$) is reached. However, significant changes in sideband evolution are apparent in the -0.48 s^{-1} shear rate case where the NLSE consistently over-predicts the amplification of sideband amplitudes at all unstable perturbation wavenumbers. This maximum error occurs predominantly at lower perturbation wavenumbers ($0.59 \leq \hat{K} \leq 1.33$). At $\hat{K} = 0.59$, the over-prediction exceeds 100% of the measured value. Predictions from the vor-NLSE numerical scheme closely follow the sideband evolution trend well into the stable perturbation wavenumber region. In the -0.48 s^{-1} shear rate case, above $\hat{K} = 1.62$ the vor-NLSE predictions are still in good agreement with experimental measurements, however the vor-NLSE and NLSE results are almost indistinguishable.

The effect of discounting shear on wave height is illustrated by the linearised envelope time

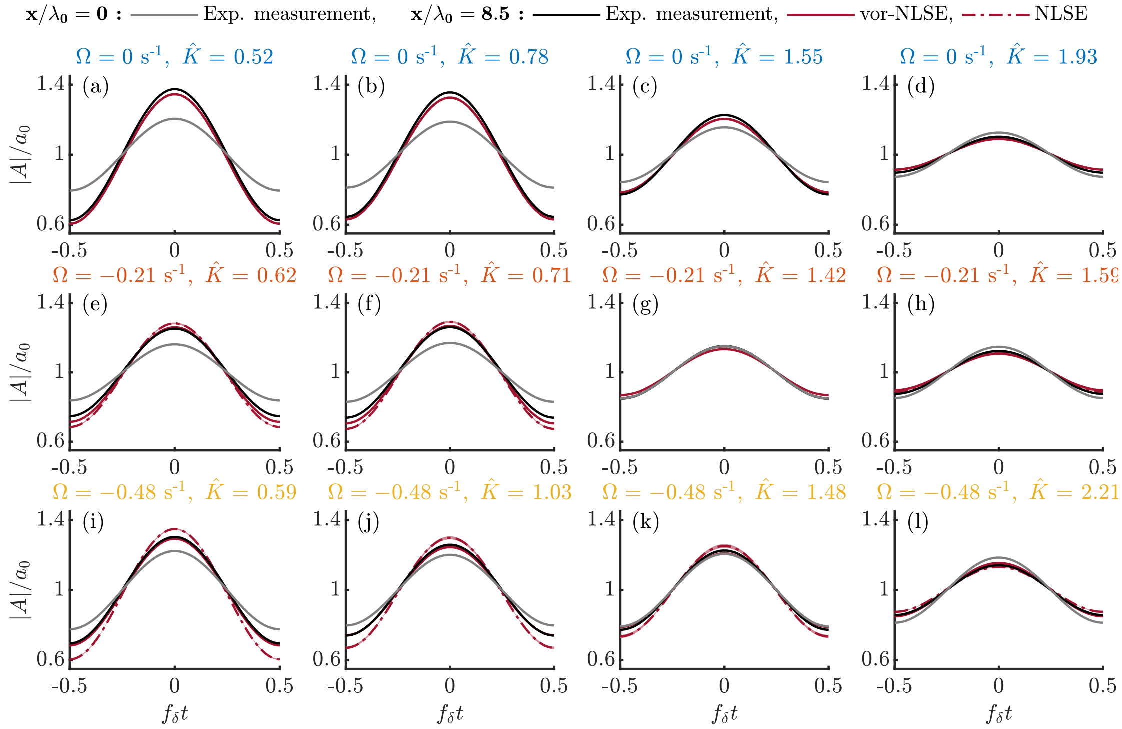

Figure 2.10: Envelopes of the linearised experimental incident wavetrains, A, at $x = 0$ m (grey line, used as wavemaker boundary condition to numerical solution) and $x = 8.9$ m (black line) normalised by the carrier component amplitude and compared with predictions by the vor-NLSE (continuous brown lines) and zero-shear NLSE (dot-dashed brown lines) as a fraction of its carrier amplitude (part II).

series data presented in figure 2.10 where the over-prediction of the envelope amplitude of 29% in panel (i) ($\hat{K} = 0.59$) by the NLSE is in stark contrast to the corresponding vor-NLSE result which follows the experimental measurement to an error within two standard deviations (seen as an overlap in vor-NLSE and experimental boundaries). The incorrect prediction in envelope amplitude by the NLSE in figure 2.10 occurs at all unstable perturbation wavenumbers of the -0.48 s^{-1} shear current case, displaying an over-prediction of 16% in the $\hat{K} = 1.03$ (panel (j)); again the vor-NLSE results compare favourably, with an under-prediction of only 7%.

Figure 2.11 shows this significant difference in predictions between the vor-NLSE and uniform velocity NLSE occurs in all of the unstable perturbation wavenumbers at the $\Omega = -0.48$ s^{-1} shear rates. As with the zero current cases, the majority of vor-NLSE amplification factor predictions fall within two standard deviations across repeats.

Across all perturbation wavenumbers, repeatability appears to be very good with minimal changes in sideband amplitude across repeats. However, in the -0.48 s^{-1} shear case, when perturbation wavenumber approaches the stability boundary, a larger standard deviation is seen. The perturbation wavenumbers at which larger deviations exist emphasises the sensitivity of the system to initial conditions. At the very sharp perturbation wavenumber stability boundary, this nonlinear system becomes very sensitive to initial conditions where slight changes in carrier

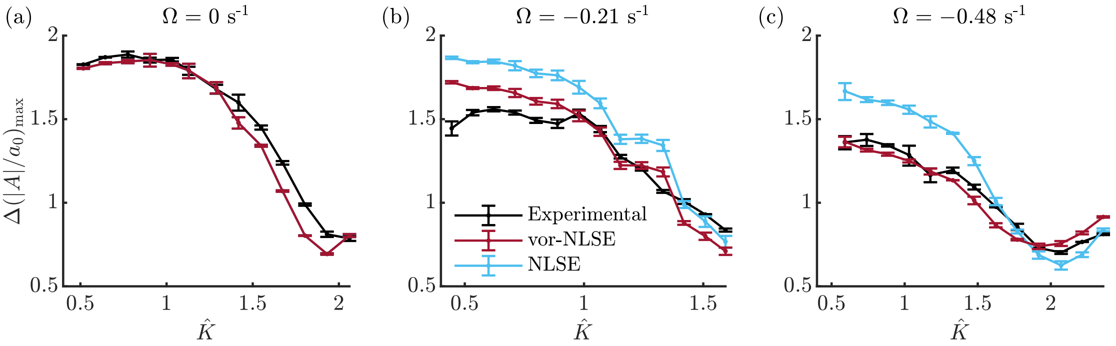

Figure 2.11: Maximum amplification factors, denoting the ratio between the maximum envelope amplitudes at the first and final gauges, as a function of the normalised sideband wavenumber parameter $\hat{K} = K/\left(a_0\sqrt{-M^*/L^*}\right)$ and for the three shear rates.

amplitude may push the system into a region of stability or instability (see Appendix D).

2.5 Conclusion

Measurements of physical experiments have been compared with the linear and weakly nonlinear constant vorticity, arbitrary depth, linear shear wave evolution equations derived by Thomas, Kharif, and Manna [123] (TKM12). It has been shown that in cases of shear $\Omega < -0.21$ s^{-1} (i.e. for shear rates sufficiently large in magnitude), the constant vorticity equations consistently perform significantly better than the standard, uniform-current equations. The linear vor-dispersion equation gave results that remained within experimental error (part I). Sideband evolution predictions of the vor-NLSE consistently remained within two standard deviations across experiment repeats (part II).

In part I, the wavelengths and frequencies of low-steepness, regular waves were measured for five opposing current profiles (down to $\Omega = -0.87$ s^{-1}), and measured dispersion relations obtained. The experimental measurements were compared with predictions from arbitrary depth, constant vorticity and standard, uniform-current dispersion relations. For all current profiles, results from the constant vorticity dispersion relation agreed with physical measurements, where the experimental data points fell within 95% confidence bounds associated with the estimation of current shear and surface current. For $\Omega \leq -0.48$ s^{-1}, the predictions by the uniform-current dispersion relation deviated significantly from both the vor-dispersion equation and experimental measurements.

In part II, in nonlinear experiments, the sidebands of modulated wavetrains were observed to grow, creating large amplitude wave pulses and indicating modulational instability in all current profiles within the unstable perturbation wavenumber region (as predicted by linear stability analysis of the vor-NLSE). Experimental measurements of sideband amplitude were compared with numerical predictions of space-marching solvers of the vor-NLSE and the standard uniform-current NLSE. The vor-NLSE results provided a very good match to experimental measurements over the range of current profiles considered, unlike the uniform velocity NLSE whose sideband amplification predictions were consistently 10% to 30% higher than measured.

Future work should include an investigation into the destabilizing effects of positive shear.

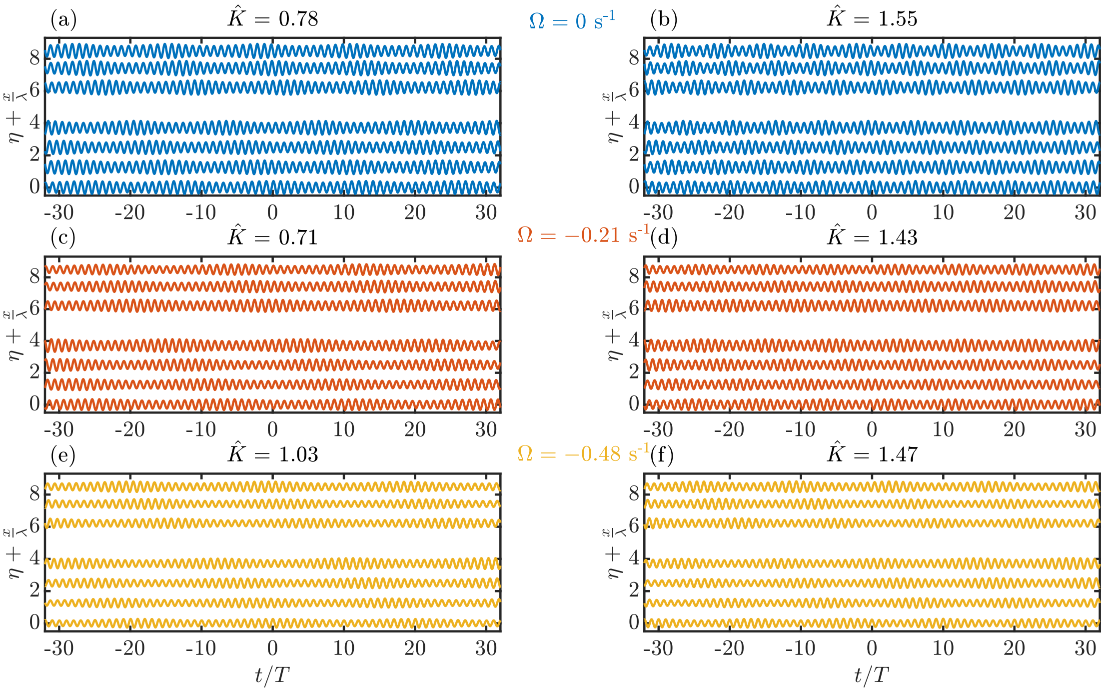

Figure 2.12: Evolution of experimental incident free surface elevation for nominally unstable (left) and marginally unstable (right) sideband frequencies (part II) for the three shear rates. A scaled free surface elevation, 25η is presented to make plots clear.

This likely requires the use of a high-velocity wave-following surface current which is known to reduce amplitudes and thus their associated nonlinear effects. As such, wavemakers capable of high frequencies ($\omega_0 > 12\,\text{rad}\,\text{s}^{-1}$) and a long evolution distance would be required. Additionally, the propagation of breather-type NLSE solutions (having known and previously verified amplification factors on still water) on negatively sheared currents would likely quantify the effect of sheared current on amplification factor more precisely, although their experimental generation will most likely rely on an iterative experimental procedure. Additionally, following laboratory verification, a natural extension would investigate the vor-NLSE applicability to real-world environments such as the Columbia River estuary bordering Washington and Oregon in the United States of America. The Columbia river is known for its high current and shear rates [73] and has previously been the subject of shear and its effects on shipping [80].

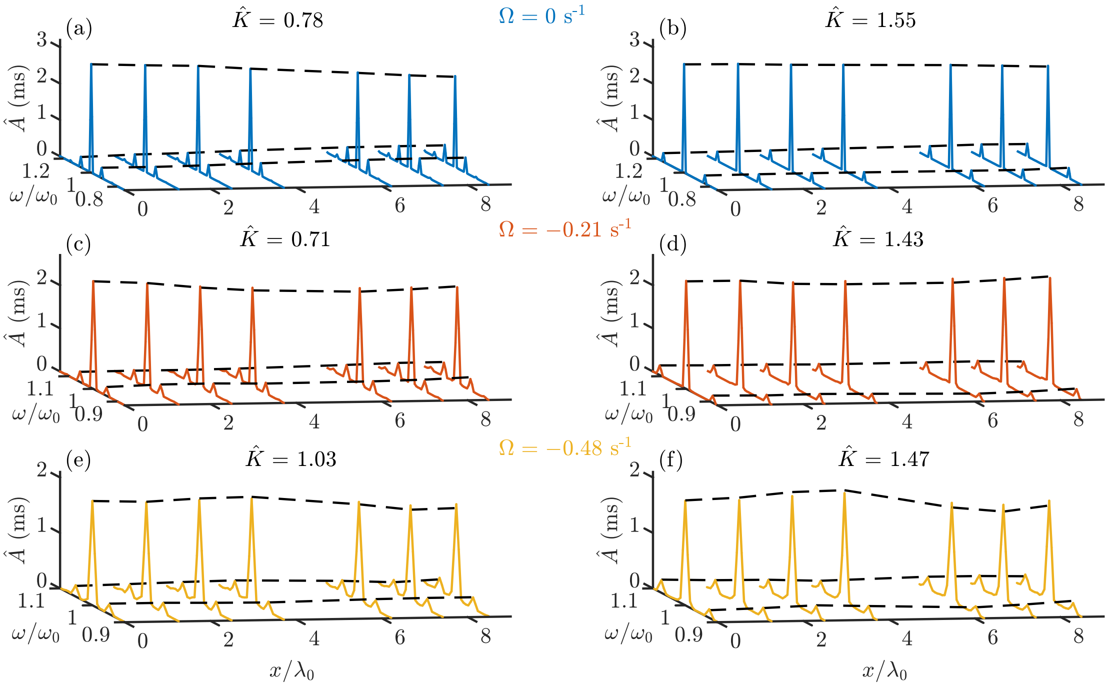

Figure 2.13: Evolution of experimental incident amplitude spectra for unstable (left) and marginally unstable (right) sideband frequencies. Black dashed lines mark the carrier and primary sideband amplitudes through their spatial evolution (part II).

Chapter 3

Modulational Stability in Crossing Seas*

3.1 Introduction

Crossing seas, in which waves travel in multiple directions, have been identified as an important challenge to offshore operations, linked to an increased probability of extreme waves [16, 20]. In addition to specific environmental forcing such as wind or (sudden) changes in bathymetry, two important mechanisms play a role in the formation of so-called rogue waves in the ocean, namely random dispersive focusing enhanced by weak bound-wave nonlinearity and modulational instability [71, 44, 98, 5]. Herein, a contribution to the understanding of extreme waves in crossing seas is made by reporting on an experimental study of modulational instability in waves crossing at angles between $0° \leq \theta \leq 88°$.

For long-crested or unidirectional seas, it is well established that weakly nonlinear regular wavetrains in sufficiently deep water rapidly evolve into pulses of wave groups through modulational instability [136, 14]. Extreme waves can form within such groups, making modulational instability a topic of considerable interest in the context of rogue wave events. The nonlinear Schrödinger equation (NLSE) provides the simplest mathematical framework for studying modulational instability, and permits unstable solutions including breathers and plane Stokes waves [84, 103]. Breather waves are characterized by a sudden increase in amplitude of initially regular waves to either three or five times their initial value [6, 24], and provide close approximations to rogue waves in long-crested seas. However, experimentally, breather waves are particularly sensitive to initial conditions, which must be specified precisely for the waves to attain maximum amplitude [25]. Particularly, in the case of the Peregrine breather, which is localized in both time and space, precise initial conditions lead to an extreme wave only once during its evolution. Although precise reproduction of specific breather solutions in the laboratory requires special input conditions at the wavemaker, such initial conditions do not exist in the ocean. Nevertheless, clear evidence of breather trains has been observed in measured ocean wave data sets through the nonlinear Fourier method [100]. Moreover, in the laboratory, breather trains have been observed to be stable to disturbances such as from wind [23].

The unstable regular Stokes wave seeded with sideband components to the carrier has pe-

---

[*] An abridged version of this chapter has been published in a paper entitled—"Experimental Observation of Modulational Instability in Crossing Surface Gravity Wavetrains", co-authored by M. L. McAllister, A. G. L. Borthwick, and T. S. van den Bremer, *MDPI Fluids,* 4(2):103, [116]

riodic modulations that grow, facilitating straightforward measurement of wavetrain stability, such as in the seminal paper by Lake et al. [79]. In this idealized problem, energy is returned from the sidebands to the carrier wave at later times, leading to periodic modulation and demodulation on very long time scales known as Fermi–Pasta–Ulam (FPU) recurrence [52, 53, 69]. Strictly, FPU recurrence only exists in conservative systems and is prevented by the occurrence of breaking. In the case of breaking, the principle of time-reversibility also does not apply [21]. However, even in the presence of breaking waves, energy from sidebands returns to a central carrier wave after some time, giving rise to FPU-type modulation-demodulation cycles [79, 90]. This chapter avoids these complications in all experiments by considering only the initial stages of modulational instability, before breaking takes place.

Although extensively studied both theoretically and experimentally in one dimension, the applicability of the 1D+1 NLSE to the open ocean is limited by the equation's unidirectionality. In the open ocean, waves may be created from multiple sources, interact, and cross at an angle. Additionally, in fetch-limited seas it has been observed that spectral components above and below the peak frequency become bimodal with energy naturally spreading symmetrically to angles above and below that of the peak frequency direction [135, 50]. As derived for deep-water by Onorato et al. [95] from the 2D+1 Zakharov equation [137], the coupled nonlinear Schrödinger equation (CNLSE) is a system of nonlinear wave equations describing the interaction of two narrow-banded weakly nonlinear wave systems propagating at an angle (see also [59]). This deep-water CNLSE has since been extended to finite depth by Kundu et al. [77]. However, for practical purposes, the experiments presented herein were performed in deep water. The CNLSE enables both modulational instability and crossing effects to be explored simultaneously. By invoking the assumptions of symmetrical propagation about the x-axis at angle $\pm\theta$ and shared group velocity along the x-axis, the CNLSE simplifies and readily lends itself to linear stability analysis. The results define both low angle and high angle instability regions separated at $\theta = 35.26°$ and $\theta = 144.74°$ (see also [107]). Discussions concerning linear stability of CNLSE and the effect of the changing values of CNLSE coefficients with crossing angle have highlighted increased amplification factors but decreased growth rates of breather and soliton solutions in crossing seas for angles approaching 35.26° [96, 2]. Within this chapter, crossing angle, θ is the angle at which waves propagate to the x-axis, i.e., when two waves cross at $\pm\theta$ the angle of bisection is 2θ. Along with the general investigation into plane wave stability, rogue wave solutions to the CNLSE are known to exist and have been classified and, through numerical computations, compared to their 1D+1 analogue, the Peregrine breather [39].

Laboratory experiments by Toffoli et al. [125] have measured the long-term statistical behaviour of deep-water weakly nonlinear crossing waves up to crossing angles of 20° (see Figure 3.1b for these experimental angles). Numerical solutions using a higher-order spectral method were used to confirm these findings and additionally, to study crossing angles up to 90° and found increases in kurtosis for crossing angles in the range $20° < \theta < 30°$ [126]. Additionally, the effect of oblique sideband perturbations (of up to 37°) to plane waves propagating over finite depth were investigated experimentally and sideband growth was reported [126]. The existence of short-crested crossing breather waves (slanted breather solutions to the 2D+1 NLSE) has also been confirmed experimentally [27].

In addition to possible modulational instability, changes to the second-order bound waves occur when waves cross. The wave-averaged free surface, represented spectrally by second-order difference waves, is the local mean surface elevation formed by temporal averaging over the rapidly varying waves that make up the slowly varying group. Whereas a set-down of the wave-averaged free surface is expected in the absence of crossing, packets are accompanied by a set-up for sufficiently large crossing angles. This can be theoretically predicted [93, 65, 128, 29] based on second-order interaction kernels [61, 110, 37, 54]. Set-up has been observed in field data

[131, 127, 109] and recently in detailed laboratory experiments [87]. For the Draupner wave, recorded in the North Sea on the 1st of January 1995 [62], the observation of set-up can be seen as evidence for crossing [131, 4, 89]. In fact, linear dispersive focusing enhanced by bound-wave nonlinearity but without modulational instability may be sufficient to explain observations such as the Draupner wave [51, 17].

Recently, a number of additional numerical studies have examined extreme waves and modulational instability in crossing seas. Støle-Hentschel et al. [118] have shown, using numerical simulations and laboratory experiments, that a small amount of energy travelling in exactly the opposing direction can significantly reduce the kurtosis of the surface elevation. Gramstad et al. [57], using random simulations of the Zakharov equation, found that, for unimodal spectra, kurtosis increased at crossing angles close to 50° and at very small crossing angles when compared to the unidirectional case. Kurtosis was found to be at a minimum at 90°.

In this chapter, regular wave experiments with seeded sidebands for two crossing wavetrains in a circular wave basin are reported on. These experiments are the crossing-wave counterpart of the classical experiments by Lake et al. [79] and cover both stable and unstable regions of the (K, θ) space, through the range $0^\circ \leq \theta \leq 88^\circ$, where K is the perturbation wavenumber. The growth of sideband amplitude is measured and compared to results from linear stability analysis of the CNLSE, as well as numerical solutions of this equation.

This chapter is laid out as follows. First, Section 3.2 reviews the theoretical background, followed by an exposition of the experimental methodology in Section 3.3. Experimental results are presented and compared to solutions of the CNLSE in Section 3.4. Finally, conclusions are drawn in Section 3.5.

3.2 Theoretical background

3.2.1 Coupled nonlinear Schrödinger equation (CNLSE)

The coupled nonlinear Schrödinger equation (CNLSE), derived by [95] from the 2D+1 Zakharov equation [137], is a narrow-banded wave equation describing the evolution of coupled, complex wave envelopes A and B. Both wave envelopes propagate on an associated carrier wave whose properties define the CNLSE coefficients and thus (along with the initial conditions) the envelope evolution. Scaled for water waves, and under the assumption of identical but symmetrical carrier waves (about the x-axis) with distinct amplitude envelopes, the CNLSE is given, in a Cartesian coordinate system (x, y, t), by [95],

$$\frac{\partial A}{\partial t} + C_x \frac{\partial A}{\partial x} + C_y \frac{\partial A}{\partial y} - i\alpha \frac{\partial^2 A}{\partial x^2} - i\beta \frac{\partial^2 A}{\partial y^2} + i\gamma \frac{\partial^2 A}{\partial x \partial y} + i(\xi|A|^2 + 2\zeta|B|^2)A = 0, \tag{3.1}$$

$$\frac{\partial B}{\partial t} + C_x \frac{\partial B}{\partial x} - C_y \frac{\partial B}{\partial y} - i\alpha \frac{\partial^2 B}{\partial x^2} - i\beta \frac{\partial^2 B}{\partial y^2} - \gamma \frac{\partial^2 B}{\partial x \partial y} + i(\xi|B|^2 + 2\zeta|A|^2)B = 0, \tag{3.2}$$

where carrier properties: frequency, ω_0; x-axis wavenumber, k; y-axis wavenumber, l; and absolute wavenumber, $k_0 = \sqrt{k^2 + l^2}$, define the group velocities C_x and C_y along their respective axes,

$$C_x = \frac{\omega_0}{2k_0^2} k \quad \text{and} \quad C_y = \frac{\omega_0}{2k_0^2} l, \tag{3.3}$$

the linear coefficients α, β, and γ are given by,

$$\alpha = \frac{\omega_0}{8k_0^4}(2l^2 - k^2), \quad \beta = \frac{\omega_0}{8k_0^4}(2k^2 - l^2), \quad \text{and} \quad \gamma = -\frac{3\omega_0}{4k_0^4} lk, \tag{3.4}$$

and the nonlinear coefficients ξ and ζ by,

$$\xi = \frac{\omega_0}{2k_0}\frac{k^5 - k^3l^2 - 3kl^4 - 2k^4k_0 + 2k^2l^2k_0 + 2l^4k_0}{(k-2k_0)k_0} \quad \text{and} \quad \zeta = \frac{2\xi}{\omega_0 k_0^2}. \tag{3.5}$$

The carrier frequency ω_0 and absolute wavenumber k_0 are related through the deep-water dispersion relation, $\omega_0 = \sqrt{k_0 g}$, with g denoting the gravitational constant.

In the special case of envelopes propagating along the x-axis, a Galilean transformation into the group reference frame reduces the CNLSE to [95],

$$\frac{\partial A}{\partial t} - i\alpha\frac{\partial^2 A}{\partial X^2} + i(\xi|A|^2 + 2\zeta|B|^2)A = 0, \tag{3.6}$$

$$\frac{\partial B}{\partial t} - i\alpha\frac{\partial^2 B}{\partial X^2} + i(\xi|B|^2 + 2\zeta|A|^2)B = 0, \tag{3.7}$$

where $X = x - C_x t$. From the wave packet amplitudes, the (linear) free surface elevation is reconstructed by reintroducing the carrier waves through,

$$\eta = \mathrm{Re}\left[Ae^{i(kx+ly-\omega_0 t)} + Be^{i(kx-ly-\omega_0 t)}\right]. \tag{3.8}$$

The associated amplitude spectrum (given as input to the wavemakers) is shown in figure 3.4.

3.2.2 Linear stability analysis

Linear stability analysis of the CNLSE reveals many properties of the equation and, using a seeded carrier solution, allows prediction of the initial sideband growth rate. Identical plane waves are admitted as solutions to (3.6) and (3.7) and perturbations of infinitesimal amplitude and phase are added to obtain (see also [95]),

$$A = a_0(1+\delta_a)e^{-i(\omega_0 t + \delta\phi_a)} \quad \text{and} \quad B = b_0(1+\delta_b)e^{-i(\omega_0 t + \delta\phi_b)}, \tag{3.9}$$

where a_0 and b_0 are carrier amplitudes, and δ_a, δ_b, $\delta\phi_a$, and $\delta\phi_b$ are small perturbations in amplitude and phase. In this linear stability analysis, the assumed form of the sideband solutions a_δ and b_δ is,

$$a_\delta = a_{\delta,0}e^{i(\Omega t \pm Kx)} \equiv a_0\delta_a \quad \text{and} \quad b_\delta = b_{\delta,0}e^{i(\Omega t \pm Kx)} \equiv b_0\delta_b, \tag{3.10}$$

where $a_{\delta,0}$ and $b_{\delta,0}$ are the initial sideband amplitudes, K is the perturbation wavenumber, and Ω is the perturbation frequency. The relationship between K and Ω is found through linear stability analysis as [95],

$$\Omega = \pm\sqrt{\alpha K^2[(\xi(a_0^2 + b_0^2 + \alpha K^2) \pm \sqrt{\xi^2(a_0^2 - b_0^2)^2 + 16\zeta^2 a_0^2 b_0^2}]}, \tag{3.11}$$

where it is apparent that Ω may take either real or imaginary values. Following substitution of this relationship into (3.10), either oscillatory (when $\Omega \in \mathrm{Re}$) or exponential (when $\Omega \in \mathrm{Im}$) behaviour can be expected from the sidebands.

Figure 3.1 presents the instability regions in (K, θ)-space with stability boundaries denoted by the critical perturbation wavenumber function, $K_c(\theta)$. Three regions of instability exist: at low angle, $0° < \theta < 35°$; medium angle, $46° < \theta < 143°$; and high angle, $145° < \theta < 180°$, in which θ is related to the carrier wavenumbers through $\theta = \arctan(l/k)$. It should be noted that the asymmetry around 90° (i.e., comparing the region from 0° towards an increasing angle θ

and the region from 180° towards decreasing θ) arises because the perturbation always travels in the positive x-direction. Figure 3.1a also shows where in (K, θ) space the experiments reported on herein lie, with Figure 3.1b displaying the locations of experiments previously reported by Toffoli et al. [125]. These experiments were restricted to angles $0° < \theta < 20°$ and were carried out with a continuous spectrum instead of discrete sidebands, as illustrated by the horizontal lines in Figure 3.1b, with 85% of their energy bounded by the y-axis and the black crosses.

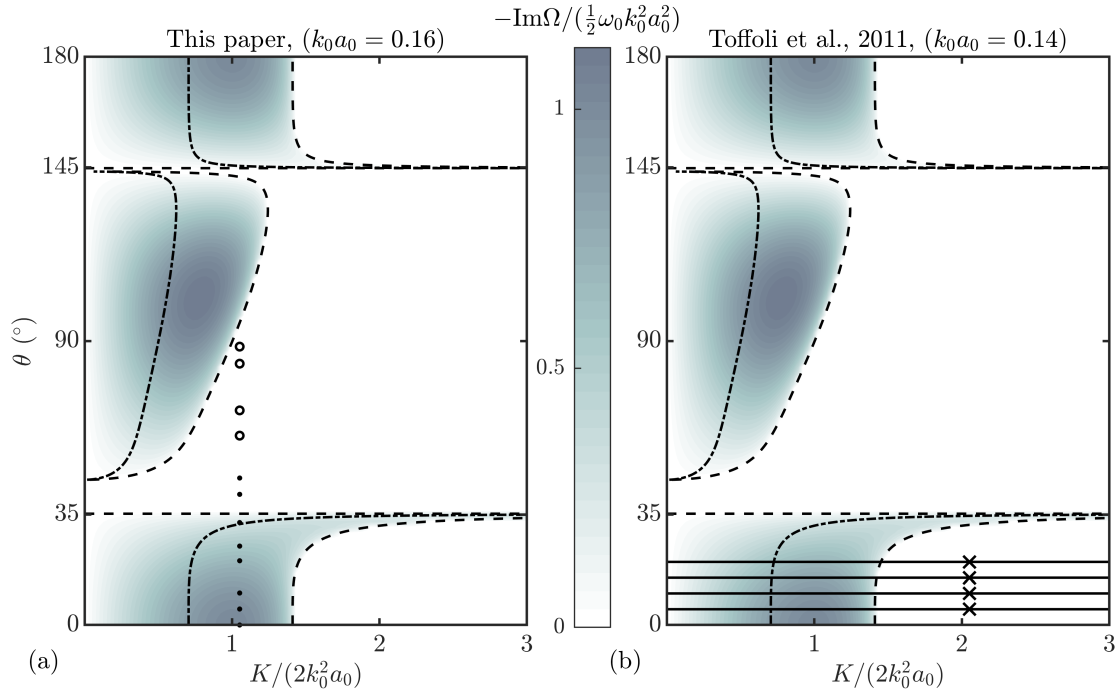

Figure 3.1: Surfaces showing the growth rate obtained from linear stability analysis of the coupled nonlinear Schrödinger equation (from (3.11)). Panel (**a**) presents experimental parameters where experiments 2a-h are indicated by dots (results presented in main text) and experiments 2i-l by open circles (results presented in Appendix E). The crossing angles of experiments performed by Toffoli et al. The continuous spectrum used in the experiments of [125] are shown as solid lines in panel (**b**) with the crosses and y-axis marking the boundary containing 85% of the spectral energy (note that the crossing angle, β, in Toffoli et al. [125] is equivalent to 2θ). The dashed lines indicate boundaries of stability regions, while the dot-dashed lines show the boundary between complex $(0 < K \leq K_c/2)$ and simple $(K_c/2 < K < K_c)$ evolution.

For unidirectional waves, modulational instability behaves as described by the standard NLSE but with increased instability due to the presence of two carrier waves, with a consequent doubling of steepness. As the crossing angle is progressively increased, the region of instability extends further along the wavenumber axis, whereas the magnitude of the instability decreases gradually. At $\theta \approx 35.26°$ (exactly, $\theta = \arctan(1/\sqrt{2})$), the low angle instability region ends, having encompassed all wavenumbers. At approximately 46°, the medium-angle instability region begins to take shape, starting close to zero wavenumber and expanding along the wavenumber axis until the crossing angle reaches approximately 143°. Finally, the high-angle region commences as a sharp boundary at approximately 145° and ends as a mirrored version, similar to the low-angle region (with both waves travelling at 180° from the x-axis).

3.2.3 Characteristics of modulational instability: complex vs. simple evolution

Figure 3.2 presents the spectral and temporal evolution of two modulated wavetrains with different perturbation wavenumbers propagating from the initial conditions (3.9) with $\theta = 20°$ and $a_{\delta,0} = 0.1a_0$, obtained using a numerical solver of the CNLSEs (see Appendix F). The effect of modulational instability is instantly recognizable from the increase in amplitude of the sidebands closest to the carrier wave (primary sidebands). As the primary sideband amplitudes increase, the carrier amplitude begins to decrease. Further in the evolution process, secondary sidebands appear at integer multiples of the primary sideband wavenumber. The effect of this initial stage of instability is seen in the packet amplitude in Figure 3.2b as a rapid increase in the group amplitude. Following the exponential sideband amplitude growth, Fermi–Pasta–Ulam recurrence is observed. During idealized FPU recurrence, energy is exchanged periodically between modes, and the system returns to its original state [52, 53, 69]. However, in water waves, energy may be lost to wave breaking resulting in a nonconservative system but FPU recurrence is a long-term behaviour, and strong modulational instability is required to observe it in the space available in most experimental facilities.

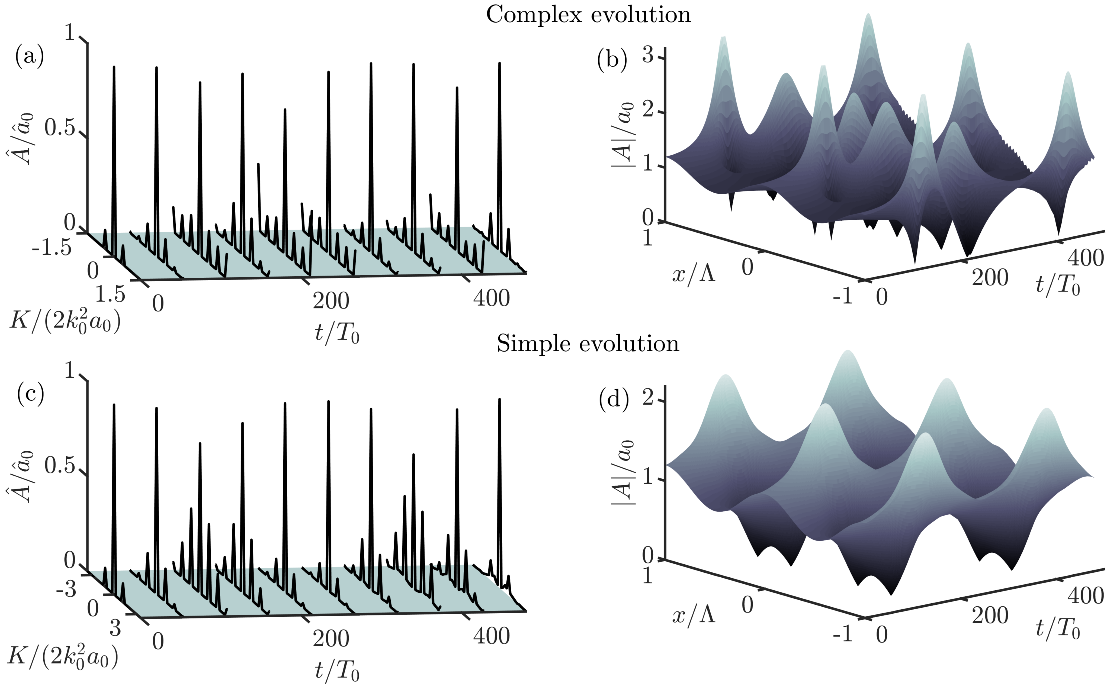

Figure 3.2: Spectral and temporal evolution obtained from the time-marching of the CNLSE for two unstable modulated wavetrains crossing at $\theta = 20°$. Panels (**a**) and (**b**) show complex ($0 < K \leq K_c/2$) evolution, whilst panels (**c**) and (**d**) display simple ($K_c/2 < K < K_c$) evolution. Temporal axes have been normalized by the carrier wave period, T_0.

Figure 3.2a,b show the wavetrain propagating with complex recurrence, whereas Figure 3.2c,d show simple recurrence. Complex recurrence is expected when K lies less than (or at) half-way through the instability region ($0 < K \leq K_c/2$), and primary sidebands themselves act as unstable carriers, continually spawning new sidebands. When K lies more than half way to the stability boundary ($K_c/2 < K < K_c$) new sidebands will lie in the stable region, and simple recurrence is observed.

3.3 Experimental methodology

3.3.1 Facility

The aim of experiments was to measure sideband growth at extreme crossing angles up to 90°. In order to achieve this, physical tests were performed in the FloWave Ocean Energy Research Facility at the University of Edinburgh, which is capable of omnidirectional wave creation and absorption. The basin (depicted in Figure 3.3a,b) has a diameter of 25 m, a working depth of 2 m, and is encircled by 168 actively absorbing force-feedback wavemakers. A Cartesian coordinate system was defined with its origin at the centre of the basin. The primary direction of propagation of the waves was in the positive x direction. In crossing wave experiments, the carrier waves travelled at an angle, θ, from the x-axis, as defined in Figure 3.3a. Wave generation in the facility was controlled using software based on linear wave theory. Ten resistance type wave gauges at a spacing of 1.5 m were mounted on a gantry spanning the basin x-axis (see Figure 3.3b for coordinates). Wave gauges were calibrated each day before tests commenced. A 20 min settling period was imposed between each test, allowing residual basin motion to settle to an acceptable level.

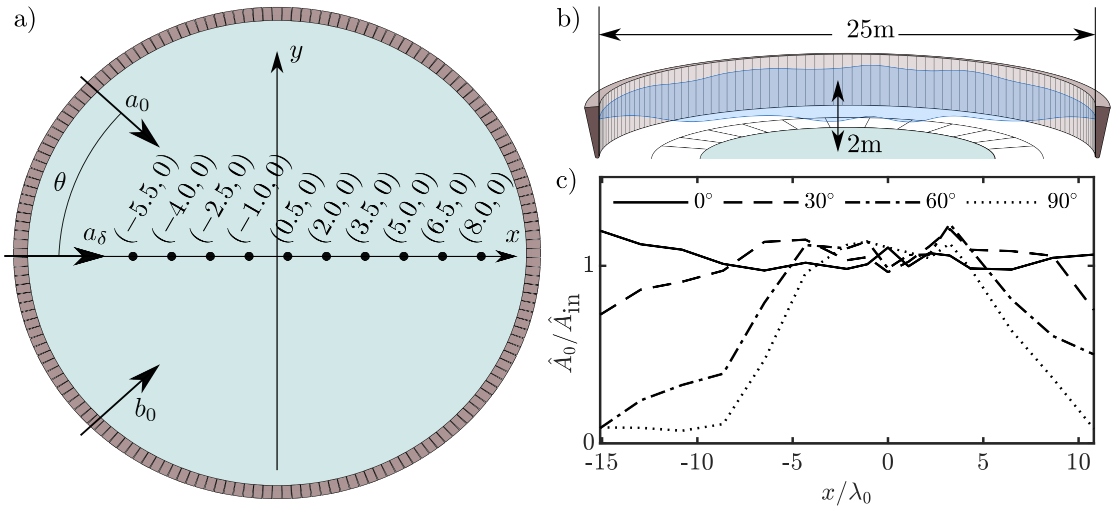

Figure 3.3: (**a**) FloWave Ocean Energy Research Facility at The University of Edinburgh, showing wave gauge locations relative to the centre of the basin $(0, 0)$ (units in m) and direction of wave system components (figure adapted from [92]). (**b**) Sectional view of the FloWave basin with key dimensions. (**c**) Amplitude profiles of unseeded carrier waves ($f_0 = 1.5$ Hz) travelling at an angle, θ, and measured along the basin x-axis (Part I). Amplitude profiles have been normalised by the target amplitude.

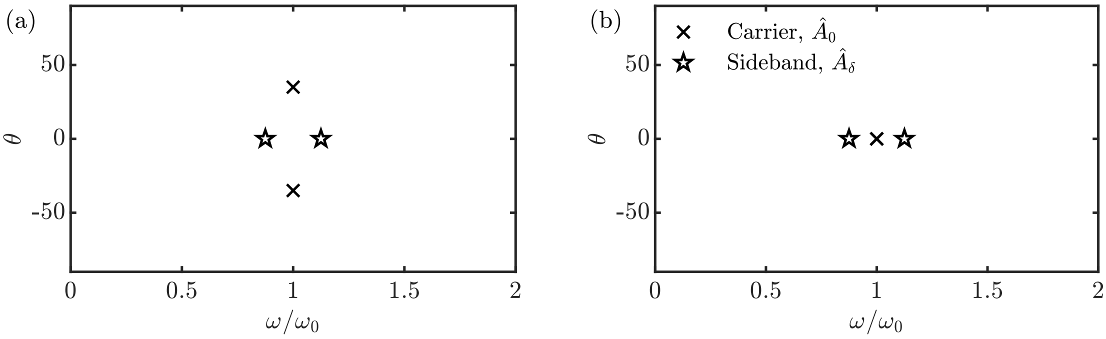

Figure 3.4: Examples of the input spectra given to the wavemaker software for all experiments in Chapter 3. **a**: Example input spectrum for modulated wave systems crossing at the critical angle. **b**: Example input spectrum for a modulated unidirectional wave system.

3.3.2 Matrix of experiments

The experimental campaign was split into two parts. Part I aimed to measure the length of crests in the facility. A manifestation of a finite number of wavemakers encircling a finite-size circular basin is the inability to create perfectly long-crested waves spanning the entire basin diameter. The drop in amplitude at the basin fringes (as shown in figure 3.3c) is dubbed the "finite-crest effect". This finite-crest effect needed to be quantified in order to estimate the length over which components travelling with different directions would interact. Part II aimed to measure the growth of frequency sidebands about carrier waves travelling at crossing angles $\pm\theta$. Crossing carrier and sideband waves only interact fully in regions of total crest overlap, and so the extent that these regions cover the chosen wave gauge locations is defined by the carrier crest length and angle. Experiments 1a–d (Part I) were therefore designed to determine the effective sideband evolution region in the basin at each angle. In these experiments, a single unseeded carrier wave was propagated at the angles given in Table 3.1 (Part I).

Table 3.1: Experiment labels and their corresponding crossing angles for both Part I (single, unseeded regular wave) and Part II (seeded waves). All experiments used carrier parameters of $f_0 = 1.5$ Hz, $k_0 a_0 = 0.16$, and $k_0 d = 18$. Experiments 2a–l used sideband parameters of $K = 3.02$ m^{-1}, and $a_{\delta,0} = 0.003$ m.

	Part I				**Part II**											
Expt.	**1a**	**1b**	**1c**	**1d**	**2a**	**2b**	**2c**	**2d**	**2e**	**2f**	**2g**	**2h**	**2i**	**2j**	**2k**	**2l**
θ (°)	0	30	60	90	0	5	10	20	25	32	41	47	60	68	83	88

For Part I, the amplitude profiles of experiments 1a–d are presented in Figure 3.3c and allow estimation of the carrier crest length in the FloWave facility. Experiment 1d ($\theta = 90°$) shows that, for high angle experiments, a reasonable region in which to expect full sideband-carrier interactions occupies approximately 10 wavelengths centred about the basin origin. However, the effective length is extended significantly to more than 20 wavelengths for crossing angles up to 30°, the region of greatest interest in Part II. As expected, for waves in the x-direction ($\theta = 0°$), the region covers all wave gauge locations. The results from the Part I tests were interpolated in order to estimate the finite-crest effect at all crossing angles.

All experiments in Part II were performed with constant values of carrier frequency, $f_0 = 1.5$ Hz, carrier amplitudes $a_0 = b_0 = 0.018$ m, and initial sideband amplitude $a_{\delta,0} = 0.003$ m, giving a depth parameter $k_0 d = 18$, and steepness of a single carrier, $k_0 a_0 = 0.16$. Figure 3.1a shows the expected growth rates, crossing angles, and sideband wavenumbers for the Part II tests. A simple system of four plane waves, consisting of two carrier waves propagating at $\pm\theta$ to the x-axis, and two sidebands propagating along the x-axis was used as input to the wave generation software. Explicitly, we thus have,

$$\eta(x_0, y, t) = \mathrm{Re}\left[a_0 e^{-i(\omega_0 t - y k_0 \sin\theta)} + b_0 e^{-i(\omega_0 t + y k_0 \sin\theta)} + a_{\delta,0}\left(e^{-i(\omega_0+\omega_\delta)t} + e^{-i(\omega_0-\omega_\delta)t}\right)\right], \tag{3.12}$$

where x_0 is the x-position of the wavemaker along $y = 0$ (the axis of propagation of the sidebands). The relatively high carrier frequency was chosen to slow group velocity, increasing the effective evolution distance. The carrier amplitude was subsequently calculated to give a moderate steepness of $k_0 a_0 = 0.16$, required for prominent instability but to avoid breaking. Each experiment was repeated 3 times.

3.3.3 Data processing

The calibrated wave gauge outputs (free surface time histories) from each experiment were bandpass filtered to eliminate higher-order and low-frequency bound waves. The recorded free surface elevation time series length was limited to eliminate reflected waves. A Tukey window with a tapering parameter of 0.2 was used to create a transient signal and limit the lobe effect associated with windowing. The length of the Tukey window was determined using the estimated linear group velocity of the wavetrain. The amplitude spectrum was determined at each location (see Figure 3.5), and the evolution of the primary sidebands (frequency components located closest to the carrier wave) used to identify modulational instability. The true frequency of these components was determined at the first gauge location. These component amplitudes were then tracked across all the remaining wave gauges. Sideband and carrier amplitudes at the first wave gauge location were used as initial conditions for a CNLSE solver (using the Fourier, split-step method, see Appendix F) and as inputs to the prediction by the linear stability analysis (3.11). The experimental evolution of the sidebands is compared to these numerical solutions, as well as the linear stability analysis (3.11) below.

3.4 Results

Figure 3.5 shows the evolution of the amplitude spectra along the tank's x-axis (the direction of propagation of the perturbation) for the different crossing angles considered in experiments in Part II. This figure shows both the finite-crest effect studied in Part I and the effect of modulational instability. Figure 3.6 presents the evolution of the primary sideband amplitudes of experiments 2a–l. The unseeded wave amplitudes presented in figure 3.3c (Part I) may be used to estimate the number of wavelengths over which the two systems fully interact.

Also shown in Figure 3.6 are the numerical results from the CNLSE time-marching scheme and the linear stability analysis. For brevity, only experiments 2a–h are presented (see Appendix E for experiments 2i–l, which show stability, as predicted). Each experimental repeat was solved across the spatial domain using the CNLSE solver. The results of the solver were then averaged and the standard deviation across repeats was calculated. Error bars for experimental measurements and dashed lines for the numerical scheme are used to indicate one standard deviation from the mean across repeats.

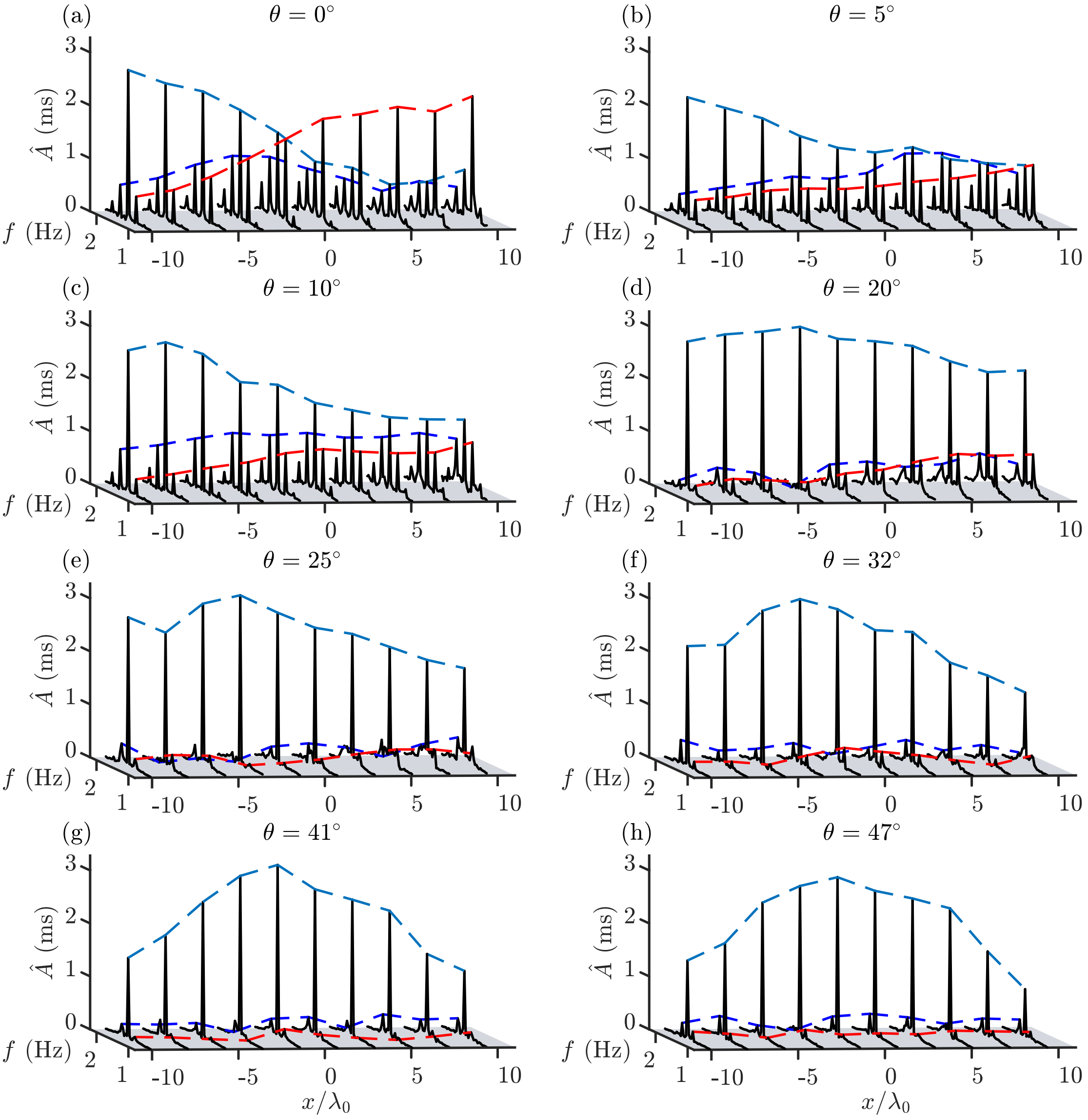

Figure 3.5: Amplitude spectra for experiments 2(**a**–**h**) (Part II) obtained using the measured free surface time series along the primary wave propagation direction (see Figure 3.3a for gauge locations) for different crossing angles, θ. Dashed lines follow the amplitudes of the carrier (light blue), lower sideband (red), and upper sideband (dark blue).

3.4.1 Unidirectional waves: $\theta = 0°$

The unidirectional experiment 2a, presented in Figure 3.6a, shows the most significant growth in sideband amplitude, with the lower sideband increasing by more than a factor of three. An increase in amplitude can also be observed in the upper sideband and the beginnings of FPU recurrence appear. The numerical solution in Figure 3.6a also shows significant growth and follows the average of the upper and lower sideband amplitudes well, displaying many of the same characteristics (such as FPU recurrence). However, the lower sideband grows much more quickly than the upper sideband, which is subject to initial growth followed by considerable attenuation, a feature not predicted by the NLSE but predicted in the modified NLSE [46] and commonly observed in unidirectional experiments [90].

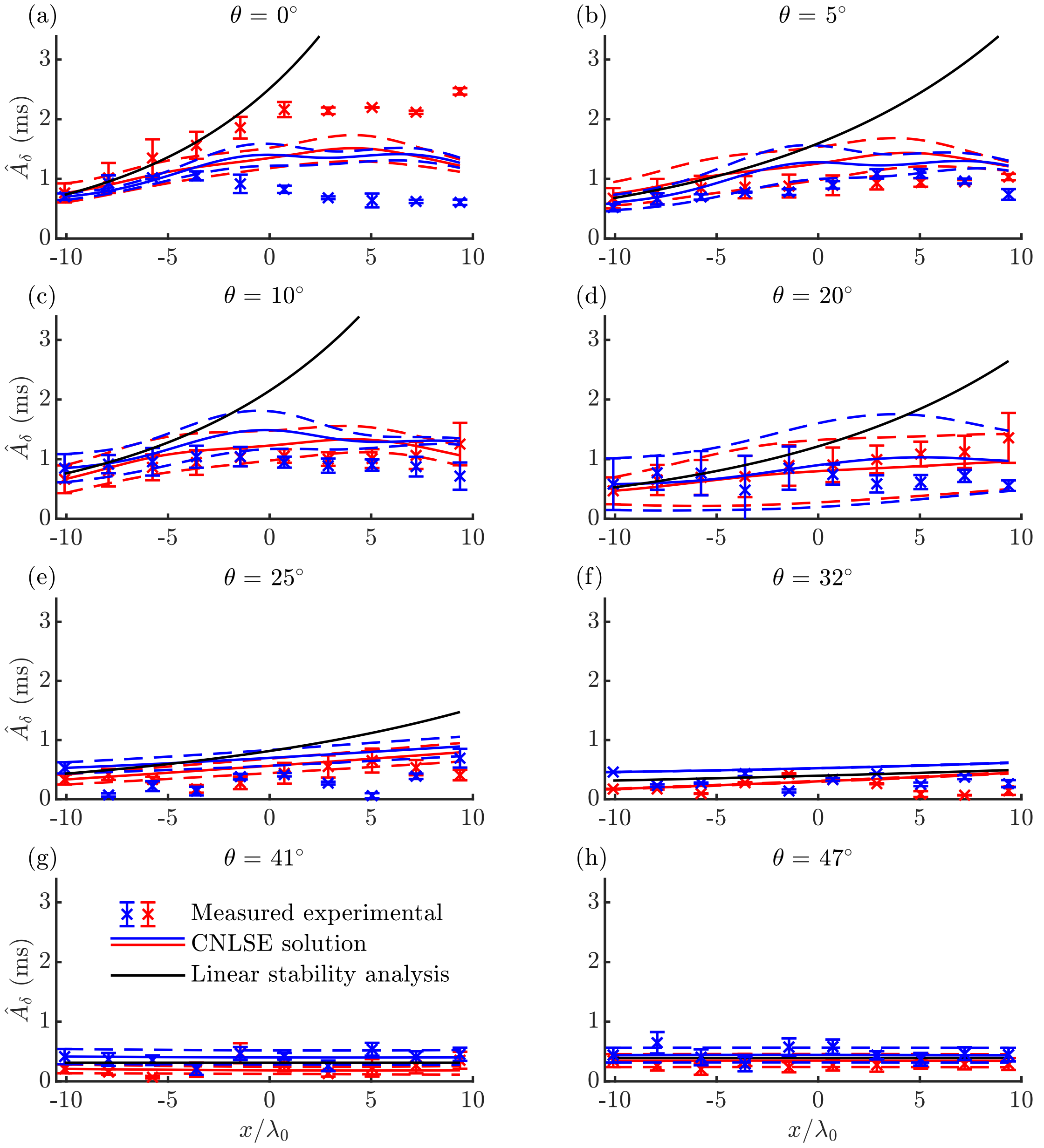

Figure 3.6: Sideband amplitude evolution along the basin centreline for experiments 2(**a**–**h**) (Part II) from measurements (crosses), numerical solutions of the CNLSE (thin blue and red lines) and linear stability analysis (thin black lines). Lower and upper sidebands are indicated in red and blue, respectively. Error bars and dashed lines represent one standard deviation from the mean across repeats for the measured data and the CNLSE solution, respectively.

The effect of sideband growth and modulational instability on free surface elevation is shown by the formation of pulses in Figure 3.7. Extreme waves occur in these pulses when carrier crests come in phase with the group centre, as demonstrated in Figure 3.7a at $x/\lambda_0 \approx 3$, where a cluster of three waves has more than doubled in amplitude within $13\lambda_0$. Figure 3.5a presents the amplitude spectra for experiment 2a. Substantial growth in secondary sidebands is evident. These secondary sideband frequency components, located at multiples of the perturbation frequency, contribute to the growth of wave group amplitudes and further enhance the strong decline of the carrier amplitude.

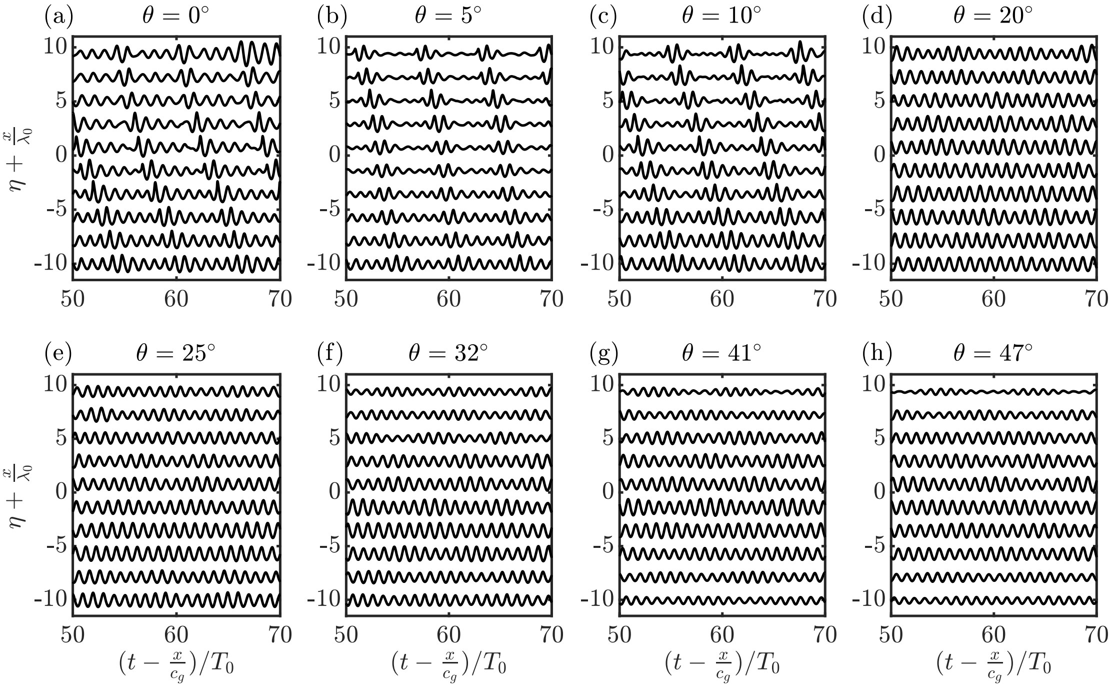

Figure 3.7: Measured free surface elevation time series for experiments 2(**a–h**) (Part II) shifted by the linear group velocity $c_g = \sqrt{C_x^2 + C_y^2}$ and normalized by the carrier period, T_0, with the positive vertical axis also representing increasing distance along the basin.

3.4.2 Crossing waves: $0° < \theta \leq 47°$

Figure 3.6b–d show that the growth observed in the unidirectional case continues but slows as the crossing angle is increased to 20°. In these experiments, the maximum amplification factor of the lower sideband generally reduces compared to the unidirectional case, whereas the upper sideband appears relatively unaffected, with no strong growth in either case. The pulse formations seen in experiment 2a persist in Figure 3.7b–d along with the sideband growth in Figure 3.5b–d, though with reduced magnitude. The unseeded carrier wave amplitude profiles of Figure 3.6b–d (measured in Part I) remain largely unchanged along the length of the basin, indicating that the effective length, over which crests reach their full amplitudes, is sufficiently long. Between $\theta = 25°$ and $\theta = 41°$ (Figure 3.6e–g), the transition to stability takes places. Throughout the transition to stability, the amplitude of unseeded regular waves show some drop in amplitude at their fringes. These drops in amplitude indicate the edges of the interaction region caused by the finite-crest effect of the tank. However, up to $\theta = 47°$, 15 wavelengths of interaction distance remain, a distance seen in the unidirectional case to be sufficient for sideband growth to occur. Experiments at angles of 41° and higher (Figure 3.6g,h, and Appendix E for the measurements from experiments 2i–l) are stable.

3.5 Conclusions

The effects of crossing angle on the modulational stability of two crossing nonlinear surface gravity wavetrains seeded with sideband perturbations has been experimentally investigated and measurements compared to numerical predictions by the the coupled nonlinear Schrödinger equation (CNLSE). The results demonstrate that sideband growth, as predicted by linear stability analysis of the CNLSE, can be reproduced in physical experiments undertaken in a circular wave basin. Strong modulation occurred in the unidirectional case, where the beginnings of recurrence were observed. The growth rate reduced as the crossing angle was increased; negligible growth was measured at and beyond a crossing angle of approximately 30°. Due to the reduced growth rate and the finite length of the basin, we have not been able to observe the increased growth rates associated with angles approaching the medium and high angle instability regions. An unseeded, regular wave was used to estimate the finite-crest effect (an experimental limitation for a finite-size circular basin), which started to become significant at 42°, well beyond the theoretical stability boundary of 35.26°. Taking into account the reduction in evolution length imposed by the finite-crest effect, no growth in sidebands was found to occur at these high angles. Future work should seek to extend experimental measurements into the second (high-angle) unstable region. To complete this successfully, the finite-crest effect must be considered allowing sidebands enough interaction evolution distance to grow.

Chapter 4

Nondispersive Crossing Waves*

4.1 Introduction

Stationary or nondispersive wave groups can occur in a range of nonlinear dispersive media, including in optics, Bose-Einstein condensates, plasma and hydrodynamics. The dynamics of higher-dimensional and steady wave packets is widely discussed in optics where the free-space scalar wave equation has traditionally been used to investigate linear, localised waves (LWs). Through various methods, a number of families of linear LW solutions have been found [19, 138, 139]. One such family is the so-called "X-wave" characterised by an X-shaped packet structure with a sharp, high amplitude centroid. Linear X-waves have been observed in optical fibres and confirmed to be truly nondispersive over finite distances, which is a common experimental limitation when investigating wave propagation features, in this particular case due to finite aperture radiators [83]. Optical localised waves have become useful in a number of relevant applications, including free space communications [134], optical lithography [68], and universal extreme events [114]. When the scales of group velocity dispersion (GVD) and nonlinear amplitude effects are comparable, linear wave equations become inaccurate and nonlinearity must be considered. Whereas GVD can be described using a dispersion relationship between frequency and wavenumber, amplitude-dependent nonlinear effects are modelled in a variety of ways, including through the universal nonlinear Schrödinger equation (NLSE) [1]. The NLSE is a nonlinear wave evolution equation that applies in nonlinear dispersive media [98, 41], and can be extended to two spatial dimensions to allow multi-dimensional, nonlinear LW group solutions. Indeed, in optics, "light bullet" nonlinear X-waves have been predicted and created experimentally and spontaneously through conical emission [31] and second-harmonic generation [40]. Extreme LW events or 'rogue waves' have also been detected in optical telecommunications fibre systems [11]. Due to the dispersive and nonlinear character of water waves, an analogy to optics, Bose-Einstein condensates and plasma can be naturally drawn [26, 94, 72, 47]. This also applies for directional weakly nonlinear shallow-water waves [12].

Both the coupled NLSE (CNLSE) (whereby two nonlinear wave systems interact) and the 2D+1 NLSE (whereby one wave system exists with a crossing angle θ between the carrier and envelope components) describe the evolution of crossing, weakly nonlinear wave systems, albeit in different ways. Using the 2D+1 NLSE, a critical crossing angle of $\theta_c = \pm \arctan 1/\sqrt{2}$ can be derived, beyond which linear focusing becomes defocusing, and the system achieves stability

---

[*] An abridged version of this chapter is forthcoming for publication in a paper entitled—"Hydrodynamic X Waves", co-authored by A. G. L. Borthwick, M. Onorato, A. Chabchoub, and T. S. van den Bremer, (Physical Review Letters)

to sideband perturbations [67]. In the CNLSE, a similar stabilization of the coupled system is observed at the same critical angle [95]. For hydrodynamics and at low interaction angles, numerical simulations of coupled wave systems have used the potential-flow Euler equations and experimentation to confirm these predictions of the CNLSE. An increase in the kurtosis of crossing seas up to approximately ±25° was observed, with this reducing rapidly as the angle was increased towards θ_c [125].

In hydrodynamics, wave groups propagating at the critical crossing angle predicted by the 2D+1 NLSE can be observed naturally at the fringes of the Kelvin ship wake [103]. Furthermore, it has been shown that an isolated spectral energy peak tends to spread outwards at this angle [82]. Additionally, this nonlinear energy transfer has been suggested as the cause of so called 'wing-waves', which exist at the fringes of extreme wave events. Their symmetry (at $\pm\theta_c$) may cause constructive interference enhancing already extreme events [3]. Extreme wave heights in crossing seas can also be enhanced by second-order bound waves causing wave-averaged set-up, as has been shown experimentally [88]. Through the elimination of dispersion at the critical crossing angle, it may be possible to extend dramatically the lifetime of groups containing extreme events in this particular configuration, playing a significant role in the probability of exceedance, coherence stability, as well as impact, of ocean rogue waves.

In this experimental study, a hydrodynamic X-wave is created in a directional and circular water-wave facility using the critical crossing angle. Using an array of wave probes to reconstruct the directional structure of the X-wave, spatio-temporal free surface elevation is measured and compared against a numerical solution of the 2D+1 NLSE. Comments are made on the effect of GVD, nonlinear focusing and spectral energy spread on the evolution of the X-wave. The crossing angle of a single arm of the X-shaped wave envelope was altered in order to quantify its effect on focusing. The experimental data includes waves of medium to high steepness allowing the characterisation of crossing angle effect on the amplitude-dependent wave nonlinearity (stability). Again, experiments are compared to numerical solutions of the 2D+1 NLSE.

4.2 Theoretical background

The following two-dimensional nonlinear Schrödinger equation (2D+1 NLSE) for deep-water surface gravity waves is considered [137],

$$i\left(\frac{\partial A}{\partial t}+c_g\frac{\partial A}{\partial x}\right)-\alpha\frac{\partial^2 A}{\partial x^2}+2\alpha\frac{\partial^2 A}{\partial y^2}-\beta|A|^2A=0, \tag{4.1}$$

where x and y are the horizontal coordinates, t is time, and $A(x,y,t)$ the envelope of a carrier wave of frequency ω_0 and wavenumber $\boldsymbol{k}_0=(k_0,0)$ propagating in the x-direction. The coefficients of the 2D-NLSE are given by

$$c_g=\frac{\partial\omega}{\partial k_x}\Big|_{\boldsymbol{k}=\boldsymbol{k}_0}=\frac{\omega_0}{2k_0},\ \alpha=\frac{1}{2}\frac{\partial^2\omega}{\partial k_x^2}\Big|_{\boldsymbol{k}=\boldsymbol{k}_0}=\frac{\omega_0}{8k_0^2},\ \beta=\frac{\omega_0k_0^2}{2}, \tag{4.2a,b,c}$$

where (4.2a-b) are obtained from the deep-water linear dispersion relationship $\omega^2=gk$ with $k=|\mathbf{k}|$. While the second derivative in the x-coordinate is responsible for the dispersion of the envelope, the second derivative in the y-coordinate implies diffraction. The free surface elevation, $\eta(x,y,t)$, can be recovered, to leading order, as follows:

$$\eta(x,y,t)=\frac{1}{2}\left(A(x,y,t)e^{i(k_0x-\omega_0t)}+\text{c.c.}\right). \tag{4.3}$$

To allow for wave packet propagation in space, the leading-order identity $\partial A/\partial t \simeq -c_g \partial A/\partial x$ can be used to transform the 2D+1 NLSE in a form that is a more suitable framework for the comparison with laboratory experiments [99, 22],

$$i\left(\frac{\partial A}{\partial x} + \frac{1}{c_g}\frac{\partial A}{\partial t}\right) - \frac{\alpha}{c_g^3}\frac{\partial^2 A}{\partial t^2} + \frac{2\alpha}{c_g}\frac{\partial^2 A}{\partial y^2} - \frac{\beta}{c_g}|A|^2 A = 0. \tag{4.4}$$

Solutions to the above equation are sought that correspond to envelopes traveling at an angle, θ, with respect to the carrier wave. Mathematically, this implies imposing a relation between the variable t and y,

$$T \equiv t\cos\theta + \frac{y}{c_g}\sin\theta. \tag{4.5}$$

After the above transformation, the complex envelope $A(x, y, t)$ becomes a function of only x and T, and the 2D+1 NLSE in (4.4) reduces to:

$$i\left(\frac{\partial A}{\partial x} + \frac{\cos\theta}{c_g}\frac{\partial A}{\partial T}\right) - \frac{\alpha}{c_g^3}(1 - 3\sin^2\theta)\frac{\partial^2 A}{\partial T^2} - \frac{\beta}{c_g}|A|^2 A = 0, \tag{4.6}$$

i.e., the integrable 1D+1 NLSE. From the (linear) dispersive coefficient,

$$\alpha' \equiv \frac{\alpha}{c_g^3}(1 - 3\sin^2\theta), \tag{4.7}$$

it can be seen that at $\theta = \pm\theta_c = \pm\text{atan}(1/\sqrt{2}) \approx \pm 35.26°$, the dispersive term becomes zero, then switches sign becoming defocusing [108, 82]. This is the critical crossing angle examined experimentally in this paper.

For small-amplitude waves, the nonlinear term in (4.6) can be neglected, and the dispersive linear Schrödinger equation with new coefficients remains,

$$i\left(\frac{\partial A}{\partial x} + \frac{1}{c'_g}\frac{\partial A}{\partial T}\right) - \alpha'\frac{\partial^2 A}{\partial T^2} = 0. \tag{4.8}$$

If $\theta = \pm\theta_c$, the system becomes nondispersive ($\alpha' = 0$). In the linear Schrödinger equation, the solution can be written as the superposition of two solutions, $A^+ = A(x, T; \theta_c^+)$ and $A^- = A(x, T; \theta_c^-)$ with $\theta_c^+ = +\theta_c$ and $\theta_c^- = -\theta_c$,

$$\begin{aligned} A(x, y, t) = {} & A_0 e^{-\left(t\cos\theta_c^+ + \frac{y}{c_g}\sin\theta_c^+ - \frac{x\cos\theta_c^+}{c_g}\right)^2/(2\sigma^2)} \\ & + A_0 e^{-\left(t\cos\theta_c^- + \frac{y}{c_g}\sin\theta_c^- - \frac{x\cos\theta_c^-}{c_g}\right)^2/(2\sigma^2)}, \end{aligned} \tag{4.9}$$

where A_0 is the theoretical linear focused amplitude of each arm and $\sigma^* \equiv \sigma/\cos(\theta_c)$ is the width of the group in the time domain. A Gaussian wave envelope was chosen. Equation (4.9) forms the characteristic X-shape pattern illustrated in figure 4.1. In the wavenumber spectrum of (4.9), all non-zero components are confined to the lines $k_y = \pm(k_x - k_0)\tan\theta_c$ (see appendix G for further details).

Given that the linear stability analysis of the uniform wave train solution to the 2D+1 NLSE

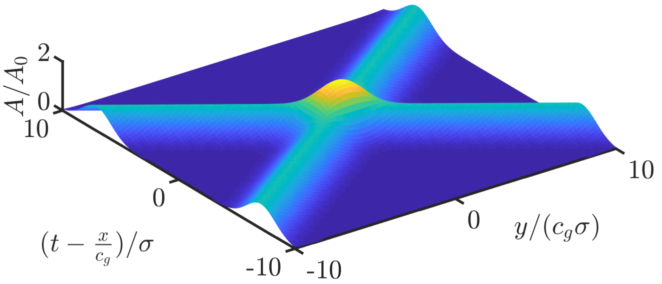

Figure 4.1: Theoretical X-wave envelope solution formed by two Gaussian envelopes, as parameterised in (4.9).

perturbed by $a_\delta = a_{\delta,0}\exp(i\Omega t \pm [ik_x(x-c_gt)+ik_yy])$ gives for Ω [136, 108]

$$\Omega^2 = \frac{\omega_0^2}{8k_0^2}\left(\frac{k_x^2}{8k_0^2} - \frac{k_y^2}{4k_0^2} - k_0^2A_0^2\right)\left(k_x^2 - 2k_y^2\right). \tag{4.10}$$

When Ω is imaginary and negative, the uniform wavetrain is unstable and grows (at rate $-i\Omega/c_g$ in space). As is readily evident from (4.10) and illustrated in figure 4.2, the critical angle also corresponds to the stability boundary. Single crossed-wave groups travelling at the critical angle can therefore be expected to travel without changing shape, as they are both unaffected by GVD and spectral sideband instabilities. However, due to energy transfer from their highly centralised energy peak, double-crossed wave groups may experience some non-stationary behaviour.

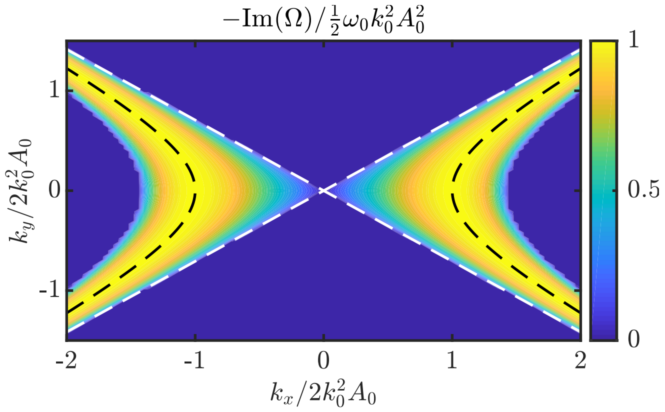

Figure 4.2: Linear stability growth rate of the 2D+1 NLSE (from (4.10)). The white dashed lines lie at the critical angles $\pm\theta_c$ and marks the angular boundary of stability. The black dashed line marks the maximum growth rate contour.

4.3 Experimental methodology

4.3.1 Facility

In order to examine the effects of waves crossing at large angles, all experiments were carried out in the circular FloWave Ocean Energy Research Facility at the University of Edinburgh (see figure 4.4 for a schematic description). This multi-directional wave basin has a 25 m diameter, is 2 m deep and is encircled by 168 actively absorbing force-feedback wavemakers, enabling creation of waves in all directions. A Cartesian coordinate system with origin at the centre of the tank is adopted. In all experiments, the x-axis is in the direction of the phase velocity of the carrier waves. The generation of waves by the wavemakers is based on linear theory. Practically, constrained by the limited number of wave gauges available and their robust positioning, a total of 16 resistance-type wave probes were placed along a low gantry that spanned the tank in the x-direction. In certain experiments, the gantry was moved in the transverse direction to alter the measurement y-coordinate, giving the effective probe layout shown in figure 4.4. The wave gauges were calibrated at the start of each day of testing. All experiments were sufficiently short that reflections did not interfere with incident measurements. A settling time of 20 min between each experiment was employed to allow for the absorption of reflected waves.

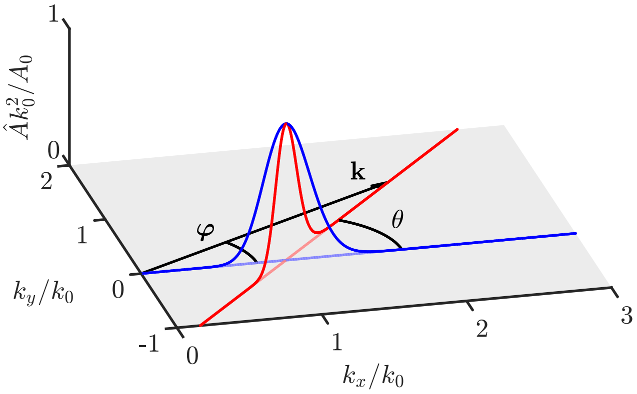

Figure 4.3: Amplitude spectrum of a crossed (red) and unidirectional (blue) wave group with wavenumber $\mathbf{k}$, crossing angle θ and component angle $\boldsymbol{\varphi}$.

4.3.2 Matrix of experiments and input parameters

To define a single crossed-wave group, a narrow-banded Gaussian amplitude spectrum in frequency space is chosen,

$$\hat{A}(\omega) = \frac{A_0\sigma^*}{\sqrt{2\pi}} \exp\left(-\frac{(\omega-\omega_0)^2{\sigma^*}^2}{2}\right), \tag{4.11}$$

where σ^* is now more generally the length of the group in the time domain, and (4.11) corresponds to the Fourier transform of a single arm in (4.9) at $x = y = 0$. An example of the spectrum given as input to the wavemakers is seen in figure 4.3.

In practice, the frequency vector was discretised such that each frequency was an integer multiple of $1/R$, where R is the repeat period of the test. All experiments were recorded for at least one repeat period with a sampling frequency of 128 Hz. The spectral bandwidth ($1/\sigma^*$)

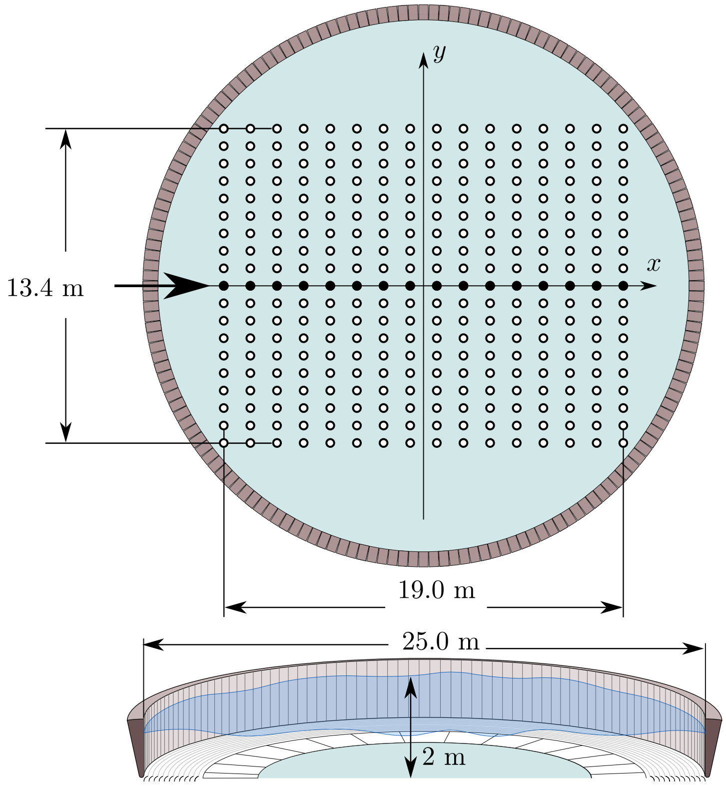

Figure 4.4: Schematic of the FloWave Ocean Energy Research Facility: the filled black circles indicate wave gauge positions during the single-crossed experiments and the open circles the effective wave probe positions achieved with repeated experiments. Principle wave direction is denoted with a single large arrow (schematic adapted from [92]).

was set as large as possible to encourage dispersion at non-critical angles while keeping the group narrow-banded and avoiding distortion of the signal due to the minimum frequency cut-off $\omega_{\min}$ (corresponding to $k_{\min}$) (see appendix G).

Table 4.1 summarises all the experiments conducted, distinguishing two main types: single crossed-wave groups (experiments 1a-d and 2a-d), consisting of only a positive arm and X-wave groups, consisting of both arms (experiment 3). Both lower-steepness (experiments 1a-d) and higher-steepness (experiments 2a-d) single crossed-groups were tested while X-wave group experiments were always of a higher-steepness. For the single crossed-group experiments, the crossing angle θ was varied while keeping the length of the group in time σ^* constant.

The evolution of the X-wave was measured by recording the free surface elevation using 16 wave gauges spaced in 1.23 m increments along the x-axis from -9.5 m to 9.5 m (filled black circles in figure 4.4), whereas the single crossed-wave experiments used 7 gauges spaced in roughly 2.5 m increments from -8.23 m to 4.42 m. All single crossed-wave experiments were repeated 4 times. For the X-wave, experiments were repeated 19 times, moving the y-position of the gauges in 0.75 m increments in order to obtain the effective spatial array in Figure 4.4. Repeatability was found to be extremely good in all single crossed-wave experiments (as shown by small values of standard deviation in all §4.4.1 results figures). However, limited time meant that exact repeats of the X-wave measurements were not possible and rely on inferring repeatability from the single crossed-wave experiments and the measurements taken at effective gauge locations.

Expt.	θ (°)	ω_0 (rad s^{-1})	$k_0 d$	σ^* (s)	$\epsilon_{\min}$	$\epsilon_{\max}$
1a	0	7.07	10.2	2.29	0.08	0.09
1b	$\theta_c^+/2$				0.08	0.09
1c	θ_c^+				0.08	0.09
1d	40				0.08	0.08
2a	0	7.07	10.2	2.29	0.17	0.25
2b	$\theta_c^+/2$				0.17	0.24
2c	θ_c^+				0.17	0.19
2d	40				0.17	0.16
3	θ_c^+ and θ_c^-	7.07	10.2	2.29	0.18	0.26

Table 4.1: Experimental parameters. Both the minimum and the maximum steepness observed during the experiments are reported, with $\epsilon \equiv k_0|A|$.

4.3.3 Data processing

In order to remove reflections, a 0.2-tapered Tukey window (25 s and 20 s for lower-steepness and higher-steepness tests, respectively) was applied across the incident wave group free surface elevation time histories. For all experiments, amplitude spectra were estimated and treated using a band-pass frequency filter with lower bound $0.7\omega_0$ and upper bound $1.6\omega_0$ to remove noise, higher-order bound waves, and low-frequency bound waves.

4.4 Results

For both single crossed-wave groups and X-waves, experimental results are compared with numerical solutions of the 2D+1 NLSE obtained using a split-step (pseudospectral) numerical scheme. The complex wavepacket amplitude at the first gauge (smallest x) is used as the boundary condition to the numerical solution which can be obtained from the recorded free surface as follows (see e.g. [99]),

$$A = (\eta + i\tilde{\eta})e^{-i(k_0 x - \omega_0 t)}, \tag{4.12}$$

where $\tilde{\eta}$ is the Hilbert-transform of the free surface elevation record (see appendix H for free surface time series).

4.4.1 Single crossed-wave groups

Figure 4.5 presents time series of the absolute of the experimental (coloured) and numerical (black) complex envelope, where dark and light lines represent the mean amplitude and associated confidence bands (across four repeated experiments), respectively. The blue lines denote the first gauge, and the red lines the final gauge along the evolution direction of waves (x-direction). Using the same notation, figure 4.6 presents the packet spectra of the experiments and numerical simulations, again showing the mean and confidence bands. In many cases, the confidence band is not clearly visible due to its proximity to the mean, indicating very good repeatability

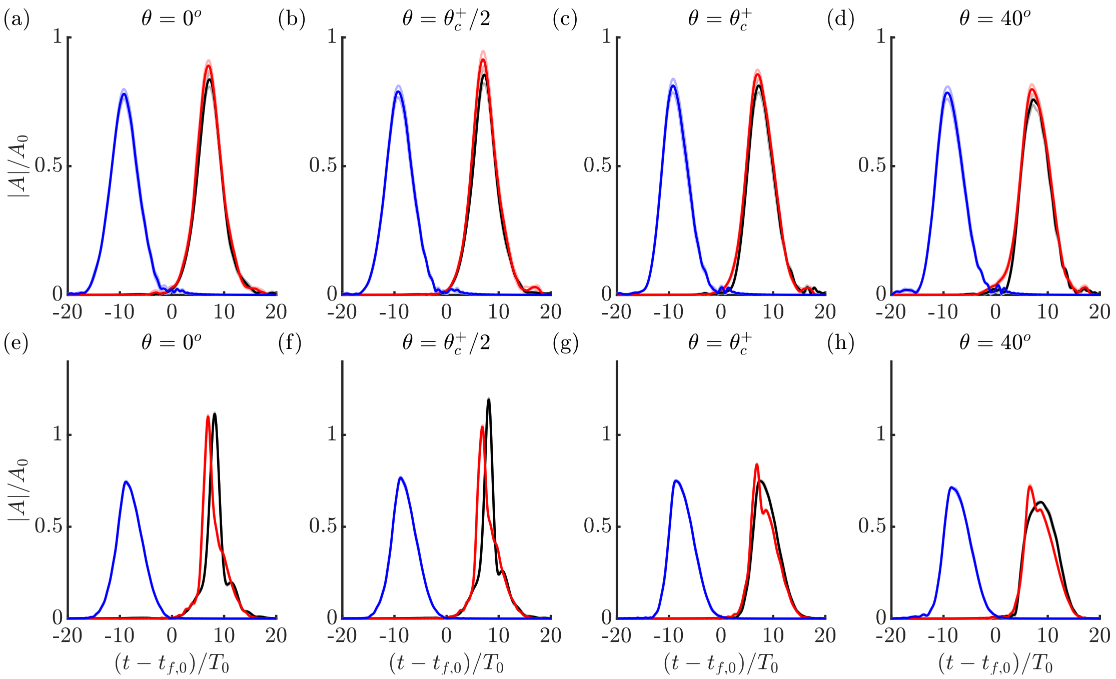

Figure 4.5: Envelope amplitude time series for the single crossed-wave lower-steepness experiments 1a-d (first row, panels a-d) and the higher-steepness experiments 2a-d (second row, panels e-h). Blue and red lines were extracted from the measured free surface time series at the initial ($x/\lambda_0 = -6.67$) and final ($x/\lambda_0 = 3.60$) gauges, respectively. The black line represents the numerical 2D+1 NLSE solution at the final gauge. The temporal signal is centred about the time at which the group passes $x = 0$ ($t_{f,0}$) and normalise by the carrier period (T_0) and the intended linear focused amplitude at $x = y = 0$ (A_0). The dark lines show the mean, and the light lines the confidence bands corresponding to one standard deviation either side of the mean.

of experiments. In both figures 4.5 and 4.6, sub-figures a-d (first row) correspond to the lower-steepness experiments (1a-d), whilst sub-figures e-h (second row) correspond to higher-steepness experiments (2a-d).

Two quantitative measures of dispersion are introduced: maximum group amplitude and group width. The maximum amplitude can be determined directly from the wave packet amplitude time series. Group width is defined through the central group time, $t_f = \sum_{i=1}^{N} \mathbf{t}_i \mathbf{A}_i / \sum_{i=1}^{N} \mathbf{A}_i$, in the form of a standard deviation, as,

$$t_\sigma = \sqrt{\frac{\sum_{i=1}^{N} \left(\mathbf{t}_i - t_f\right)^2 \mathbf{A}_i}{\sum_{i=1}^{N} \mathbf{A}_i}}, \tag{4.13}$$

where the indicator i simply corresponds to the discrete sampling points in time. Figure 4.7 shows the mean of the maximum amplitude across repeats for different crossing angles. Using the same notation, figure 4.8 presents the average width as calculated from (4.13). The numerical solutions appear as dashed lines in both figures 4.7 and 4.8.

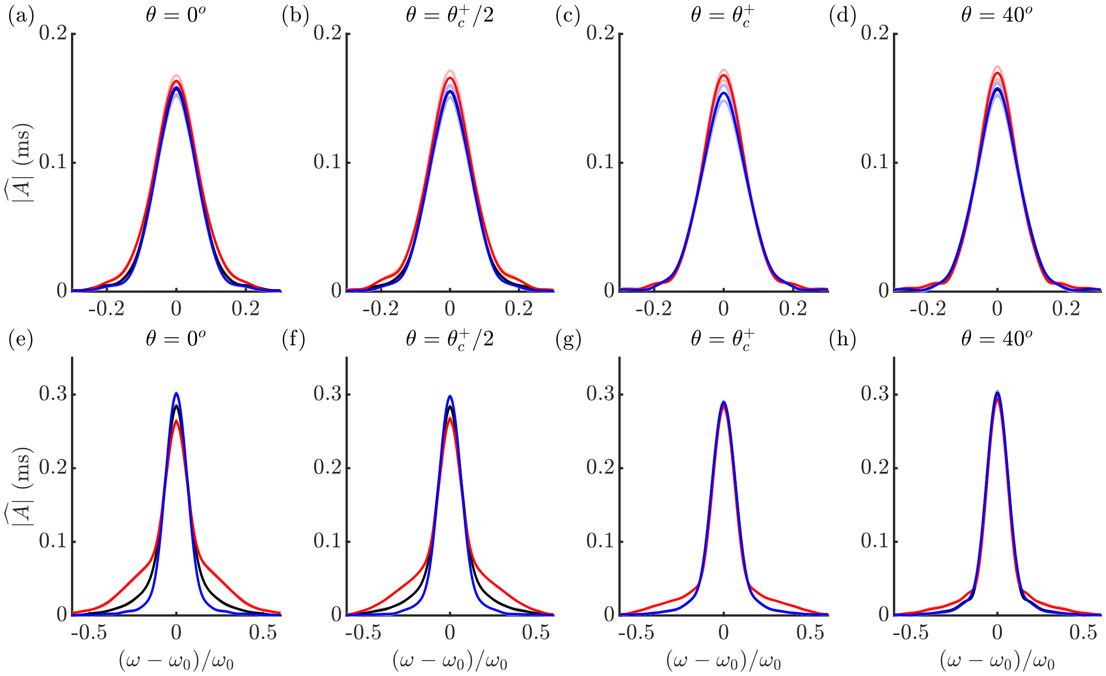

Figure 4.6: Spectra of amplitude envelope time series in figure 4.5, showing the lower-steepness experiments 1a-d (first row, panels a-d) and the higher-steepness experiments 2a-d (second row, panels e-h). The blue and red lines estimated from experimental time histories at the initial ($x/\lambda_0 = -6.67$) and final ($x/\lambda_0 = 3.60$) gauges respectively, whilst the black line represents the numerical 2D+1 NLSE solution at the final gauge. The dark lines show the mean, and the light lines the confidence bands corresponding to one standard deviation either side of the mean.

4.4.1.1 Lower-steepness experiments (1a-d)

In the lower-steepness case, both experimental and numerical packet time series in the unidirectional direction (figure 4.5a) show clear focusing, with the experimental packet amplitude increasing from $0.78A_0$ to $0.90A_0$ across $\approx 10\lambda_0$ of evolution (a small amount of underproduction by the wavemakers limited the focus amplitude slightly). Additionally, figure 4.8a shows a decrease in group width as the group undergoes dispersive focusing. The wave group travelling with $\theta_c^+/2$ in figure 4.5b shows very similar behaviour, as expected, based on the linear dispersion relationship (see figure G.1 in appendix G, noting the similar behaviour of the lines corresponding to $\theta = 0°$ and $\theta = \theta_c^+/2$). At the critical crossing angle, the wave group amplitude only increases from $0.83A_0$ to $0.86A_0$, and the width stays constant across the evolution distance. At the 40° crossing angle, the mean packet amplitude changes by less than $0.01A_0$, which is within one standard deviation across repeats. Again, the width of the 40° case stays constant across the evolution distance. This similar behaviour between θ_c^+ and 40° is predicted in the linear analysis presented in figure G.1. All spectra of the low-steepness experiments in figure 4.6a-d show minimal changes across their evolution indicating that the focusing seen in figure 4.5a-d is predominantly a result of linear wave behaviour.

Summarizing, it is clear from Figures 4.7a and 4.8a and that the behaviour of the 35.26° and the 40° cases are least dispersive, as predicted well by the 2D+1 NLSE (dashed lines), which is

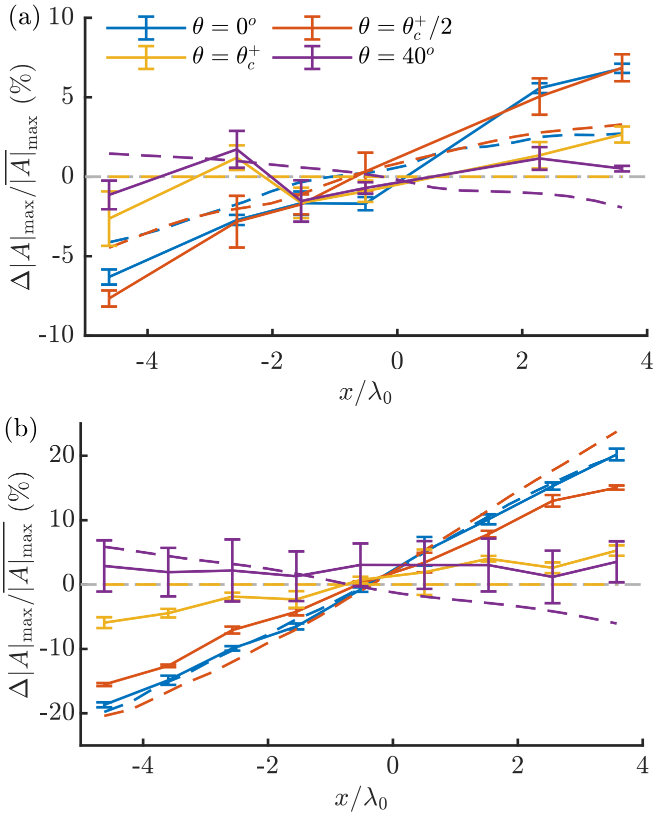

Figure 4.7: Relative change of the maximum packet amplitude $\Delta|A|_{\max} = |A|_{\max} - \overline{|A|_{\max}}$ in space for different crossing angles, where $\overline{|A|_{\max}}$ denotes the average across the gauges. Panel a shows experiments 1a-d (lower-steepness), and panel b experiments 2a-d (higher-steepness). The continuous lines denote the mean across repeat experiments with the errors bars corresponding to one standard deviation, and the dashed lines denote the numerical solutions.

behaving mostly linearly in these lower-steepness experiments.

4.4.1.2 Higher-steepness experiments (2a-d)

In the higher-steepness cases, the unidirectional (figure 4.5e) and $\theta = \theta_c^+/2$ (figure 4.5f) experiments show much more substantial focusing than their lower-steepness counterparts. The maximum amplitude of the wave in experiment 2a increases from $0.74A_0$ to $1.10A_0$ and in experiment 2b from $0.77A_0$ to $1.04A_0$, in both cases to beyond the theoretical linear focused amplitudes. Nonlinear changes are very likely to have occurred, as is evident from the significant spectral changes observed in figure 4.6e and f, including a drop in peak spectral amplitude and significant spectral widening as a classical signature of modulational instability. It is further evident that the 2D+1 NLSE (black lines) with its restrictions on steepness and bandwidth captures the main features but certainly not all aspects of the observed behaviour for these high-steepness, close-to-unidirectional cases.

The time domain behaviour of the higher-steepness critical angle experiment 2c (figure 4.5g) appears to show some changes in the packet shape, with larger waves moving to the front of the

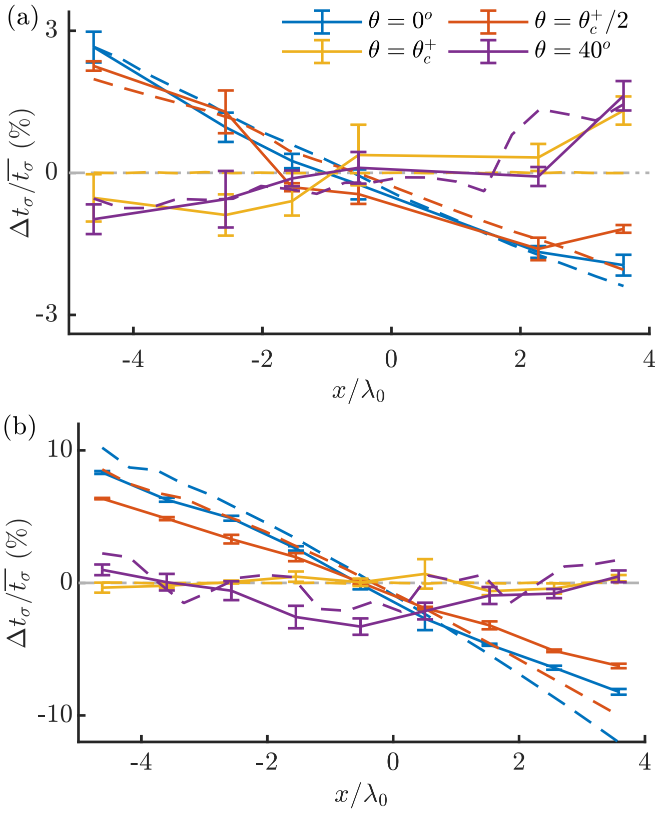

Figure 4.8: Relative change of the the group width parameter $\Delta t_\sigma = t_\sigma - \overline{t_\sigma}$ in space for different crossing angles, where $\overline{t_\sigma}$ denotes the average across the gauges and t_σ is defined by (4.13). Panel a shows experiments 1a-d (lower-steepness), panel b shows experiments 2a-d (higher-steepness). The continuous lines denote the mean across repeat experiments with the errors bars corresponding to one standard deviation, and the dashed lines denote the numerical solutions.

group creating a double-peak; however, the maximum amplitude of the group remains largely unchanged. The nullification of the dispersive term in the 2D+1 NLSE at the critical angle has removed linear focusing and stabilised the wave group as predicted by linear stability analysis (cf. (4.10) and figure 4.2). The numerical evaluation of the 2D+1 NLSE (black lines) shows these effects perfectly with a completely stationary wave group in its group velocity reference frame and figure 4.6g displaying an unchanging packet spectrum. Experiment 2d ($\theta = 40°$) in figure 4.5h shows very similar behaviour to the critical angle experiment. It is evident from figure 4.6e-h that for the high-steepness case spectral changes occur that are greater than predicted by the 2D+1 NLSE (figure 4.6e-f) or non-zero where zero changes are predicted by the 2D+1 NLSE (figure 4.6g-h).

Summarizing, it is clear from Figures 4.7b and 4.8b that, as with the low-steepness experiments, the behaviour of the 35.26° and the 40° cases is least dispersive, as predicted well by the 2D+1 NLSE (dashed lines) and that most of the strong nonlinearity observed for small and zero angles is quelled for these larger crossing angles.

4.4.2 X-wave

Turning from the single-crossed to the double-crossed or X-wave (experiment 3), surfaces of measured wave group amplitude $A(y, t)$ are reconstructed at different gauge locations suitable for comparison with the output of the numerical method as shown in figure 4.9 (left and middle columns, respectively). The corresponding spectra $\hat{A}(\omega, k_y)$ of the numerical result are also presented (right column). At the beginning of its evolution (top rows), the experimental X-wave structure is clearly visible with distinct arms lying on the expected $\pm\theta_c$ lines and a centroid of amplitude $2A_0$. The X-structure maintains its global shape as it propagates across the tank, although the finite number of straight wave paddles makes perfect generation by constructive super-positioning away from the centre and near the boundaries of the tank challenging. This is most evident from the long spatial behaviour in figure 4.9.

It is further evident that for this high-steepness experiment, the peak at the crossing points of the two arms undergoes considerable narrowing in the x-direction (its direction of travel, shown here as time t) and broadening in the y-direction, a phenomenon previously observed by Gibbs & Taylor for directionally spread groups that are not crossing and described therein as 'walls of water' [55]. This behaviour is observed in both experiments and numerical simulations of the 2D+1 NLSE and it is noted that its likely origin is from resonant third-order nonlinearity identified by Phillips arising from the interaction between four wave components [105]. Accordingly, the 2D+1 NLSE predicts a preferential energy transfer to higher wavenumbers, as shown in the right column of figure 4.9. Unlike the single crossed-wave groups, where all the non-zero spectral components are confined to a single line (cf. figure 4.3), the double-crossed or X-wave has sufficient components to take part in four-wave interaction (cf. Phillips's figure of 8). Indeed, Longuet-Higgins showed that for a narrow-banded three-dimensional wave packet the preferential direction of energy transfer to higher-wavenumbers is 35.26° [82].

4.5 Conclusion

This chapter has experimentally demonstrated the existence of stationary water wave groups when a carrier wave is modulated by a wavegroup crossing it at an angle of ±35.26°, as predicted by the 2D+1 NLSE. The lower-steepness, single crossed-wave group experiments showed significant reductions in linear focusing at the critical angle, with both amplitude and group width remaining constant across the evolution distance. The higher-steepness single crossed-group experiments confirmed these structures are also stable at angles equal or greater to the critical angle. Numerical solutions based on 2D+1 NLSE exhibited very similar behaviour, with perfectly stationary wave groups occurring at the critical angle, as expected. Although the unidirectional groups focused to more extreme amplitudes, the experimental observation of crossed groups propagating unchanged over many wavelengths confirms the lifetime extension of wave groups containing the potential for extreme events.

When the two arms travelling at ±35.26° are superimposed, a nondispersive hydrodynamic X-wave is constructed, which has been observed in the laboratory. Although nondispersive, such a structure, when observed for relatively high steepness, readily becomes subject to third-order resonant four-wave interaction, which are known to transfer energy to higher wavenumbers with a preferred direction of ±35.26° [82]. In the real ocean, this preferred growth direction may lead to the natural generation of X-waves, which in turn will be longed-lived due to their lack of dispersion confirmed experimentally herein.

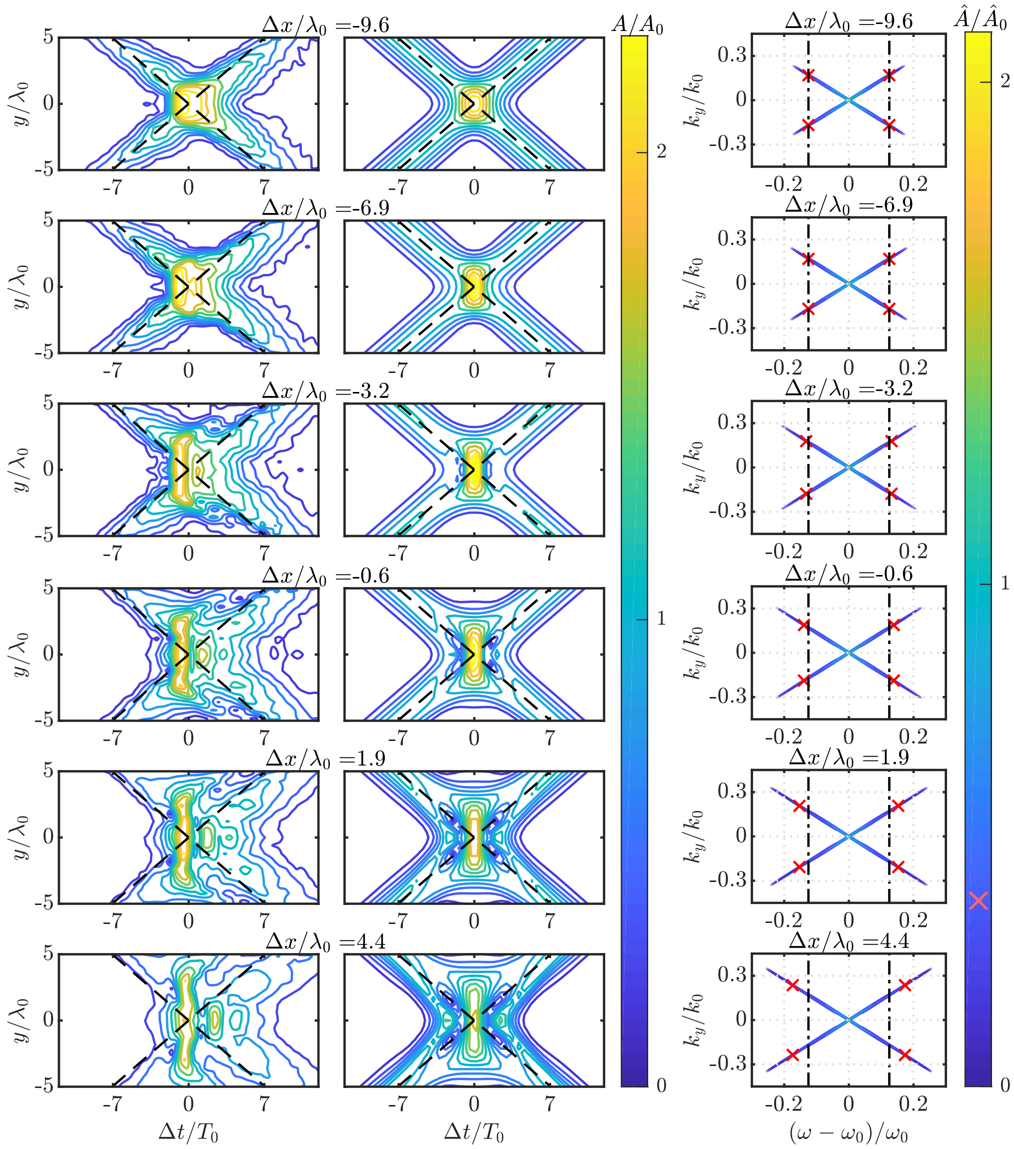

Figure 4.9: Spatio-temporal comparison of the experimental (left) and numerical (centre) X-wave packet $A(t, y)$ (experiment 3) as the packet evolves in space (rows). The black dashed lines corresponds to the 35.26° angle. The amplitude spectra $\hat{A}(\omega, k_y)$ of the numerical results are also presented (right): grey lines are grid lines, red crosses indicate the position of the contour at $\hat{A}/\hat{A}_0 = 0.33$ with the black dash-dotted lines aligned with the crosses in the top panel. The spatio-temporal signals in the group reference frame (as predicted by linear theory) are plotted.

Chapter 5

Conclusions and Recommendations

5.1 Conclusions

This thesis has investigated the dispersion and stability of surface gravity waves of non-negligible steepness, on deep water with vertical shear, coupled crossing wavetrains, and when a wavetrain and group are at an oblique angle.

5.1.1 Modulational stability on linearly sheared currents

For one-dimensional surface gravity waves travelling on a negatively sheared current, the relevant third-order wave evolution equation, the constant-vorticity nonlinear Schrödinger equation (vor-NLSE), predicts a stabilising of the wavetrain. In stabilising the wavetrain, slower growth and smaller waves at the end of the evolution are expected. It was found that at all shear rates tested, the vor-NLSE numerical solution predicted sideband growth well. It was also found that at all but the weakest shear rate, ($\Omega = -0.21$ s^{-1}) the vor-NLSE numerical solution significantly outperformed the standard, uniform current NLSE which showed errors in its amplification factor of up to 100%. Similarly, when the linear properties (wavelength and frequency) of low-steepness waves were measured, the constant-vorticity equations outperformed the uniform-current dispersion relation between shear rates of -0.87 s^{-1} $\leq \Omega \leq -0.48$ s^{-1}. These results show the arbitrary depth, constant-vorticity equations derived by Thomas, Kharif, and Manna in 2012 [123] to be appropriate for medium-steepness, narrow-banded waves, capable of describing their weakly nonlinear properties.

5.1.2 Modulational stability in crossing seas

The interaction of two weakly nonlinear wavetrains crossing at an angle was investigated experimentally. These experiments were compared with the coupled NLSE nonlinear Schrödinger eqaution (CNLSE). Experiments showed good agreement with numerical solutions of the CNLSE at all angles. At the lowest crossing angles, ($\theta < 20°$) significant sideband growth was observed but reduced significantly through all angles up to $\theta = 32°$, where complete stability of the system was observed. This result was expected from linear stability analysis of the CNLSE, where at $\theta \approx 35.26°$ medium-steepness wavetrains become stable regardless of carrier or sideband properties.

5.1.3 Nondispersive crossing waves

The two-dimensional nonlinear Schrödinger equation was used to impose an angle between the carrier and sideband components of a single narrow-banded Gaussian wave group. The resulting crossed wave group was expected to become linearly nondispersive and stable at $\theta \approx 35.26°$. The combination of these effects is a group travelling with entirely unchanged form along its primary axis (direction of the carrier wave). Relatively low-steepness Gaussian groups were seen to have normal dispersive properties up to $\theta = 17°$. At the critical, 35.26° angle and at 40°, the group became nondispersive, changing in group amplitude by no more than a single standard deviation. The medium-steepness crossed groups showed strong focusing throughout their evolution when unidirectional. However, as the crossing angle was increased, this dropped significantly up to the critical crossing angle. At the critical crossing angle, the overall group envelope had remained very close to its original form with minimal focusing of the group. Some nonlinear effects were observed through the medium-steepness group's evolution as a double peak had formed where higher amplitude waves had travelled faster and moved to the front of the group. Largely both the low and medium-steepness groups remained unchanged across their evolution. This result indicates that groups containing extreme waves are capable of remaining as such for much longer distances when crossed.

In Chapter 4, it has also been found that an X-wave structure created by the superposition of two crossed groups is capable of travelling large distances unchanged. Its strong central frequency peak will eventually move energy to components at $\pm 35.26°$ due to four-wave resonances, as predicted by Longuet-Higgins [82] and Phillips, [105].

5.2 Recommendations for future work

After investigating the applicability of the crossing and constant-vorticity NLSEs to a controlled experimental setting, a natural extension to this thesis would be an investigation into their application to real-world environments. However, prior to this investigation, further experimental investigation into each of the three conditions would provide useful additional information.

In future, experimental studies of nonlinear waves propagating on positively sheared (destabilising) currents should be carried out as these shear rates may push otherwise stable wavetrains into an unstable parameter space. Positive shear would only realistically be possible in a following current. This causes inherent difficulties in creating steep waves due to a reduction in both wavenumber and amplitude as waves move onto the following current. Using a long flume and high-frequency wavemakers, this investigation could be possible. With refinements, the method of producing a sheared current presented in this thesis could give current stability over the required extended distance. In either shear cases, observations of the evolution of the breather solution family on shear would be insightful. With precisely recreated initial conditions, breather solutions have a known amplification factor (of either 3 or 5 depending on the order of the solution [24]) and this fact would aid in refining and more precisely quantifying the effect of shear on amplification factor. Ultimately, laboratory experiments should be followed by investigations focusing on the applicability of the vor-NLSE to real-world environments. These may include the Scottish Pentland Firth, and the estuary of the Columbia River in the United States of America [73]. Both locations experience high rates of shipping traffic and strong current flows. The shear present in the Columbia river estuary has previously been studied with a focus on the linearity of its shear [80]. The conditions in the Pentland Firth are presently subject to intense scrutiny due to the newly present tidal-stream turbines installed in 2016 and further marine energy developments in the future.

An extension to the nondispersive, nonlinear crossed groups investigation should seek to increase the variation of parameters tested in order to explore the boundaries of the parameter space. Increasing the steepness of single crossed groups would determine whether waves with steepnesses close to that of a breaking wave are able to travel within a nondispersive group. Additionally, the effect of a breaking wave within the group and whether the group as a whole survives this event would provide more confidence to their existence in the real world. It should be noted that increasing waves to breaking within a nondispersive group would require a wave steepening method other than linear dispersion or nonlinear focusing (for example, changes in depth). An investigation into the effect of steepness on the spread of energy to the critical angle components of the X-wave would give further insight into the behaviour of these nondispersive structures.

The coupled wave systems investigated in this thesis fell into either the low-angle unstable region or the stable high-angle region. Changing the carrier properties and increasing the nonlinearity of the group, would allow the high angle unstable region to be investigated. If experimental results followed the predictions of the CNLSE, a mechanism for the generation of extreme waves higher and evolving quicker than those predicted in a unidirectional environment would be found. This would have a significant impact on the discussion between crossing and instability generation mechanisms. The group lengths of such wavetrains would be extremely large and the potential facility would need to allow for a long enough evolution distance. The facility would also be required to produce omnidirectional waves.

Ultimately, the three scenarios considered within this thesis should continue to be investigated in the context of their role in creating dangerous conditions for shipping and offshore structures by enhancing the effects of modulational instability. Throughout this thesis, other factors that exist in crossing and current-driven seas (directional induced set-up, current steepening etc.) have been discussed and should be included as compounding factors in any future studies. Lastly, it is my belief that the role of this thesis should be to provide an incremental step towards formalisation of dangerous sea conditions including modulational instability.

Appendix A

Chapter 2: Arbitrary Depth vor-NLSE Coefficients

The arbitrary-depth coefficients of the constant vorticity nonlinear Schrödinger equation (vor-NLSE) were first derived by [123] (TKM12). For completeness, the same coefficients as in TKM12 are presented here. Firstly, as in TKM12, some recurring terms are defined,

$$\mu = k_0 d, \quad \sigma = \tanh \mu, \quad X = \sigma \bar{\Omega}, \quad \text{and} \quad \bar{\Omega} = \Omega/\tilde{\omega}_0, \tag{A.1a,b,c,d}$$

where k_0 and $\tilde{\omega}_0$ are the carrier wavenumber and carrier frequency, d is the depth, and Ω is the shear rate. Tilde notation specifies a property measured in the surface current reference frame (see figure 2.1 for details of reference frames used). The vor-NLSE takes the form,

$$iA_\tau + LA_{\xi\xi} - M|A|^2 A = 0, \tag{A.2}$$

with slow-scale coordinates,

$$\xi = \epsilon(\tilde{x} - \tilde{c}_g t) \quad \text{and} \quad \tau = \epsilon^2 t, \tag{A.3a,b}$$

and fast-scale coordinate, x and t, where $\epsilon = k_0 a_0$ is the steepness of the carrier wave, and phase and group velocities are (respectively),

$$\tilde{c}_p = \frac{\tilde{\omega}_0}{k_0}, \quad \tilde{c}_g = \frac{\tilde{c}_p}{\sigma} \frac{(1-\sigma^2)k_0 d + \sigma(1+X)}{2+X}, \quad \text{with} \quad \rho = \frac{\tilde{c}_g}{\tilde{c}_p}. \tag{A.4a,b,c}$$

The arbitrary-depth linear vor-NLSE coefficient is,

$$L = \frac{\tilde{\omega}_0}{k_0^2 \sigma (2+X)} \left\{ \mu(1-\sigma^2)[1 - \mu\sigma + (1-\rho)X] - \sigma\rho^2 \right\}, \tag{A.5}$$

where the outside parentheses accidentally omitted in TKM12 (their (48)) have been included. The nonlinear coefficient is,

$$M = \frac{\tilde{\omega}_0 k_0^2 (U + VW)}{8(1+X)(2+X)\sigma^4}, \tag{A.6}$$

where,

$$U = 9 - 12\sigma^2 + 13\sigma^4 - 2\sigma^6 + (27 - 18\sigma^2 + 15\sigma^4)X + (33 - 3\sigma^2 + 4\sigma^4)X^2$$
$$+ (21 + 5\sigma^2)X^3 + (7 + 2\sigma^2)X^4 + X^5, \tag{A.7}$$

$$V = (1 + X)^2(1 + \rho + \mu\bar{\Omega}) + 1 + X - \rho\sigma^2 - \mu\sigma X, \quad \text{and} \tag{A.8}$$

$$W = 2\sigma^3 \frac{(1 + X)(2 + X) + \rho(1 - \sigma^2)}{\sigma\rho(\rho + \mu\bar{\Omega}) - \mu(1 + X)}. \tag{A.9}$$

Appendix B

Chapter 2: Current Profile Approximation

Although a perfectly linear profile could not be obtained, the current profiles used throughout experiments were designed to contain a strongly sheared, linearly varying velocity profile in their upper portion. The final current profiles were then investigated for their linearity using a comparison of the linear wave phase velocity predicted by a linearly sheared current, $c_{p,\Omega}$ and the linear wave phase velocity predicted by an arbitrarily sheared current, $c_{p,\mathrm{A}}$. A perfectly linearly varying current would produce no error between these two phase velocities. Wave phase velocity, $c_p = \omega/k$, is calculated using the depth-averaged velocity, $\bar{U}$ in the Doppler shift equation,

$$\omega = \tilde{\omega}(k) + k\bar{U}, \tag{B.1}$$

where the depth averaged velocity $\bar{U}$ is calculated from the Rayleigh equation (inviscid Orr-Sommerfeld equation) in finite depth [112] (see [117] for deep water),

$$\bar{U} = \frac{2k}{1 - e^{-4kd}} \left[\int_{-d}^{0} U(z) e^{2kz} \, \mathrm{d}z + e^{-4kd} \int_{-d}^{0} U(z) e^{-2kz} \, \mathrm{d}z \right]. \tag{B.2}$$

Equations (B.1) and (B.2) are used to calculate the percentage difference between the two phase velocities given in figure B.1. At the carrier wavenumber used for all experiments in Part II (6 $\mathrm{rad\,s^{-1}}$), the error in linear wave phase velocity associated with assuming a linear current is expected to be no more than 1% for the strongest current profile.

[117] also present the error, E, in phase velocity associated with limiting the depth-averaged integral to a depth, D. For deep water, the depth-averaged velocity is evaluated through the depths $-\infty < z < -D$ m and $-D < z < 0$ m, and the ratio of these integrals calculated. Using the finite-depth depth-averaged velocity (B.2), we calculate this error for $k = 6$ $\mathrm{rad\,m^{-1}}$ and present it in figure B.2. In this figure, we only show the strongest shear, as the other shear rates gave indistinguishable results. At $D \geq 0.2$ m, the error in phase velocity is less than 5%, with this reducing further to less than 1% at our chosen cut-off depth of 0.35 m.

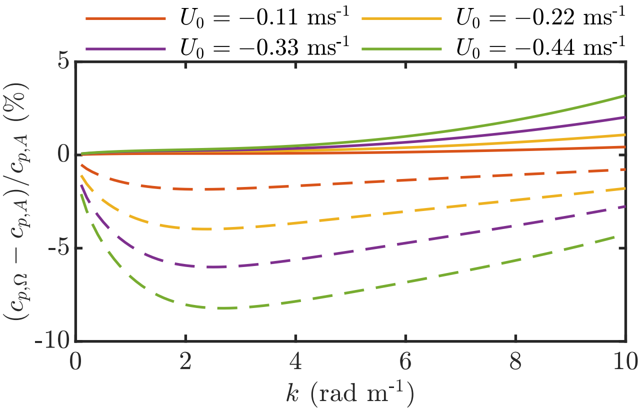

Figure B.1: Percentage difference between the linear phase velocity calculated when assuming a linearly sheared current profile, $c_{p,\Omega}$, and when assuming an arbitrarily sheared current profile, $c_{p,A}$, for the four current profiles in table 2.1. The continuous lines show the effect of the linear current approximation. The dashed lines show the effect of ignoring the current's shear altogether.

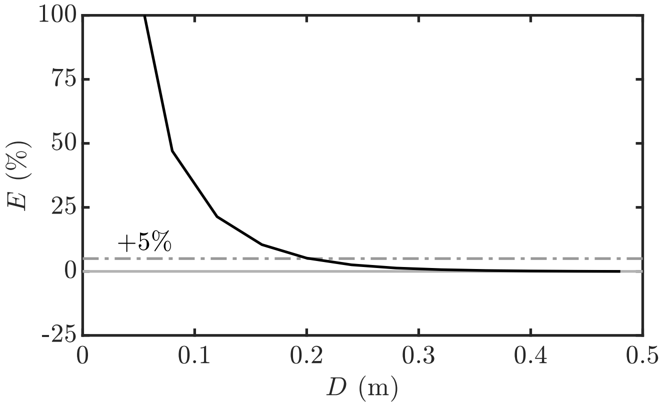

Figure B.2: Percentage error in phase velocity associated with estimating current down to a depth, D for a wave of wavenumber, $k = 6$ rad s^{-1} and the strongest shear rate ($\Omega = -0.87$ s^{-1}).

Appendix C

Chapter 2: vor-NLSE Numerical Method

Solving the arbitrary depth, constant vorticity nonlinear Schrödinger equation (vor-NLSE) and comparing the results to experimental measurements first requires a translation into the laboratory frame and then a change of form from the space-NLSE presented in [123] (describes change in time) to the time-NLSE (describes change in space). [22] details the relationship between time- and space- NLSEs. For comparison with experiments, it is most convenient for a time signal to be defined at the wavemaker and propagated spatially, as is the case with the time-NLSE. To obtain the time-NLSE from the space-NLSE in the group reference frame,

$$iA_\tau + LA_{\xi\xi} - M|A|^2A = 0, \tag{C.1}$$

which is translated out of the group reference frame and into laboratory frame coordinates, (x, t) using the chain rule,

$$i(A_t + c_gA_x) + LA_{xx} - M|A|^2A = 0, \tag{C.2}$$

where $c_g = \tilde{c}_g + U_0$, the sum of the surface current velocity and the group velocity in the surface current frame. This form is then transformed to the time-NLSE by changing linear and nonlinear coefficients and giving the time vor-NLSE to be solved numerically,

$$i(A_x + \frac{1}{c_g}A_t) + \frac{L}{c_g^3}A_{tt} - \frac{M}{c_g}|A|^2A = 0. \tag{C.3}$$

Given a periodic initial condition, the linear component of the vor-NLSE can be solved in Fourier space and allowing the use of the split-step numerical scheme. The split step method solves the linear and nonlinear components independently and exactly at each time step and then combines them (at which point a small error is introduced) [132]. The linear component is solved in Fourier space, whereas the nonlinear is solved in the time or space domain (depending on the form of the equation). A known error in carrier steepness of $\mathcal{O}(\epsilon^3)$ is associated with the independence assumption. The split-step method is second-order accurate in Δt and to all orders in Δx, it is unconditionally stable [121].

Within chapter 2, the following algorithm was implemented. First, the vor-NLSE in its time-form is rearranged and split into its linear, $\mathcal{L}$ and nonlinear, $\mathcal{N}$ components,

$$\mathcal{L} : A_x = -i\frac{L}{c_g^3}A_{tt} + \frac{1}{c_g}A_t, \tag{C.4}$$

$$\mathcal{N} : A_x = i\frac{M}{c_g}|A|^2 A. \tag{C.5}$$

The nonlinear component is integrated forwards in the space domain,

$$A_{i+1} = A_i e^{i\Delta x \frac{M}{c_g}|A_i|^2}, \tag{C.6}$$

where subscript i represents the current time-step. Meanwhile the linear component is Fourier-transformed,

$$\hat{A}_x = -i\hat{A}\frac{L}{c_g^3}(\tilde{\omega}i)^2 + \hat{A}\frac{1}{c_g}\tilde{\omega}i, \tag{C.7}$$

$$= i\hat{A}(\frac{L}{c_g^3}\tilde{\omega}^2 + \frac{1}{c_g}\tilde{\omega}), \tag{C.8}$$

and then discretised and integrated in time to give,

$$\hat{A}_{i+1} = \hat{A}_i e^{i\Delta x(\frac{L}{c_g^3}\tilde{\omega}^2 + \frac{1}{c_g}\tilde{\omega})}. \tag{C.9}$$

Combining the linear and nonlinear components at each time step the following explicit expression is obtained,

$$A_{i+1} = \mathcal{F}^{-1}\left(\hat{A}_i e^{i\Delta x(\frac{L}{c_g^3}\tilde{\omega}^2 + \frac{1}{c_g}\tilde{\omega})} + \mathcal{F}\left(A_i e^{i\Delta x \frac{M}{c_g}|A_i|^2}\right)\right). \tag{C.10}$$

Appendix D

Chapter 2: Extended Results

The evolution of the average sideband amplitudes are examined in the main text of Chapter 2. However, here, the evolution of the the separated upper and lower sidebands are shown in figures D.1-D.3.

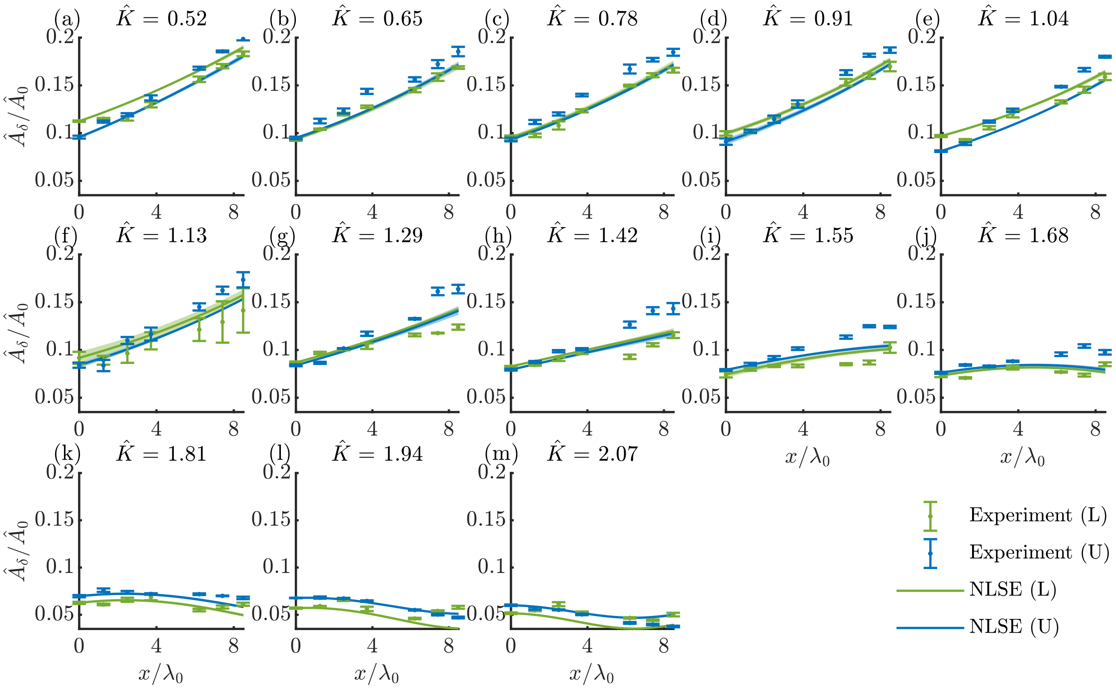

Figure D.1: $\mathbf{\Omega = 0}$ s^{-1} : Separated upper (U) and lower (L) primary sideband Fourier amplitudes, $\hat{A}_\delta$ normalized by the carrier Fourier amplitude, $\hat{A}_0$. Error bars denote two standard deviations from the mean as averaged across four repeats. All sidebands are represented as the normalized sideband wavenumber parameter $\hat{K} = K/K(\tilde{\gamma}_{\max})$. Solid lines indicate predictions made with the constant vorticity equations while dashed lines include only surface current in their predictions.

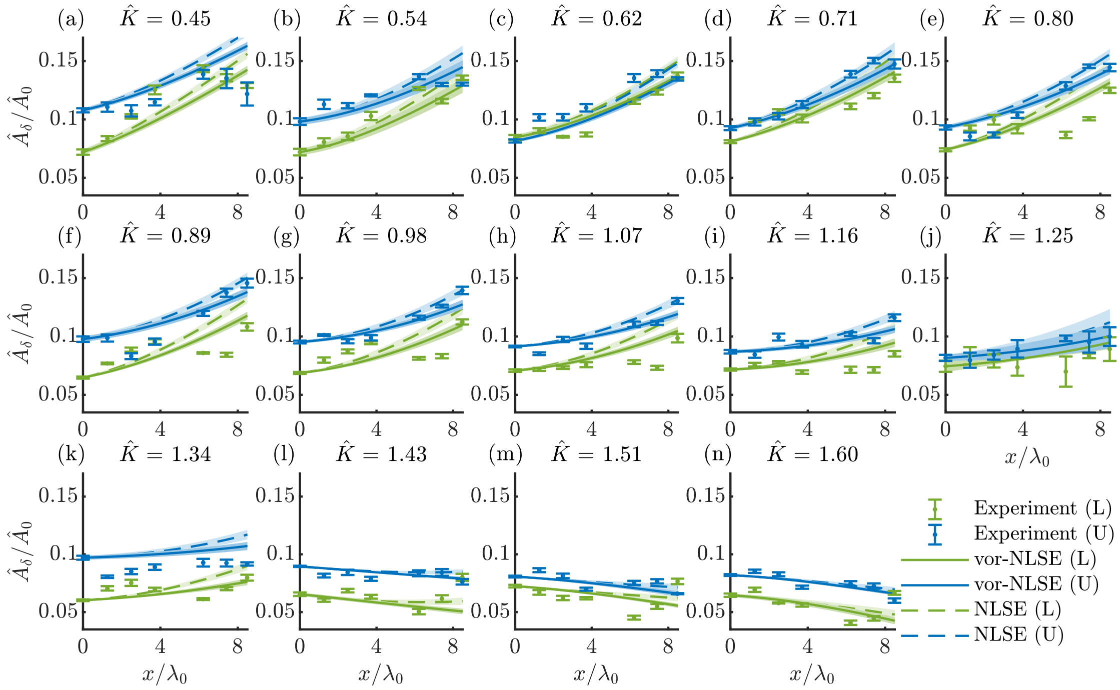

Figure D.2: $\mathbf{\Omega = -0.21}$ s^{-1} : Separated upper (U) and lower (L) primary sideband Fourier amplitudes, $\hat{A}_\delta$ normalized by the carrier Fourier amplitude, $\hat{A}_0$. Error bars denote two standard deviations from the mean as averaged across four repeats. All sidebands are represented as the normalized sideband wavenumber parameter $\hat{K} = K/K(\tilde{\gamma}_{\max})$. Solid lines indicate predictions made with the constant vorticity equations while dashed lines include only surface current in their predictions.

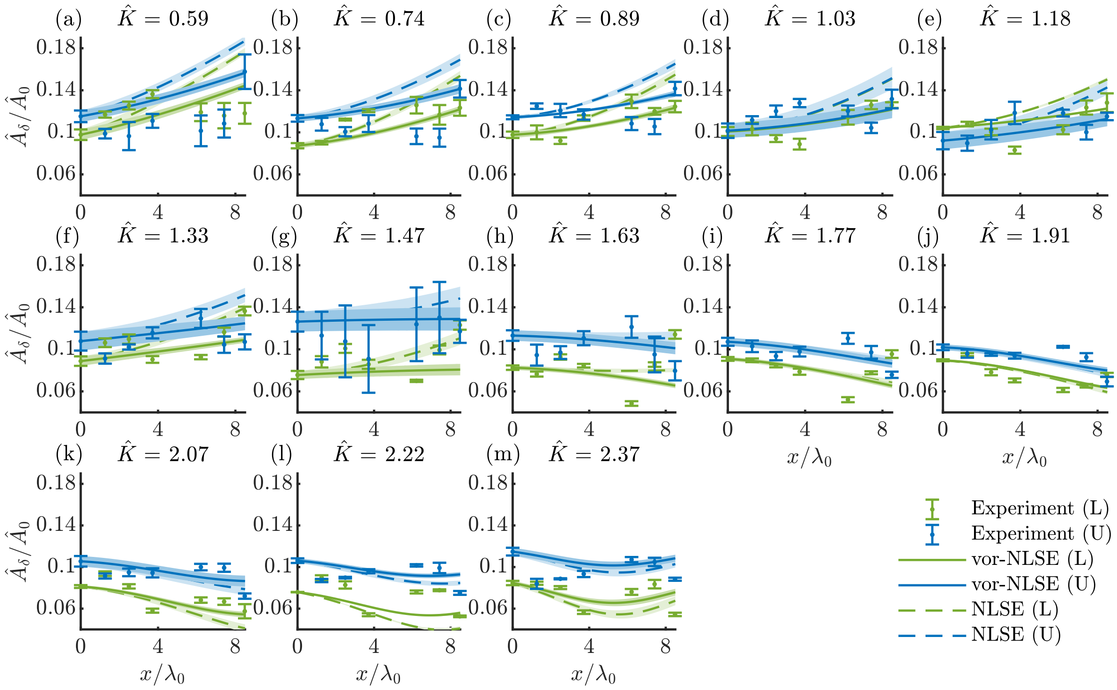

Figure D.3: $\mathbf{\Omega = -0.48}$ s^{-1} : Separated upper (U) and lower (L) primary sideband Fourier amplitudes, $\hat{A}_\delta$ normalized by the carrier Fourier amplitude, $\hat{A}_0$. Error bars denote two standard deviations from the mean as averaged across four repeats. All sidebands are represented as the normalized sideband wavenumber parameter $\hat{K} = K/K(\tilde{\gamma}_{\max})$. Solid lines indicate predictions made with the constant vorticity equations while dashed lines include only surface current in their predictions.

Appendix E

Chapter 3: Extended Results

E.1 Experiments 2i–l: $60^\circ \leq \theta \leq 88^\circ$

Experimental measurements of crossing waves at and above $\theta = 60^\circ$ are included here in the appendix for completeness. The finite-crest effect and exceedingly fast group velocity along the x-axis mean that growth rates close to $\theta = 90^\circ$ could not be measured if present.

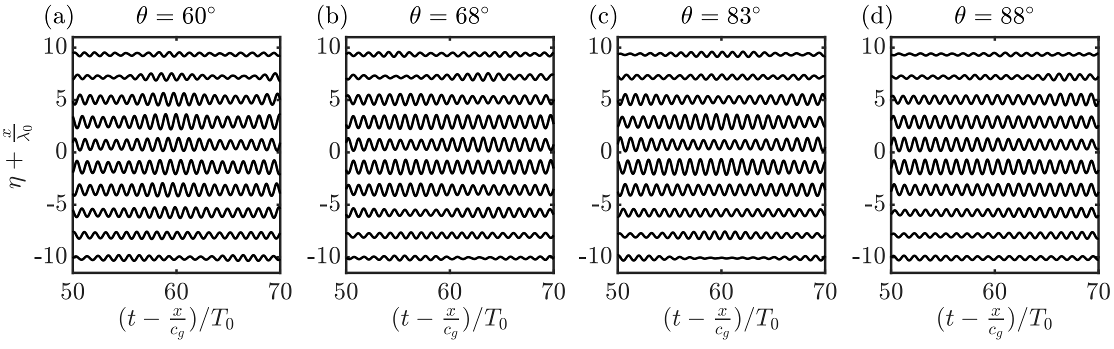

Figure E.1: Measured free surface elevation time series for experiments 2i–l (Part II) shifted by the linear group velocity $c_g = \sqrt{C_x^2 + C_y^2}$ and normalized by the carrier period, T_0, with the positive vertical representing increasing distance along the basin.

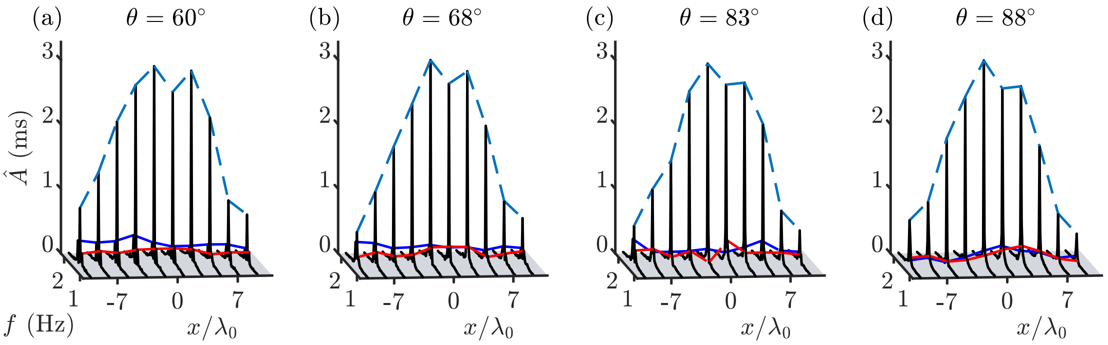

Figure E.2: Amplitude spectra for experiments 2i–l (Part II) obtained using the measured free surface time series along the primary wave propagation direction (see figure 3.3a for gauge locations) for different crossing angles, θ. Dashed lines follow the amplitudes of the carrier (light blue), lower sideband (red), and upper sideband (dark blue).

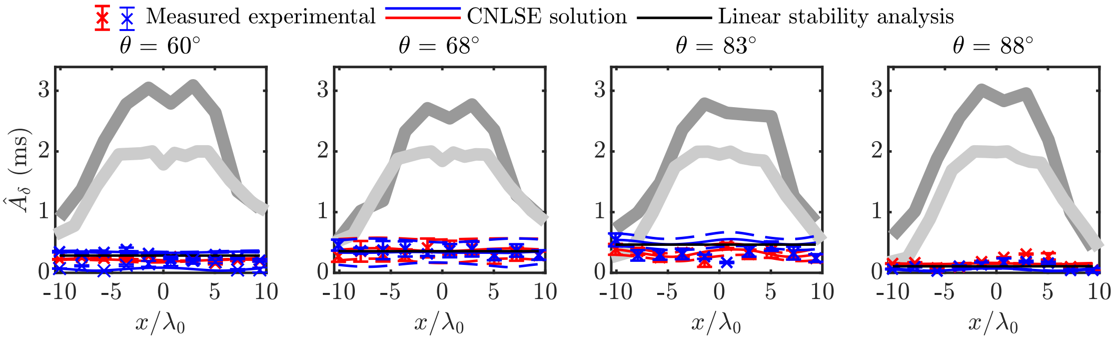

Figure E.3: Comparison of the evolution of sideband amplitude along the centreline of the basin for experiments 2i–l (Part II) from measurements, numerical solutions (crosses) of the CNLSE (thin blue and red lines) and linear stability analysis (thin black lines). Lower and upper sidebands are indicated in red and blue, respectively. Error bars and dashed lines represent one standard deviation from the mean across repeats for the measured data and the CNLSE solution, respectively. Thick lines represent carrier wave amplitudes from the seeded (Part II, dark grey) and unseeded (Part I, light grey) experiments.

Appendix F

Chapter 3: CNLSE Numerical Method

F.1 Split-step time marching technique

The split-step method (also known as the Fourier method) takes advantage of the fact that the linear and nonlinear components can be separated and then solved exactly [132]. The linear component is solved in Fourier space, whereas the nonlinear is solved in the time or space domain (depending on the form of the equation). In the split-step method, the linear and nonlinear components of the CNLSEs are treated independently and the predictions combined immediately after each time step as the full solution advances forward. A known error of $\mathcal{O}(\epsilon^3)$ (where $\epsilon = k_0 a_0$, the carrier wave steepness) is associated with the independence assumption. The split-step method is second-order accurate in Δt and to all orders in Δx, it is unconditionally stable [121].

First, the CNLSE is rearranged and split into its linear and nonlinear components (here only the A solution is considered for brevity),

$$\mathcal{L} : \frac{\partial A}{\partial t} = i\alpha \frac{\partial^2 A}{\partial x^2}, \quad \mathcal{N} : \frac{\partial A}{\partial t} = -i(\xi |A|^2 + 2\zeta |B|^2)A. \tag{F.1}$$

The nonlinear component is integrated forwards in the time domain as follows,

$$A_{i+1} = A_i e^{-i\Delta t(\xi |A_i|^2 + 2\zeta |B_i|^2)}, \tag{F.2}$$

whereas the linear component is Fourier-transformed,

$$\frac{\partial \hat{A}}{\partial t} = i\hat{A}\alpha(ik)^2, \tag{F.3}$$

$$= -i\alpha \hat{A} k^2, \tag{F.4}$$

and then integrated in time to give,

$$\hat{A}_{i+1} = \hat{A}_i e^{-i\Delta t \alpha k^2}. \tag{F.5}$$

Combining the linear and nonlinear components, at each time step the explicit expression is,

$$A_{i+1} = \mathcal{F}^{-1}\left(\hat{A}_i e^{-i\Delta t \alpha k^2} + \mathcal{F}\left(A_i e^{-i\Delta t(\xi|A_i|^2 + 2\zeta|B_i|^2)}\right)\right). \tag{F.6}$$

The same process is applied to the B solution. The results of advancing A and B individually are combined in the current time step to give the full system state to be passed to the next step.

Appendix G

Chapter 4: Critical Angle Linear Derivation

G.1 Narrow-band dispersive properties

In our wavenumber spectrum, all non-zero components are confined to the lines $k_y = \pm(k_x - k_0)\tan\theta$, of which Figure 4.3 illustrates a positive arm at crossing angle θ. It is evident that the smallest value the frequency and wavenumber vector magnitude can take is given by $k_{\min} = k_0 \sin(\theta)$. Substituting $k_y = \pm(k_x - k_0)\tan\theta$ into the deep-water dispersion relation yields a result that is dependent on k_x only,

$$\omega = \sqrt{g}\left(k_x^2 + (k_0 - k_x)^2 \tan\theta^2\right)^{\frac{1}{4}} . \tag{G.1}$$

Figure G.1 illustrates the group velocity $\mathrm{d}\,\omega/\mathrm{d}\,k_x$ obtained from (G.1) for different crossing angles. It is evident that the optimum group velocity, which corresponds to no dispersion at leading order, occurs at the carrier wavenumber ($k_x/k_0 = 1$) for $\theta = \theta_c$. The group velocity starts to deviate at larger and smaller wavenumbers, which would become significant in a more broad-banded spectrum, as discussed below.

G.2 Broad-band dispersive properties

The nondispersive crossing angle resulting from the 2D+1 NLSE assumes a narrow-banded spectrum and only requires that $\mathrm{d}^2\,\omega/\mathrm{d}\,k_x^2$ is zero at the carrier wavelength $k_x = k_0$. The requirement that all components have identical group velocities extends this definition to broadbanded spectra. A function, $k_y = f(k_x)$ is sought such that $\mathrm{d}^2\,\omega/\mathrm{d}\,k_x^2 = 0$ for all spectral components. The intersection between the dispersion surface $\omega = g^{1/2}\left(k_x^2 + k_y^2\right)^{1/4}$ and a plane tangent to this surface at the carrier, namely $\omega = c_g(k_x - k_0)$, defines this function implicitly. Explicitly in terms of k_y,

$$k_y = \pm\frac{(k_0 - k_x)\sqrt{k_0^2 + 6k_0k_x + k_x^2}}{4k_0}, \tag{G.2}$$

which is illustrated in Figure G.2.

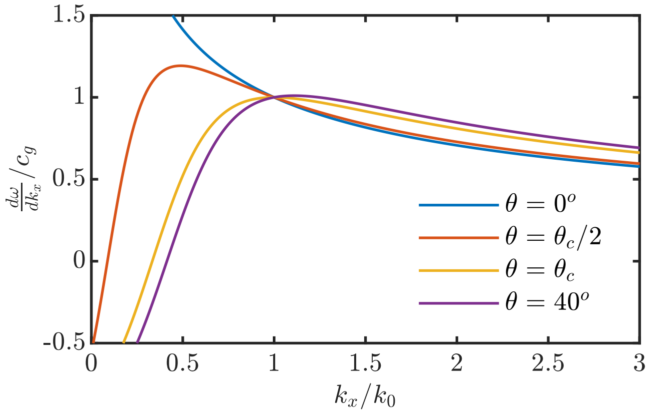

Figure G.1: Variation of group velocity for a range of crossing angles θ where. For the critical crossing angle θ_c, the slope of the group velocity with k_x is zero at the carrier wavenumber indicating nondispersive behaviour in the narrow-banded limit (from (G.1)).

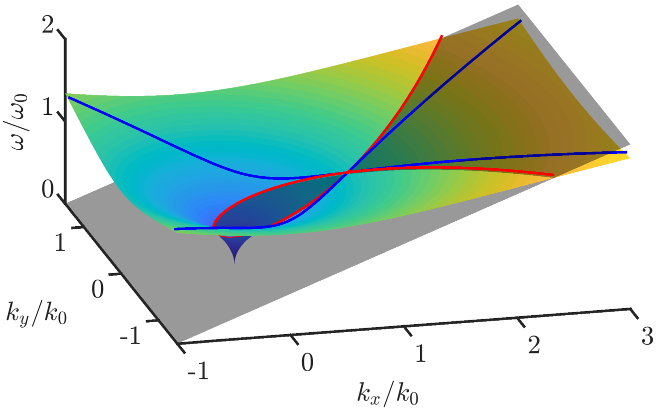

Figure G.2: Two-dimensional dispersion surface (colour) with the tangential grey transparent plane representing the group velocity at the carrier. The intersection of the two surfaces (red line) defines the broadbanded nondispersive solution; the narrow-banded approximation is represented by the blue line.

Appendix H

Chapter 4: Extended Results

Figure H.1 shows examples of the band-pass filtered free surface elevation time histories recorded for experiments 1a and 2a (unidirectional) and 1c and 2c (θ_c^+) single crossed-wave groups at initial (-5.7 m) and final (4.4 m) wave gauges. For the lower-steepness experiments, comparison between Figure H.1a and b reveals distinct focusing over a distance of roughly 10 wavelengths in the unidirectional case (panel a), whereas the group at the critical angle (panel b) remains largely unchanged. This difference is more obvious for the higher-steepness experiments in Figure H.1c and d where dispersion and nonlinear amplitude growth are both suppressed at the critical angle.

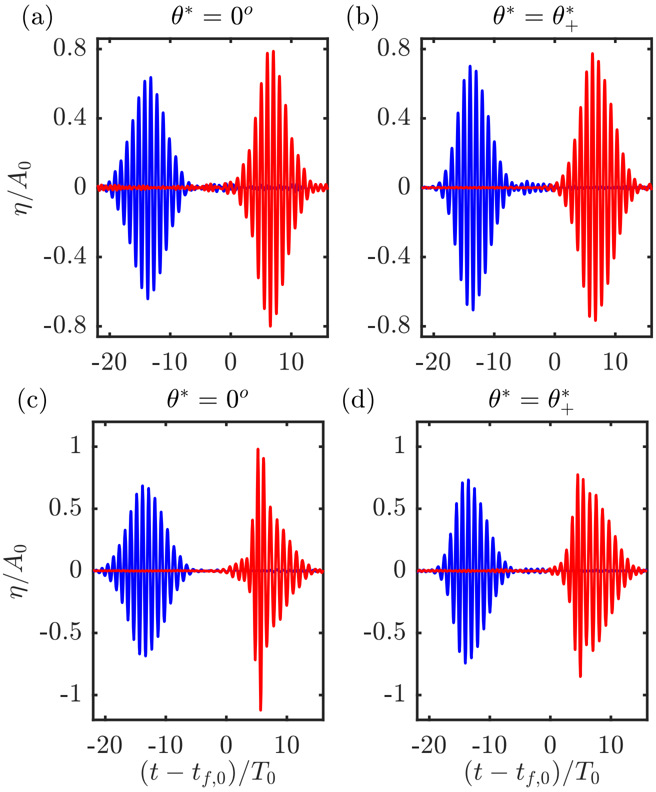

Figure H.1: Band-pass filtered free surface elevation time series for the lower-steepness single crossed-wave experiments 1a and 1c (first row, panels a and b) and the higher-steepness single crossed-wave experiments 2a and 2c (second row, panels c and d). Blue and red lines present results from initial ($x/\lambda_0 = -6.67$) and final ($x/\lambda_0 = 3.60$) gauges, respectively. We centre the temporal signal about the time the group passes $x = 0$ ($t_{f,0}$) and normalize by the carrier period (T_0) and the linear focused amplitude at $x = y = 0$ (A_0).

Bibliography

[1] Ablowitz, M. J. (2011). *Nonlinear dispersive waves: asymptotic analysis and solitons*, volume 47. Cambridge University Press.

[2] Ablowitz, M. J. and Horikis, T. P. (2015). Interacting nonlinear wave envelopes and rogue wave formation in deep water. *Phys. Fluid.*, 27(1):012107.

[3] Adcock, T. and Taylor, P. (2016). Fast and local non-linear evolution of steep wave-groups on deep water: A comparison of approximate models to fully non-linear simulations. *Phys. Fluids*, 28(1):016601.

[4] Adcock, T., Taylor, P., Yan, S., Ma, Q., and Janssen, P. (2011). Did the draupner wave occur in a crossing sea? *P. Roy. Soc. A*, 467(2134):3004–3021.

[5] Adcock, T. A. and Taylor, P. H. (2014). The physics of anomalous ('rogue') ocean waves. *Rep. Prog. Phys.*, 77(10):105901.

[6] Akhmediev, N., Ankiewicz, A., and Taki, M. (2009). Waves that appear from nowhere and disappear without a trace. *Phys. Lett. A*, 373(6):675–678.

[7] Akhmediev, N., Dudley, J. M., Solli, D., and Turitsyn, S. (2013). Recent progress in investigating optical rogue waves. *Journal of Optics*, 15(6):060201.

[8] Andrews, D. G. and McIntyre, M. E. (1978). On wave-action and its relatives. *J. Fluid Mech.*, 89(4):647–664.

[9] Baddour, R. and Song, S. (1990a). Interaction of higher-order water waves with uniform currents. *Ocean Eng.*, 17(6):551–568.

[10] Baddour, R. and Song, S. (1990b). On the interaction between waves and currents. *Ocean Eng.*, 17(1-2):1–21.

[11] Baronio, F. (2018). F. baronio, b. frisquet, s. chen, g. millot, s. wabnitz, and b. kibler, phys. rev. a 97, 013852 (2018). *Phys. Rev. A*, 97:013852.

[12] Baronio, F., Wabnitz, S., and Kodama, Y. (2016). Optical kerr spatiotemporal dark-lump dynamics of hydrodynamic origin. *Phys. Rev. Lett.*, 116(17):173901.

[13] Baumstein, A. I. (1998). Modulation of gravity waves with shear in water. *Stud. Appl. Math.*, 100(4):365–390.

[14] Benjamin, T. B. and Feir, J. E. (1967). The disintegration of wave trains on deep water part 1. theory. *J. Fluid Mech.*, 27(3):417–430.

[15] Biésel, F. (1950). Etude théorique de la houle en eau courante. *La Houille Blanche*,:279–285.

[16] Bitner-Gregersen, E. and Gramstad, O. (2015). Rogue waves impact on ships and offshore structures. *DNVGL Strategic Research and Innovation Position Paper.*

[17] Brennan, J., Dudley, J. M., and Dias, F. (2018). Extreme waves in crossing sea states. *Int. J. Ocean Coast. Eng.*, 1(01):1850001.

[18] Bretherton, F. P. and Garrett, C. J. R. (1968). Wavetrains in inhomogeneous moving media. *Proc. R. Soc. Lon. A Mat.*, 302(1471):529–554.

[19] Brittingham, J. N. (1983). Focus waves modes in homogeneous maxwells equations: Transverse electric mode. *J. Appl. Phys.*, 54(3):1179–1189.

[20] Cavaleri, L., Bertotti, L., Torrisi, L., Bitner-Gregersen, E., Serio, M., and Onorato, M. (2012). Rogue waves in crossing seas: The louis majesty accident. *J. Geophys. Res.-Oceans*, 117(C11).

[21] Chabchoub, A. and Fink, M. (2014). Time-reversal generation of rogue waves. *Physical review letters*, 112(12):124101.

[22] Chabchoub, A. and Grimshaw, R. H. J. (2016). The hydrodynamic nonlinear Schrödinger equation: Space and time. *Fluids*, 1(3):23.

[23] Chabchoub, A., Hoffmann, N., Branger, H., Kharif, C., and Akhmediev, N. (2013). Experiments on wind-perturbed rogue wave hydrodynamics using the peregrine breather model. *Physics of Fluids*, 25(10):101704.

[24] Chabchoub, A., Hoffmann, N., Onorato, M., and Akhmediev, N. (2012). Super rogue waves: observation of a higher-order breather in water waves. *Phys. Rev. X*, 2(1):011015.

[25] Chabchoub, A., Hoffmann, N. P., and Akhmediev, N. (2011). Rogue wave observation in a water wave tank. *Phys. Rev. Lett.*, 106(20):204502.

[26] Chabchoub, A., Kibler, B., Finot, C., Millot, G., Onorato, M., Dudley, J., and Babanin, A. (2015). The nonlinear Schrödinger equation and the propagation of weakly nonlinear waves in optical fibers and on the water surface. *Ann. Phys.*, 361.

[27] Chabchoub, A., Mozumi, K., Hoffman, N., Babanin, A. V., Toffoli, A., Steer, J. N., van den Bremer, T. S., Akhmediev, N., Onorato, M., and Waseda, T. (2019). Observation of short-crested slanted solitons and breathers. *P. Natl. A. Sci. USA (forthcoming).*

[28] Choi, W. (2009). Nonlinear surface waves interacting with a linear shear current. *Math. Comput. Simulat.*, 80(1):29–36.

[29] Christou, M., Tromans, P., Vanderschuren, L., and Ewans, K. (2009). Second-order crest statistics of realistic sea states. In *Proc. of the 11th Int. Workshop on Wave Hindcasting and Forecasting, Halifax, Canada*, pages 18–23.

[30] Constantin, A. and Strauss, W. (2004). Exact steady periodic water waves with vorticity. *Commun. Pur. Appl. Math.*, 57(4):481–527.

[31] Conti, C., Trillo, S., Di Trapani, P., Valiulis, G., Piskarskas, A., Jedrkiewicz, O., and Trull, J. (2003). Nonlinear electromagnetic x waves. *Phys. Rev. Lett.*, 90(17):170406.

[32] Craik, A. D. (1988). *Wave interactions and fluid flows.* Cambridge University Press.

[33] Craik, A. D. (2004). The origins of water wave theory. *Annu. Rev. Fluid Mech.*, 36:1–28.

[34] Da Silva, A. F. T. and Peregrine, D. H. (1988). Steep, steady surface waves on water of finite depth with constant vorticity. *J. Fluid Mech.*, 195:281–302.

[35] Dalrymple, R. A. (1974). A finite amplitude wave on a linear shear current. *J. Geophys. Res.*, 79(30):4498–4504.

[36] Dalrymple, R. A. (1977). A numerical model for periodic finite amplitude waves on a rotational fluid. *J. Comput. Phys.*, 24(1):29–42.

[37] Dalzell, J. F. (1999). A note on finite depth second-order wave–wave interactions. *App. Ocean Res.*, 21:105–111.

[38] Davey, A. and Stewartson, K. (1974). On three-dimensional packets of surface waves. *Proc. R. Soc. A*, 338:101–110.

[39] Degasperis, A., Lombardo, S., and Sommacal, M. (2019). Rogue wave type solutions and spectra of coupled nonlinear schrödinger equations. *Fluids*, 4(1):57.

[40] Di Trapani, P., Valiulis, G., Piskarskas, A., Jedrkiewicz, O., Trull, J., Conti, C., and Trillo, S. (2003). Spontaneously generated x-shaped light bullets. *Phys. Rev. Lett.*, 91(9):093904.

[41] Dudley, J. M., Dias, F., Erkintalo, M., and Genty, G. (2014). Instabilities, breathers and rogue waves in optics. *Nat. Photonics*, 8(10):755–764.

[42] Dudley, J. M., Genty, G., and Eggleton, B. J. (2008). Harnessing and control of optical rogue waves in supercontinuum generation. *Opt. Express*, 16(6):3644–3651.

[43] Dudley, J. M., Genty, G., Mussot, A., Chabchoub, A., and Dias, F. (2019). Rogue waves and analogies in optics and oceanography. *Nat. Rev. Phys.*, pages 1–15.

[44] Dysthe, K., Krogstad, H. E., and Müller, P. (2008). Oceanic rogue waves. *Annu. Rev. Fluid Mech.*, 40:287–310.

[45] Dysthe, K. B. (1979). Note on a modification to the nonlinear Schrodinger equation for application to deep water waves. *Proc. R. Soc. A*, 369:105–114.

[46] Dysthe, K. B., Trulsen, K., Krogstad, H. E., and Socquet-Juglard, H. (2003). Evolution of a narrow-band spectrum of random surface gravity waves. *J. Fluid Mech.*, 478:1–10.

[47] El Koussaifi, R., Tikan, A., Toffoli, A., Randoux, S., Suret, P., and Onorato, M. (2018). Spontaneous emergence of rogue waves in partially coherent waves: a quantitative experimental comparison between hydrodynamics and optics. *Phys. Rev. E*, 97(1):012208.

[48] Ellingsen, S. Å. and Brevik, I. (2014). How linear surface waves are affected by a current with constant vorticity. *Eur. J. Phys.*, 35(2):025005.

[49] Ellingsen, S. Å. and Li, Y. (2017). Approximate dispersion relations for waves on arbitrary shear flows. *J. Geophys. Res.-Oceans*, 122(12):9889–9905.

[50] Ewans, K. C. (1998). Observations of the directional spectrum of fetch-limited waves. *J. Phys. Oceanogr.*, 28(3):495–512.

[51] Fedele, F., Brennan, J., De León, S. P., Dudley, J., and Dias, F. (2016). Real world ocean rogue waves explained without the modulational instability. *Scientific Reports*, 6:27715.

[52] Fermi, E., Pasta, P., Ulam, S., and Tsingou, M. (1955). Studies of the nonlinear problems. Technical report, Los Alamos Scientific Lab., N. Mex.

[53] Ford, J. (1992). The fermi-pasta-ulam problem: paradox turns discovery. *Phys. Rep.*, 213(5):271–310.

[54] Forristall, G. Z. (2000). Wave crest distributions: Observations and second-order theory. *J. Phys. Oceanogr.*, 30:1931–1943.

[55] Gibbs, R. and Taylor, P. (2005). Formation of walls of water in ‘fully’ nonlinear simulations. *Appl. Ocean Res.*, 27(3):142–157.

[56] Goda, Y. and Suzuki, T. (1976). Estimation of incident and reflected waves in random wave experiments. *Coast. Eng. Proc.*, 1(15).

[57] Gramstad, O., Bitner-Gregersen, E., Trulsen, K., and Nieto Borge, J. C. (2018). Modulational instability and rogue waves in crossing sea states. *J. Phys. Oceanogr.*, 48(6):1317–1331.

[58] Groeneweg, J. and Klopman, G. (1998). Changes of the mean velocity profiles in the combined wave–current motion described in a glm formulation. *J. Fluid Mech.*, 370:271–296.

[59] Hammack, J. L., Henderson, D. M., and Segur, H. (2005). Progressive waves with persistent two-dimensional surface patterns in deep water. *J. Fluid Mech.*, 532:1–52.

[60] Hasimoto, H. and Ono, H. (1972). Nonlinear modulation of gravity waves. *J. Phys. Soc. Jpn.*, 33(3):805–811.

[61] Hasselmann, K. (1962). On the non-linear energy transfer in a gravity-wave spectrum part 1. General theory. *J. Fluid Mech.*, 12:481–500.

[62] Haver, S. (2004). A possible freak wave event measured at the Draupner jacket January 1 1995. In *Rogue Waves Workshop*, pages 1–8, Brest, France.

[63] Henry, D. (2013). On the pressure transfer function for solitary water waves with vorticity. *Math. Ann.*, 357(1):23–30.

[64] Henry, D. and Thomas, G. P. (2017). Prediction of the free-surface elevation for rotational water waves using the recovery of pressure at the bed. *Philos. T. Roy. Soc. A*, 376(2111):20170102.

[65] Herbers, T. H. C., Elgar, S., and Guza, R. T. (1994). Infragravity-frequency (0.005-0.05 Hz) motions on the shelf. part I: Forced waves. *J. Phys. Oceanogr.*, 24:917–927.

[66] Hughes, S. A. (1993). *Physical models and laboratory techniques in coastal engineering*, volume 7. World Scientific.

[67] Hui, W. H. and Hamilton, J. (1979). Exact solutions of a three-dimensional nonlinear Schrödinger equation applied to gravity waves. *J. Fluid. Mech.*, 93(1):117–133.

[68] Ito, T. and Okazaki, S. (2000). Pushing the limits of lithography. *Nature*, 406(6799):1027.

[69] Janssen, P. A. E. M. (1981). Modulational instability and the fermi-pasta-ulam recurrence. *Phys. Fluids*, 24(1):23–26.

[70] Jonsson, I., Brink-Kjaer, O., and Thomas, G. (1978). Wave action and set-down for waves on a shear current. *J. Fluid Mech.*, 87(3):401–416.

[71] Kharif, C. and Pelinovsky, E. (2003). Physical mechanisms of the rogue wave phenomenon. *Eur. J. Mech. B - Fluid*, 22(6):603–634.

[72] Kibler, B., Chabchoub, A., Gelash, A., Akhmediev, N., and Zakharov, V. E. (2015). Superregular breathers in optics and hydrodynamics: Omnipresent modulation instability beyond simple periodicity. *Phys. Rev. X*, 5(4):41026.

[73] Kilcher, L. F. and Nash, J. D. (2010). Structure and dynamics of the columbia river tidal plume front. *J. Geophys. Res.-Oceans*, 115(C5).

[74] Kimmoun, O., Hsu, H., Branger, H., Li, M., Chen, Y., Kharif, C., Onorato, M., Kelleher, E., Kibler, B., Akhmediev, N., et al. (2016). Modulation instability and phase-shifted fermi-pasta-ulam recurrence. *Sci. Rep.-UK*, 6:28516.

[75] Kirby, J. T. and Chen, T. (1989). Surface waves on vertically sheared flows: approximate dispersion relations. *J. Geophys. Res.-Oceans*, 94(C1):1013–1027.

[76] Klopman, G. (1994). Vertical structure of the flow due to waves and currents-laser-doppler flow measurements for waves following or opposing a current. *WL report H840-30, part II, for Rijkswaterstaat,*.

[77] Kundu, S., Debsarma, S., and Das, K. (2013). Modulational instability in crossing sea states over finite depth water. *Phys. Fluids*, 25(6):066605.

[78] Lake, B. M., Yuen, H. C., Rungaldier, H., and Ferguson, W. E. (1977a). Nonlinear deep-water waves: theory and experiment. Part 2. Evolution of a continuous wave train. *J. Fluid Mech.*, 83:49–74.

[79] Lake, B. M., Yuen, H. C., Rungaldier, H., and Ferguson, W. E. (1977b). Nonlinear deep-water waves: theory and experiment. part 2. evolution of a continuous wave train. *J. Fluid Mech.*, 83(1):49–74.

[80] Li, Y., Smeltzer, B. K., and Ellingsen, S. Å. (2017). Transient wave resistance upon a real shear current. *Eur. J. Mech. B-Fluid.*

[81] Lo, E. and Mei, C. C. (1985). A numerical study of water-wave modulation based on a higher-order nonlinear schrödinger equation. *J. Fluid Mech.*, 150:395–416.

[82] Longuet-Higgins, M. S. (1976). On the nonlinear transfer of energy in the peak of a gravity-wave spectrum: a simplified model. *Proc. R. Soc. Lond. A*, 347(1650):311–328.

[83] Lu, J. and Greenleaf, J. F. (1992). Nondiffracting x waves-exact solutions to free-space scalar wave equation and their finite aperture realizations. *IEEE T. Ultrason. Ferr.*, 39(1):19–31.

[84] Ma, Y.-C. (1979). The perturbed plane-wave solutions of the cubic Schrödinger equation. *Stud. Appl. Math.*, 60(1):43–58.

[85] Mallory, J. K. (1974). Abnormal waves on the south east coast of south africa. *Int. Hydrogr. Rev.*, 51(2).

[86] Marine Accident Investigation Branch (2016). Report on the investigation of the capsize and sinking of the cement carrier cemfjord in the pentland firth, scotland. Technical report, Marine Accident Investigation Branch.

[87] McAllister, M. L., Adcock, T. A. A., Taylor, P. H., and van den Bremer, T. S. (2018a). The set-down and set-up of directionally spread and crossing surface gravity wave groups. *J. Fluid Mech.*, 835:131–169.

[88] McAllister, M. L., Adcock, T. A. A., Taylor, P. H., and van den Bremer, T. S. (2018b). The set-down and set-up of directionally spread and crossing surface gravity wave groups. *J. Fluid. Mech.*, 835:131–169.

[89] McAllister, M. L., Draycott, S., Adcock, T. A. A., Taylor, P. H., and van den Bremer, T. S. (2019). Laboratory recreation of the Draupner wave and the role of breaking in crossing seas. *J. Fluid Mech.*, 860:767–786.

[90] Melville, W. K. (1982). The instability and breaking of deep-water waves. *J. Fluid Mech.*, 115:165–185.

[91] Mori, N. and Janssen, P. A. (2006). On kurtosis and occurrence probability of freak waves. *J. Phys. Ocean.*, 36(7):1471–1483.

[92] Noble, D. R. (2017). Combined wave-current scale model testing at flowave. *EngD.*

[93] Okihiro, M., Guza, R. T., and Seymour, R. J. (1992). Bound infra-gravity waves. *J. Geophys. Res.*, 97:453–469.

[94] Onorato, M., Baronio, F., Conforti, M., Chabchoub, A., Suret, P., and Randoux, S. (2016). Hydrodynamic and optical waves: A common approach for unidimensional propagation. In *Rogue and Shock Waves in Nonlinear Dispersive Media*, pages 1–22. Springer.

[95] Onorato, M., Osborne, A. R., and Serio, M. (2006). Modulational instability in crossing sea states: A possible mechanism for the formation of freak waves. *Phys. Rev. Lett.*, 96(1):014503.

[96] Onorato, M., Proment, D., and Toffoli, A. (2010). Freak waves in crossing seas. *Eur. Phys. J. - Spec. Top.*, 185(1):45–55.

[97] Onorato, M., Proment, D., and Toffoli, A. (2011). Triggering rogue waves in opposing currents. *Phys. rev. lett.*, 107(18):184502.

[98] Onorato, M., Residori, S., Bortolozzo, U., Montina, A., and Arecchi, F. (2013). Rogue waves and their generating mechanisms in different physical contexts. *Phys. Rep.*, 528(2):47–89.

[99] Osborne, A. (2010). *Nonlinear Ocean Waves and the Inverse Scattering Transform.* Academic Press.

[100] Osborne, A. R., Resio, D. T., Costa, A., de León, S. P., and Chirivì, E. (2019). Highly nonlinear wind waves in currituck sound: dense breather turbulence in random ocean waves. *Ocean Dynam.*, 69(2):187–219.

[101] Pelinovsky, E., Kharif, C., et al. (2008). *Extreme ocean waves.* Springer.

[102] Peregrine, D. H. (1976). Interaction of water waves and currents. In *Advances in Applied Mechanics*, volume 16, pages 9–117. Elsevier.

[103] Peregrine, D. H. (1983). Water waves, nonlinear Schrödinger equations and their solutions. *ANZIAM J.*, 25(1):16–43.

[104] Peregrine, D. H. and Jonsson, I. G. (1983). Interaction of waves and currents. Technical report, University of Bristol.

[105] Phillips, O. (1960). On the dynamics of unsteady gravity waves of finite amplitude part 1. the elementary interactions. *Journal of Fluid Mechanics*, 9(2):193–217.

[106] Quinn, B. E., Toledo, Y., and Shrira, V. I. (2017). Explicit wave action conservation for water waves on vertically sheared flows. *Ocean Model.*, 112:33–47.

[107] Ruban, V. (2010). Giant waves in weakly crossing sea states. *J. Exp. Theor. Phys.+*, 110(3):529–536.

[108] Saffman, P. G. and Yuen, H. C. (1978). Stability of a plane soliton to infinitesimal two-dimensional perturbations. *Phys. Fluid.*, 21(8):1450–1451.

[109] Santo, H., Taylor, P. H., Eatock Taylor, R., and Choo, Y. S. (2013). Average properties of the largest waves in Hurricane Camille. *J. Offshore Mech. Arct.*, 135:011602.

[110] Sharma, J. N. and Dean, R. G. (1981). Second-order directional seas and associated wave forces. *Soc. Petrol. Eng. J.*, 21:129–140.

[111] Shrira, V. I. and Slunyaev, A. V. (2014). Trapped waves on jet currents: asymptotic modal approach. *J. Fluid Mech.*, 738:65–104.

[112] Skop, R. A. (1987). Approximate dispersion relation for wave-current interactions. *J. Waterw. Port Coast.*, 113(2):187–195.

[113] Solli, D., Ropers, C., and Jalali, B. (2008). Active control of rogue waves for stimulated supercontinuum generation. *Physical review letters*, 101(23):233902.

[114] Solli, D., Ropers, C., Koonath, P., and Jalali, B. (2007). Optical rogue waves. *Nature*, 450(7172):1054.

[115] Stagonas, D., Buldakov, E., and Simons, R. (2014). Focusing unidirectional wave groups on finite water depth with and without currents. *Coast. Eng. Proc.*, 1(34):31.

[116] Steer, J. N., McAllister, M. L., Borthwick, A. G., and van den Bremer, T. S. (2019). Experimental observation of modulational instability in crossing surface gravity wavetrains. *Fluids*, 4(2):105.

[117] Stewart, R. H. and Joy, J. W. (1974). Hf radio measurements of surface currents. In *Deep-sea Res.*, volume 21, pages 1039–1049. Elsevier.

[118] Støle-Hentschel, S., Trulsen, K., Rye, L. B., and Raustøl, A. (2018). Extreme wave statistics of counter-propagating, irregular, long-crested sea states. *Phys. Fluids*, 30(6):067102.

[119] Swan, C., Cummins, I. P., and James, R. L. (2001). An experimental study of two-dimensional surface water waves propagating on depth-varying currents. part 1. regular waves. *J. Fluid Mech.*, 428:273–304.

[120] Swan, C. and James, R. L. (2000). A simple analytical model for surface water waves on a depth-varying current. *Appl. Ocean Res.*, 22(6):331–347.

[121] Taha, T. R. and Ablowitz, M. I. (1984). Analytical and numerical aspects of certain nonlinear evolution equations. ii. numerical, nonlinear Schrödinger equation. *J. Comput. Phys.*, 55(2):203–230.

[122] Thomas, G. P. (1990). Wave–current interactions: an experimental and numerical study. part 2. nonlinear waves. *J. Fluid Mech.*, 216:505–536.

[123] Thomas, R., Kharif, C., and Manna, M. (2012). A nonlinear Schrödinger equation for water waves on finite depth with constant vorticity. *Phys. Fluids*, 24(12):127102.

[124] Thompson, P. D. (1949). The propagation of small surface disturbances through rotational flow. *Ann. N.Y. Acad. Sci.*, 51(1):463–474.

[125] Toffoli, A., Bitner-Gregersen, E. M., Osborne, A. R., Serio, M., Monbaliu, J., and Onorato, M. (2011). Extreme waves in random crossing seas: Laboratory experiments and numerical simulations. *Geophys. Res. Lett.*, 38(6).

[126] Toffoli, A., Fernandez, L., Monbaliu, J., Benoit, M., Gagnaire-Renou, E., Lefevre, J., Cavaleri, L., Proment, D., Pakozdi, C., Stansberg, C., et al. (2013). Experimental evidence of the modulation of a plane wave to oblique perturbations and generation of rogue waves in finite water depth. *Phys. Fluids*, 25(9):091701.

[127] Toffoli, A., Monbaliu, J., Onorato, M., Osborne, A. R., Babanin, A. V., and Bitner-Gregersen, E. M. (2007). Second-order theory and setup in surface gravity waves: a comparison with experimental data. *J. Phys. Oceanogr.*, 37:2726–2739.

[128] Toffoli, A., Onorato, M., and Monbaliu, J. (2006). Wave statistics in unimodal and bimodal seas from a second-order model. *Eur. J. Mech. B-Fluid.*, 25(5):649–661.

[129] Toffoli, A., Waseda, T., Houtani, H., Cavaleri, L., Greaves, D., and Onorato, M. (2015). Rogue waves in opposing currents: an experimental study on deterministic and stochastic wave trains. *J. Fluid Mech.*, 769:277–297.

[130] Vanden-Broeck, J.-M. (1996). Periodic waves with constant vorticity in water of infinite depth. *IMA J. Appl. Math.*, 56(3):207–217.

[131] Walker, D. A. G., Taylor, P. H., and Eatock Taylor, R. (2004). The shape of large surface waves on the open sea and the Draupner New Year wave. *App. Ocean Res.*, 26:73–83.

[132] Weideman, J. A. C. and Herbst, B. M. (1986). Split-step methods for the solution of the nonlinear Schrödinger equation. *SIAM J. Numer. Anal.*, 23(3):485–507.

[133] Whitham, G. B. (1965). A general approach to linear and non-linear dispersive waves using a Lagrangian. *J. Fluid Mech.*, 22(2):273–283.

[134] Willebrand, H. A. and Ghuman, B. S. (2001). Fiber optics without fiber. *IEEE Spectrum*, 38(8):40–45.

[135] Young, I., Verhagen, L., and Banner, M. (1995). A note on the bimodal directional spreading of fetch-limited wind waves. *J. Geophys. Res. - Oceans*, 100(C1):773–778.

[136] Yuen, H. C. and Lake, B. M. (1982). Nonlinear dynamics of deep-water gravity waves. In *Adv. Appl. Mech.*, volume 22, pages 67–229. Elsevier.

[137] Zakharov, V. E. (1968). Stability of periodic waves of finite amplitude on the surface of a deep fluid. *J. Appl. Mech. Tech. Phy.*, 9(2):190–194.

[138] Ziolkowski, R. W. (1985). Exact solutions of the wave equation with complex source locations. *J. Math. Phys.*, 26(4):861–863.

[139] Ziolkowski, R. W. (1989). Localized transmission of electromagnetic energy. *Phys. Rev. A*, 39(4):2005.